Delft University of Technology

Master Thesis

Interference in 79 GHz Phase-Coded Automotive Radar

Author:
Jeroen Overdevest

Supervisors:
Ir. F. Jansen (NXP)
Dr. F. Uysal (MS3)
Prof. Dr. A.G. Yarovoy (MS3)

Microwave Sensing, Signals and Systems
Department of Microelectronics

July 3, 2018

Interference in 79 GHz Phase-Coded Automotive Radar

by

Jeroen Overdevest

to obtain the degree of Master of Science
at the Delft University of Technology,
to be defended publicly on July 9, 2018

Student number:	4215109	
Project duration:	September 11, 2017 - July 9, 2018	
Thesis committee:	Prof. dr. A. Yarovoy	Microwave, Sensing, Signals and Systems (TU Delft)
	Dr. F. Uysal	Microwave, Sensing, Signals and Systems (TU Delft)
	Prof. dr. ir. G.J.T Leus	Circuits & Systems (TU Delft)
	Ir. F. Jansen	NXP Semiconductors

This thesis excludes multiple appendices for purposes of confidentiality for NXP Semiconductors.

Abstract

Jeroen Overdevest

Interference in 79 GHz Phase-Coded Automotive Radar

Automotive radars play a crucial role in the reduction of traffic casualties and the realization of autonomous driving due to its robustness and adverse weather tolerance. However, as the penetration rate of automotive radars increases, concerns arise regarding the mutual interference. In contrast to the predominant Frequency-Modulated Continuous Wave (FMCW) radars, Phase-Modulated Continuous Wave (PMCW) radars might provide solutions for the interference problem by coding the waveforms, which brings an additional degree of freedom.

In this thesis, a system level overview of the phase-coded radar is presented. Regarding the popular code families, particular attention was given to the Gold, Almost Perfect Autocorrelation Sequences (APAS), and Zero-Correlation Zone (ZCZ) sequences. This thesis has proposed three distinct designs for 16-TX-element MIMO Phase-Coded radar that drives the requirements of a Medium Range Radar (MRR). The conclusion can be drawn that APAS and ZCZ sequences have shown to provide a (sub)optimal design that is emphasized by their perfect correlation characteristics within the designated distance of interest.

Furthermore, in full-transmit capacity MIMO, the proposed designs use semi-orthogonal waveforms to provide excellent performance in synchronous PMCW radars. However, performance degrades in case Doppler-shifted reflections are received, whereas sidelobes arise in range due to non-orthogonality. This thesis concludes that the APAS-coded waveforms are most tolerant to Doppler shift; besides, its Time Division Multiplexing (TDM) MIMO Transmission scheme is computationally more efficient than the Code Division Multiplexing (CDM) scheme used in Gold and ZCZ coded waveforms.

Finally, the radar-to-radar interference investigation has proven that for uncorrelated PMCW-to-PMCW interference, the noise floor undergoes a consistent increase, which is according to the interference-plus-noise power level calculated from the link budget analysis. This thesis emphasizes these results, as the interference effect in FMCW-to-FMCW (provided by NXP Semiconductors) have seen similar phenomena. Therefore, results in this thesis support the conclusion that coded waveforms do not remove or suppress the energy levels of the interference. For correlated interference, ghost targets might be formed, but this depends on the starting time as well as the starting coded bit of the interferer, as the correlation peak can be formed outside the distance of interest.

Acknowledgements

First of all, I would like to sincerely thank the Microwave Sensing, Signals and Systems (MS3) Group and NXP Semiconductors N.V. for giving me the opportunity to do a 9-month study in my field of interest.

My supervisors Dr. Faruk Uysal (MS3) and Ir. Feike Jansen (NXP) need close attention as I cannot thank them more for the guidance and expertise they have provided during my thesis. I highly respect the amount of valuable time they have put into me. Their office doors were always open, and they were willing to answer my questions at any moment. Also, I would like to thank Prof. Yarovoy for his interest in my thesis and his valuable in-depth and high-level feedback. Furthermore, I would like to acknowledge Francesco Laghezza (NXP) for the engaging discussions on interference and the comparisons to FMCW radar systems.

The support of my family needs to be emphasized as well. Their belief in me helped me to achieve the results of this thesis.

Finally, I want to kindly thank Ms. Nur Engin (NXP) for giving me the chance to work for NXP Semiconductors after this thesis. I am truly blessed that I can continue to work in the field of automotive radar and that I can contribute in such a future-oriented company.

Contents

List of Figures

List of Tables

List of Abbreviations

AACF	Aperiodic Autocorrelation Function
ACCF	Aperiodic Cross-correlation Function
ADC	Analog-to-Digital Converter
AWGN	Additive White Gaussian Noise
BPSK	Binary Phase Shift Keying
CFAR	Constant False Alarm Rate
CMDA	Code Division Multiple Access
DFT	Discrete Fourier Transform
DSP	Digital Signal Processing
ETSI	European Telecommunications Standards Institute
FCC	Federeal Communications Commission
FMCW	Frequency-Modulated Continuous Wave
LPF	Low-pass Filter
LRR	Short Range Radar
MIMO	Multiple-Input Multiple-Output
MRR	Medium Range Radar
PA	Power Amplifier
PACF	Periodic Autocorrelation Function
PCCF	Periodic Cross-correlation Function
PMCW	Phase-Modulated Continuous Wave
RFCMOS	Radio Frequency Complementary Metal Oxide Semiconductor
SINR	Signal-to-Interference-plus-Noise Ratio
SNR	Signal-to-Noise Ratio
SISO	Single-Input Single Output
SRR	Short Range Radar
QPSK	Quadrature Phase Shift Keying

List of Symbols

Symbol	**Name**	**Unit**
R	Range	m
ΔR	Range resolution	m
R_u	Maximum detectable range	m
v	Velocity	$\mathrm{m\,s^{-1}}$
Δv	Velocity resolution	$\mathrm{m\,s^{-1}}$
v_u	Maximum detectable velocity	$\mathrm{m\,s^{-1}}$
θ	Azimuth angle	°
$\Delta\theta$	Azimuth resolution	°
ϕ	Elevation angle	°
P_T	Transmit power	W
P_R	Receive power	W
G_T	Transmit gain	dBi
G_R	Receive gain	dBi
f_c	Carrier frequency	Hz
f_D	Doppler Shift	Hz
λ	Wavelength	m
c	Speed of Light	$\mathrm{m\,s^{-1}}$
σ	Radar cross-section	$\mathrm{dB\,m^{2}}$
k	Boltzmann constant	$\mathrm{m^{2}\,kg\,s^{-2}\,K^{-1}}$
T_{sys}	System temperature	K
B_N	Null-to-null bandwidth	Hz
F_{noise}	Noise figure	
S_L	Receiver Sensitivity	
d_t	Transmit array inter-element spacing	m
d_r	Receive array inter-element spacing	m
d_v	Virtual array inter-element spacing	m
K_T	Number of antennas in transmit array	
K_R	Number of antennas in receive array	
K_v	Number of antennas in virtual array	
L_c	Code length	
T_c	Chip duration	s
T_r	Period duration (PRI)	s
T_{frame}	Frame (or: measurement) duration	s
M	Number of repetitive periods	
R_c	Chip rate	Hz
Z_{cz}	Zero-correlation zone width	
$\mathcal{S}$	Sequence set size	
R_x	Autocorrelation function	
R_{xy}	Cross-correlation function	

Chapter 1

Introduction

The past decade has seen a rapid development of automotive radar sensors, as the demand for driver assistance systems has continued to gain momentum. Since the first sensors were tested in the 1970s [1], there has been significant interest to relieve the driver from the monotonic tasks and split-second decisions within complex traffic situations to improve vehicular safety [2]. However, the dimensions of these early-phase radar systems were immense which lead to poor integration capabilities.

Today, millimeter-wave radar sensors are of high interest, which are being developed using CMOS (Complementary Metal-Oxide Semiconductor) technology. Semiconductor technology offers advantages, such as higher performance, more integration, low power and low costs [2], [3]. This industry is prosperous, as more and more solutions in semiconductor technology, packaging technology, and antenna systems become available [2]. NXP Semiconductors is one of the market leaders in this field and has produced multiple integrated circuits already. Their latest release, *TEF810X Fully-Integrated 77 GHz Radar Transceiver*, is a fully-integrated RFCMOS (Radio Frequency Complementary Metal Oxide Semiconductor) transceiver that is optimized for Multiple-Input Multiple-Output (MIMO) Frequency-Modulated Continuous Wave (FMCW) radar [4].

In the near feature, an increasing number of cars is likely to be deployed with multiple radar sensors to guarantee safety in driving assistance. Each sensor is configured to fulfill its function to establish a distributed sensor network that retrieves a precise observation of the surrounding environment. These functions include adaptive cruise control (ACC), lane change assistant (LCA), cross traffic alert (CTA), and parking assistance. The requirements of each function are defined explicitly for its needs. For example, the ACC needs to be designed to observe a considerable distance in advance of the car, and a broad velocity range to measure significant relative velocities of oncoming vehicles.

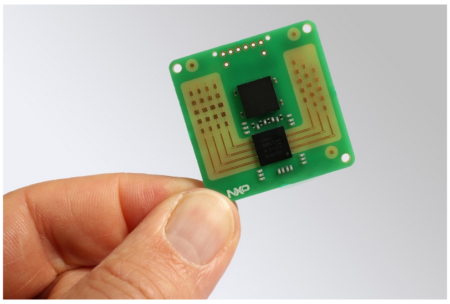

Figure 1.1: Latest chipset by NXP: TEF810X Fully-Integrated 77 GHz Radar Transceiver [4]

In general, three distinctive radar classifications have been defined, namely the Short Range Radar (SRR), Medium Range Radar (MRR) and Long Range Radar (LRR). Table 1.1 illustrates the specifications and vehicular applications for the three radar modes [5]. These specifications have been slightly adjusted to satisfy the wishes of NXP Semiconductors.

Table 1.1: Radar classification modes

Parameter		**Radar Configuration**		
		SRR	MRR	LRR
Maximum transmit power	P_t	$-9\,\mathrm{dBm/MHz}$	$-9\,\mathrm{dBm/MHz}$	$55\,\mathrm{dBm}$
Range resolution	ΔR	$0.05\,\mathrm{m}$	$0.5\,\mathrm{m}$	$1\,\mathrm{m}$
Velocity resolution	Δv	$0.2\,\mathrm{m/s}$	$0.2\,\mathrm{m/s}$	$0.2\,\mathrm{m/s}$
Unambiguous range	R_u	$30\,\mathrm{m}$	$75\,\mathrm{m}$	$250\,\mathrm{m}$
Unambiguous velocity	v_u	$10\,\mathrm{m/s}$	$60\,\mathrm{m/s}$	$60\,\mathrm{m/s}$
Azimuthal field of view	θ	$\pm\,80^\circ$	$\pm 40^\circ$	$\pm 15^\circ$
Elevation field of view	ϕ	$\pm\,10^\circ$	$\pm 5^\circ$	$\pm 5^\circ$
Applications		Park assist; Obstacle detection, Pre-crash	Lane-change assist; cross-traffic alert; Blind-spot detection; Rear-collision warning	Adaptive cruise control

1.1 Measurement Quantities

Currently, automotive radars can estimate the target's range, velocity, and azimuthal angle. Signal processing techniques play an utmost important role in the development of these techniques. Various signal processing techniques are being implemented to provide better resolution and estimation performance in all measurement dimensions: range, velocity, and azimuth-elevation angles. These are respectively written as [2]

$$\Delta R = \frac{c}{2B}\,, \tag{1.1}$$

$$\Delta v = \frac{\lambda}{2\,T_{frame}}\,, \tag{1.2}$$

$$\Delta\theta \approx 0.886\,\frac{\lambda}{d_v(N_v-1)\cos(\theta)}\,. \tag{1.3}$$

where c is the speed of light, B is the transmission bandwidth, T_{frame} is the total duration of a single transmission frame, λ is the wavelength, d_v is the inter-element spacing in the virtual array elements, and N_v is the number of virtual array elements, and the azimuth resolution $\Delta\theta$ is given in radians. These parameters will be explained at a later stage.

Furthermore, this thesis regards a bistatic radar with separate transmit and receive antennas. Each transmit antenna radiates with the transmit power P_T and has a transmit antenna gain G_T. Using Friss' equation, the received power P_R can be calculated deterministically, which depends on the following parameters: receiver gain G_R, radar cross-section of a target σ, wavelength λ and range to the target R. Received signals can be categorized in two partitions: desired and undesired. Here, the desired signal signifies the returns of the transmitted waveform and the undesired signal refers to an interfering source. Desired and undesired received power levels depend on a two-way and one-way propagation of electromagnetic energy, respectively, and are defined as [6]

$$P_{\mathrm{R,D}} = \frac{P_\mathrm{T} G_\mathrm{T} G_\mathrm{R} \lambda^2 \sigma}{(4\pi)^3 R^4}\,, \tag{1.4}$$

$$P_{\mathrm{R,U}} = \frac{P_T G_T G_R \lambda^2}{(4\pi)^2 R^2}\,. \tag{1.5}$$

Unavoidable in electromagnetic receiver antennas is thermal noise, that is proportional to the receiver bandwidth

$$P_N = kT_{sys}B\, F_{noise} = -174 + 10\log_{10}(B) + \, F_{noise} \tag{1.6}$$

where k is the Boltzmann constant and equals $1.38 \cdot 10^{-23}\mathrm{m^2kgs^{-2}K^{-1}}$ and T_{sys} is the system temperature in Kelvin. The kT_{sys} product measures $-174\,\mathrm{dBm/Hz}$, assuming $T_{\mathrm{sys}} = 290\,\mathrm{K}$. Noise figure F_{noise} implies the degradation in SNR caused by the amplifier or radio receiver due to the imperfect receiver RF components.

Well-known measures for signal quality are the Signal-to-Noise Ratio (SNR) and Signal-to-Interference-plus-Noise Ratio (SINR)

$$\mathrm{SNR} = \frac{P_{R,D}}{P_N}\,, \tag{1.7}$$

$$\mathrm{SINR} = \frac{P_{R,D}}{P_N + \sum_i P_{R,Ui}}\,. \tag{1.8}$$

Here, i refers to the i^{th} interferer impinging on the source radar.

Using the SNR, the accuracy for range, velocity, and azimuth angles are respectively given by [2]

$$\delta R = \frac{\Delta R}{\sqrt{2\,\mathrm{SNR}}}\,, \tag{1.9}$$

$$\delta v = \frac{\Delta v}{\sqrt{2\,\mathrm{SNR}}}\,, \tag{1.10}$$

$$\delta \theta = \frac{\Delta \theta}{\sqrt{2\mathrm{SNR}}}\,. \tag{1.11}$$

1.2 Assumptions

Several assumptions and approximations have been taken into account in the MATLAB simulation environment:

1. **Binary sequences**
   In this thesis, the type of codes is constricted to binary codes.

2. **Complex equivalent baseband**
   To reduce simulation time a down-scaled version in frequency was used, instead of the 77-81 GHz frequency span.

3. **Narrowband approximation**
   Received signals and reflections originating from non-static objects are assumed to undergo a Doppler shift instead of a time-scaled version in the case of the wideband receiver. The narrowband approximation holds when $vT_r \ll c/(2B)$ and $B/f_c \ll 1$ [7] [8]. In this thesis, an MRR source radar is considered having a bandwidth $B = R_c = 300\,\mathrm{MHz}$. Therefore, we can assume a *narrowband processor*, as long as

$$v \ll \frac{c}{2BT_{frame}} = \frac{c}{2R_cT_{frame}} = 50\,\mathrm{m/s} \tag{1.12}$$

holds, which is assumed to be sufficient for an MRR radar. Here, T_{frame} is the duration of a single frame of the transmitted signal.

4. **Non-fluctuating targets**
   Peter Swerling developed a set of four statistical models, which are probabilistically defined for the fluctuation behavior of a target's radar cross-section [9]. This thesis considers non-fluctuating targets and is, therefore, time-invariant and angle independent. This model is known as "Swerling 0" Model.

5. **Line-of-sight reception**
   This thesis only considers line-of-sight reflections. Multipath reflections are excluded.

6. **Receiver idealities**
   An idealistic receiver is assumed, which suggests that in the digital stage no receiver clipping, nor quantization errors would harm the digital processing. The impact of analog-to-digital clipping, as well as the quantization process on phase-modulated 79 GHz CMOS radar is investigated in [10].

1.3 Motivation for this study

The previous section explains the increasing importance of automotive radar to assist the driver. Assisted and autonomous driving is expected to erupt with exponential growth in the years to come. This will lead to a significant increase in the use of radar sensors in vehicles on the streets. As every car is to possess multiple radars, the phenomenon of overlapping waveforms in time and frequency cannot be avoided. Therefore, interference between radar systems under these circumstances is very likely to become a practical problem.

Today, frequency modulated continuous wave (FMCW) radars are being implemented, which are conceivably degrading the radar performance with interference being the main plague for the system. Interference mitigation techniques already exist for this type of waveform implementation. However, these do not specifically address and solve the interference issue. Literature has provided a significant interest to replace FMCW waveforms with phase-modulated continuous waveforms (PMCW) radar systems for better interference rejection [3]. However, little is published regarding the interference rejection for PMCW radar systems. Therefore, this thesis will provide a study on to what extent the use of spread-spectrum techniques can alleviate the interference problem for continuous wave radar.

The primary research question that needs to be answered:
Can PMCW waveforms provide improved performance compared to FMCW waveforms in the presence of interference? Here, interference includes self-interference (MIMO), as well as multi-user interference from other radars.

1.4 Novelty in this study

Interference in automotive radar is one of the main concerns in automotive radar. The absence of standardization in waveform design, timing and frequency usage make it a vast and broad problem. However, the urge to solve the interference issue is high, which also reflects the large number of publications in this field.

Thus far, many publications focus on radar-to-radar interference for FMCW radar systems. Goppelt [11], [12] and Brooker [13] explain the interference issue analytically and experimentally. Since these publications, a lot of detection and mitigation publications have been released. First of all, I want to note that Sasanka Sanka did a study on a mitigation technique for radar-to-radar interference in FMCW radar systems, also in collaboration with NXP Semiconductors, for his MSc Thesis at Delft University of Technology [14]. Multiple techniques to detect and mitigate interference are suggested to be applied, i.e., by nulling in time [15], by spatial nulling, by (hybrid) digital beamforming [16]–[18], and by sparse sampling approaches [19], [20].

Few sources on radar-to-radar interference for PMCW radar systems are available due to its infancy. Lately, Beise [21] and Bourdoux [22] published a study on mutual interference between FMCW and PMCW automotive radars. However, the main weakness of this study was the paucity of details, whereas mainly a high-level overview is given.

This thesis aims to contribute novelty in the following aspects:

1. Defining and investigating promising code families for phase-coded automotive radar, which have sub-optimal correlation properties. System design is done for the most auspicious code families with a clear focus on the trade-offs to be made for each individual design. The comparison of the three distinct designs will point out their major benefits and drawbacks.

2. Inspecting the synchronous effects in (16TX) MIMO radar for the selected designs from p1. extensively, with particular attention to orthogonality and computational complexity.

3. Inspecting the asynchronous effects, also known as multi-user interference, and providing a detailed study on radar-to-radar interference in a generalized, non-situation-specific level. The obtained simulation results on radar-to-radar interference will be validated by doing baseband measurements in a loopback test setup.

1.5 Outline of this thesis

The remainder of this thesis is structured as follows:

Chapter 2 Chapter 2 explains the principles and basics of the PMCW radar. It includes a literature overview of a system overview, whereas the transmitter and receiver chains are explained in detail, as well as the signal processing steps. The chapter finalizes with a prognostic, theoretical analysis on interference using the link budget model.

Chapter 3 The literature review continues by denoting and investigating the promising code families. The second part of this chapter is used to explain the approach for designing a PCMW radar. A detailed design strategy and its corresponding trade-off for 16TX MIMO PMCW MRR, specifically for the Gold, ZCZ, and APAS sequences.

Chapter 4 The effects of MIMO orthogonality in phase-coded radar are subject of this chapter, whereas the designs of Chapter 3 are evaluated for: spill-over effects, transmit orthogonality, Doppler tolerance, and computational complexity.

Chapter 5 This chapter focuses on radar-to-radar interference in PMCW radar. Numerous situations are examined to observe the severeness of asynchronous waveforms originating from undesired PMCW, as well as FMCW, vehicular radars.

Chapter 6 In Chapter 6, the analytical and numerical results from the previous chapter are validated by doing experiments with the PARSAX radar, provided by Delft University of Technology.

Chapter 7 Chapter 7 finalizes and concludes this nine-month studies. Also, recommendations will be provided on the possible future work in the field.

Chapter 2

Phase Modulated Continuous Wave Radar

This chapter gives an overview on the state of the art of the phase-modulated continuous wave (PMCW) radar. The fundamentals of the PMCW radar are extensively explained in order to provide a good understanding of its operation. Next, using existing literature, an analysis is presented on the design aspects of signal transmission and reception of the phase-coded signals. Accordingly, Section 2.5 briefly introduces channel access and the essential elements concerning the coexistence of multiple phase-coded signals. Finally, the ambiguities in Doppler and range are addressed.

2.1 Fundamentals

Traditionally, radar systems were equipped with a single transmitter and were generally configured to send out pulsed waveforms [6], [9], [23]. These radars require ultrashort pulses to achieve high range resolution and very high peak power for detecting small targets. One major drawback of the pulsed radar satisfying a high range resolution is that it is therefore unrealizable using small-scale, low-cost hardware and integrated circuits.

In contrast to pulsed radar, the proposed solution is found through range compression which is used to decouple the pulse width from range resolution. By applying pulse compression, a continuous wave (long) pulse can have the same bandwidth as a short pulse by modulating the pulse in frequency or phase. These radar systems have been known as Frequency-modulated Continuous Wave (FMCW) and Phase-modulated Continuous Wave (PMCW) radar systems, respectively. Range resolution is a key metric in every radar system as it denotes the ability to resolve closely situated targets. Richards defines the range resolution in [9] as the main lobe width at the 3-dB point below the peak of the response. In such way, two targets can be resolved in the range domain only if the reflections in time are non-overlying for a duration of T_p. Therefore, the range resolution is proportional to the pulse width, T_p. The range resolution equation is equal to (2.1),

$$\Delta R = \frac{c}{2B} \tag{2.1}$$

where c is the speed of light and B is the bandwidth of a pulse with a duration T_p. PMCW radar systems make use of a spread spectrum technique, that can realize the required high range resolution [6], [9], [23]–[25]. Instead of transmitting a pulse of duration T_p, the technique creates a sequence containing L_c chips. Each chip refers to an individual bit of the code sequence and lasts for T_c seconds, where T_c is inversely proportional to the bandwidth of the transmitted signal,

$$T_c = \frac{1}{B} \tag{2.2}$$

The total duration of a single period is equal to the product of the number of chips and the chip duration, and is denoted by T_r. The duration of a single period is also known as the

Pulse Repetition Interval (PRI). In this thesis, we assume that only binary sequences are transmitted. A binary sequence is a sequence $\alpha_1 \; \alpha_2 \; \ldots \; \alpha_{L_c}$ for L_c bits, i.e. $\alpha_n \in \{-1\,,\,+1\}$ for $n = 1,\,2,\,\ldots,\,L_c$. These discrete binary sequences are modulated to an analog electromagnetic (EM) signal using Binary Phase-Shift Keying (BPSK) modulation. BPSK conveys data by changing the phase of a reference signal, at time instants which are multiples of T_c, based on the value of the consecutive bits

$$\phi_{+1} = 0 \qquad exp(j\,0) = +1 \tag{2.3}$$

$$\phi_{-1} = \pi \qquad exp(j\,\pi) = -1\,. \tag{2.4}$$

Here, the reference signal is a single-carrier wave. BPSK modulates at a rate of 1 bit/symbol. A single period of a binary phase-coded waveform can mathematically be represented as

$$s_p(t) = \sum_{n=0}^{L_c-1} exp(j\phi_n)\;\mathrm{rect}\left(\frac{t - n\,T_c}{T_c}\right) \qquad n = 1, 2, \ldots, L_c \tag{2.5}$$

Here, ϕ_n denotes the phase corresponding to the n^{th} bit of the sequence. The phase is kept constant for the chip duration T_c. As the concurrent chip value changes from -1 to +1, or vice versa, then a phase discontinuity will take place as the phase is shifted 180°. Figure 2.1a illustrates the principle of a phase-coded waveform.

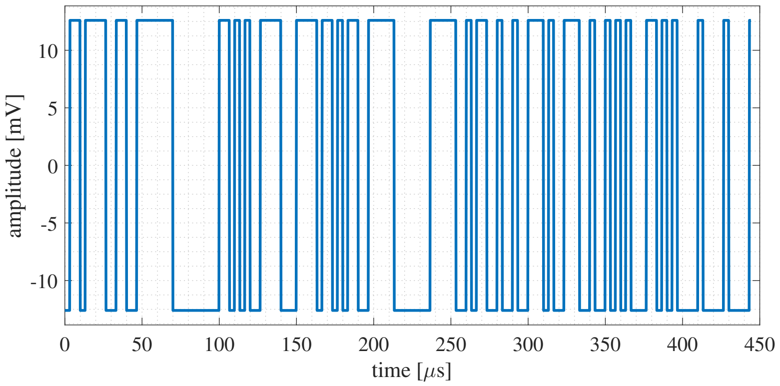

(a) Time domain plot of the first 50 chips

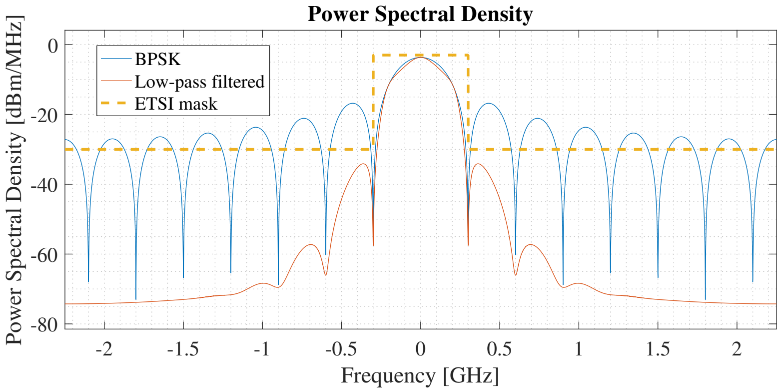

(b) Frequency spectrum

Figure 2.1: Example of a phase-coded waveform (APAS of length $L_c = 1020$ and bandwidth $B = 300$ MHz)

The frequency spectrum of a BPSK-modulated waveform is characterized by its sinc-pattern, as visualized in Figure 2.1b, due to the ideal rectangular pulses in time domain. The main lobe of this spectrum contains all transmitted information; however, energy is spread out in frequency with each side lobe containing similar information as the main lobe. In [26], antenna power transmission limits have been set up by Federal Communications Commission (FCC) for the United States of America to prevent out-of-band interference and avoid the spectrum from becoming too crowded. This thesis treats the European standards, the so-called European Telecommunications Standards Institute (ETSI) spectral mask, which is for MRR and LRR radar systems defined by $-3\,\mathrm{dBm/MHz}$ within the system defined receiver bandwidth B, while outside the receiver bandwidth power spectral density is limited to $-30\,\mathrm{dBm/MHz}$. From 2.1b, one can observe that the side lobes of BPSK-modulated waveform's spectrum are above the spectral mask. Throughout this thesis, to satisfy the requirements on the power spectral density set by the FCC a third-order Chebyshev low-pass filter is applied in the transmitter chain to reduced energy outside the receiver's bandwidth.

From Figure 2.1b, another important remark on the frequency spectrum of a BPSK waveform can be made. First nulls are located at $\pm 1/T_c$ Hz, meaning that the null-to-null bandwidth is twice the bit rate:

$$B_N = 2R_c \tag{2.6}$$

In the remainder of this thesis, the receiver's low-pass filter cut-off frequency is selected at the first null: $f_{cut} = R_c$ Hz. However, in Section 4.2.1 the effects on the autocorrelation properties for different values are analyzed.

Other modulation techniques also exist, which are not restricted to binary sequences. For example, Quadrature Phase Shift Keying (QPSK) can transmit 2 bits/symbol. For poly-phase and unimodular codes, the reader is referred to Chapter 5 of [27].

The duration of a single period is in the order of microseconds. For instance, for a MRR with $B = 300\,\mathrm{MHz}$, $\Delta R = 0.5\,\mathrm{m}$ and $R_{un} = 80\,\mathrm{m}$, hence $L_c \geq 160$, the minimum Pulse Repitition Interval (PRI) measures $T_{frame} = T_r = 53.33\,\mu\mathrm{s}$. In this case, the Doppler resolution of a single pulse is very poor, see (1.2). Thus, we require to increase the measurement duration, called the *dwell time*, to enhance the Doppler resolution by either increasing L_c or repeating a single period multiple times. The effects on this assumption have been analyzed and are explained in Section 2.4. The proposed solution is to repeat a single period M times to increase the measurement time, leading to the transmitting baseband signal

$$\begin{aligned} s_{T,IF}(t) &= \sum_{m=0}^{M-1} s_p(t - mT_r) \\ &= \sum_{m=0}^{M-1} \sum_{n=0}^{L_c-1} exp(j\phi_n)\,\mathrm{rect}\left(\frac{t - n\,T_c - mT_r}{T_c}\right) \end{aligned} \tag{2.7}$$

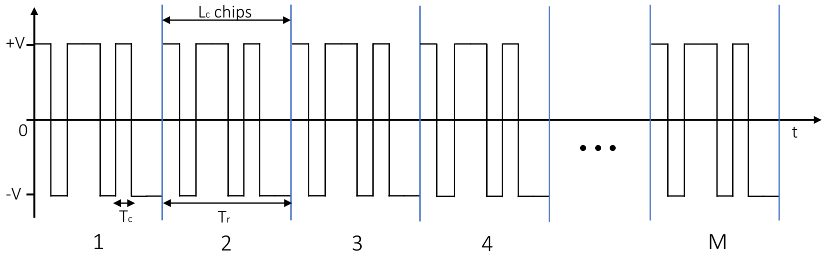

Figure 2.2: Transmission of a multi-period baseband phase-modulated signal

Accordingly, the phase coded signal is continuous having a duty cycle of 100%. The total frame of transmission consists of M ensuing pulses that have a total duration of

$$T_{frame} = M \cdot T_r = M \cdot L_c T_c \tag{2.8}$$

Figure 2.2 illustrates the prior-mentioned timing parameters of a single frame of the phase-coded signal that is generated by the Pseudorandom Code Generator. A architectural overview of the MIMO PMCW system with K_T transmit antennas and K_R receive antennas is given in Figure 2.3. The following two Sections explain the transmitter and receiver chain in more detail.

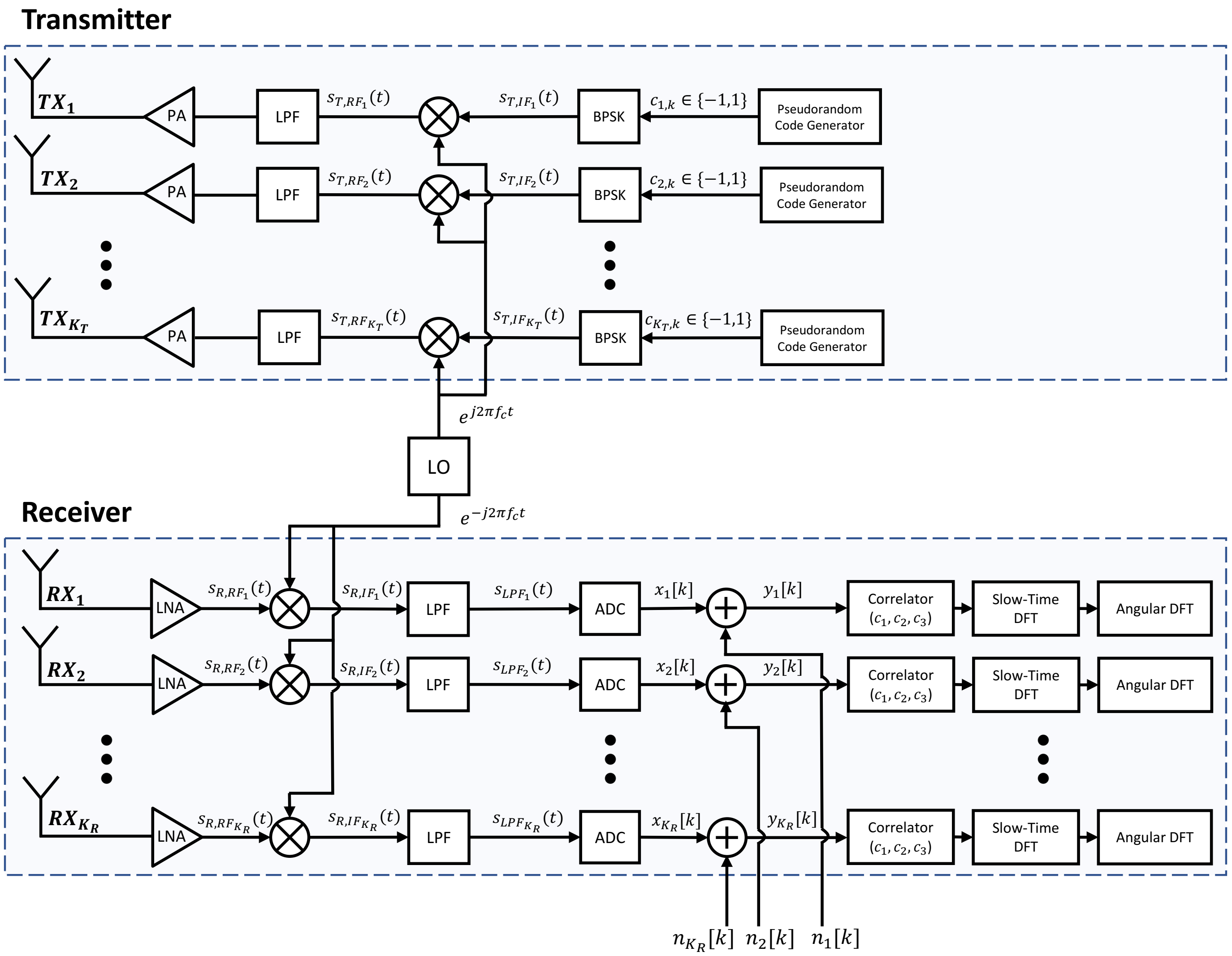

Figure 2.3: Schematic overwiew of the PMCW radar system

2.2 Transmitter

The transmitter is responsible for sending out an electromagnetic signal to a desired direction according to predetermined beamwidth. Figure 2.3 provides a schematic overview of a general PCMW radar system. The transmitter generates a predetermined code generated by the Pseudorandom Code Generator. This code sequence is modulated using the Binary Phase Shift Keying (BPSK) technique (2.7) and up-converted to the carrier frequency f_c using a local oscillator (LO)

$$s_{T,RF}(t) = \Re\left\{ s_{T,IF}(t) \; e^{j2\pi f_c t} \right\} \tag{2.9}$$

after which it is transmitted as EM waves by the antenna.

2.2.1 Pseudorandom Code Generator

The performance of the radar is highly depending on the type of code, also known as code family, being implemented. In recent research, the potential of Code Division Multiple Access (CDMA) has been enlighted to extend its use cases also beyond mobile communications and GPS. Now the principle of code division is also investigated for radar, where all kinds of binary and polyphase sequences are evaluated for the specific application. Recall that this thesis will only consider binary sequences in phase-coded radar. First, let us define, a sequence set S for an arbitrary code family. The set size $\mathcal{S}$ refers to the number of unique binary codes of length L_c. An important measure is the autocorrelation function, which connotes the correlation between a reference signal with a delayed and scaled version of the reference signal as a function of delay. Correlation functions can be periodic or aperiodic depending on the structure of the transmitted sequence. Periodic correlation functions are of interest for phase-modulated continuous wave radar, since its transmission is continuous in order to use the full transmit capacity. On top of that periodic binary sequences can achieve lower sidelobe levels and peak values regarding periodic autocorrelation function (PACF) and periodic cross-correlation function (PCCF), when compared to the aperiodic autocorrelation function (AACF) and the aperiodic cross-correlation function (ACCF) (see Chapter 2.3.3 of [27]). The mathematical expression for the PACF for a sequence x is defined as

$$R_x[k] = \sum_{m=0}^{L_c-1} x[m]x[m+k] \qquad\qquad k = 0, 1, \cdots, L_c - 1 \tag{2.10}$$

where $m + k$ is taken modulo L_c when $m + k > L_c$. The modulo operation accounts for the periodicity in the signal. Perfect autocorrelation properties can be achieved when for $k = 0$ a maximum correlation value is found, known as the *in-phase* value, while the values for all nonzero shifts are equal to zero, also known as *out-of-phase* values.

As the PACF determines the correlation of a sequence with itself, a similar methodology exists to determine the correlation between two distinct sequences within the set $\mathcal{S}$. This periodic cross-correlation function of sequence x and y is given by

$$R_{xy}[k] = \sum_{m=0}^{L_c-1} x[m]y[m+k] \qquad\qquad k = 0, 1, \cdots, L_c - 1 \tag{2.11}$$

where $m + k$ is taken modulo L_c when $m + k > L_c$.

From a radar perspective, all sequences in $\mathcal{S}$ should be orthogonal to each other inducing orthogonal waveforms. Orthogonality means minimization of interference. In order to achieve orthogonality all sequences within set $\mathcal{S}$ should have perfect cross-correlation properties. Ideal cross-correlation properties indicate that for all k shifts the correlation values are zero.

The aim in phase-coded radar is to find a code family that has both perfect autocorrelation properties, as well as perfect cross-correlation properties

$$\begin{aligned} R_x[k] &\neq 0 && \text{for } mod(k, L_c) = 0 \\ R_x[k] &= 0 && \text{for } mod(k, L_c) \neq 0 \\ R_{xy}[k] &= 0 && \text{for all } k \end{aligned} \tag{2.12}$$

However, Skolnik states in [23] that there exists no binary sequence which exhibits both of these properties. They also state that binary sequences can achieve either one of the properties, but not both. Nonetheless, this thesis aims for using existing binary sequences that perform as close to these perfectly defined conditions, which seem to provide great performance in radar. The promising code families are evaluated in Section 3.1 in terms of code length, set sizes, PACF sidelobe levels, and PCCF levels.

Theoretical Lower Bounds

Unavailability of perfect binary sequences has caused several researchers to reach to lower limits for the correlation values. Sarwate [28], Welch [29] and Tang-Fan [30] have defined different lower bounds for different kind of sequences. Throughout this thesis, ϕ_a is used to refer to the maximum sidelobe level of the PACF, whereas ϕ_c is used to refer to the maximum value of the PCCF. Here with $\phi_m = \max\{\phi_a, \phi_c\}$, the famous Welch Bound presents a lower bound for binary sequence

$$\phi_m^2 \geq \frac{(\mathcal{S}-1)L_c^2}{\mathcal{S}L_c - 1} \tag{2.13}$$

Therefore, the Welch Bound depends on the sequence set size $\mathcal{S}$, as well as the code length L_c.

Trade-offs in Code Selection

Until now, we have only discussed the theoretical aspects of the code families. We will now shortly translate these to radar aspects. Since all codes are transmitted consecutively, meaning a duty cycle of 100%, the correlation functions are periodic. Consequently, the distance after range compression between two in-phase peaks is equal to L_c range gates, hence the code length L_c directly corresponds to the maximum unambiguous range

$$R_u = \frac{c\,T_r}{2} = \frac{c\,T_c L_c}{2} \tag{2.14}$$

The repetition period not only directly relates to the maximum unambiguous range. Besides, it also determines the maximum detectable velocity. To estimate both positive and negative velocities, the maximum detectable velocity is

$$|v_u| = \frac{\lambda}{4T_r} = \frac{\lambda}{4T_c L_c} \tag{2.15}$$

Now (2.14) and (2.15) are implying a lower and upper limit respectively for T_r.

$$\frac{2R_u}{cT_c} < L_c < \frac{\lambda}{4\,v_u T_c} \tag{2.16}$$

For MRR Single-Input Single-Output (SISO) radar, with a minimum unambiguous distance $R_u = 75\,\mathrm{m}$ and a minimum unambiguous velocity $v_{max} = 60\,\mathrm{m/s}$ (Table 1.1), these limits have lead to a design restriction in L_c

$$151 < L_{c,_{SISO}} < 4744 \tag{2.17}$$

Besides, the code length determines the peak value of the PACF and has a direct relation to the dynamic range. In Section 3.1, it is shown that the peak of the PACF is equal to L_c for all selected code families. Therefore, the longer the code length, the higher the peak power will be compared to its sidelobes. However, at a later stage in this thesis, it is explained that the code length's relation is decoupled from the dynamic range by processing multiple sequence periods.

The sequence set size $\mathcal{S}$ is another crucial aspect. The size of the set is directly related to the probability that multiple distinct radar systems are transmitting an identical sequence. In this unique case, a PMCW receiver may observe large non-existing targets at a distance $R_{\text{INT}}/2$, where R_{INT} is the distance from the source radar to the interfering radar that is transmitting at the same time in the same spectrum. Such a target is usually referred to as a *ghost target*. Also, MIMO PMCW radar sets specific requirements on the sequence set size. Namely, every antenna element transmits a unique sequence simultaneously. Therefore, the set size $\mathcal{S}$ should be at least the size of the transmit channel accesses K_T. Assuming that $K_T = 16$ and the maximum code length of (2.17) is used, we find the theoretically defined lowest possible correlation level ϕ_m by filling in the Welch Bound of (2.13)

$$\phi_m = \sqrt{\frac{15 \cdot 4744^2}{16 \cdot 4744 - 1}} = 66.7 \tag{2.18}$$

which reflects the theoretical correlation limits of binary sequences in MIMO system design. These implications in system design are further explained in Section 3.3.

2.3 Receiver

The receiver's RF front-end consists of at least one antenna that converts the reflected electromagnetic waves into an electrical signal. The lower block in Figure 2.3 illustrates the receiver chain of K_R receiver antennas from the RF front-end until the signal processing stage.

The analog RF bandpass signal $s_{R,RF}(t)$, which is received from the antenna package, is amplified by a Low-Noise Amplifier (LNA). The received RF bandpass signal $s_{R,RF}(t)$ is an amplitude-scaled and time-delayed version of the transmitted signal, $s_{T,RF}(t)$, and can be written as

$$\begin{aligned} s_{R,RF}(t) &= \Re\left\{\beta\, s_{T,RF}\left(t-\tau\right)\, e^{j2\pi f_c(t-\tau)}\right\} \\ &= \Re\left\{\beta\, s_{T,RF}\left(t-\frac{2(R_0+vt)}{c}\right)\, e^{j2\pi f_c t}\, e^{-j2\pi f_c \frac{2(R_0+vt)}{c}}\right\} \\ &= \Re\left\{\beta\, s_{T,RF}\left(t-\frac{2(R_0+vt)}{c}\right)\, e^{j2\pi f_c t}\, e^{-j\frac{4\pi R_0}{\lambda}}\, e^{-j2\pi \frac{2v}{\lambda} t}\right\} \\ &= \Re\left\{\beta\, s_{T,RF}\left(t-\frac{2(R_0+vt)}{c}\right)\, e^{j2\pi f_c t}\, e^{-j\frac{4\pi R_0}{\lambda}}\, e^{-j2\pi f_D t}\right\} \end{aligned} \tag{2.19}$$

where the propagation delay is given by $\tau = 2(R_0 + vt)/c$ and β is denoted as the magnitude of the received signal according to path loss model as in (1.4). From the narrowband approximation we can conclude that the signal experiences a Doppler shift $f_D = 2v/\lambda$, in case it is reflected from a moving target.

After the LNA, the RF signal, $s_{R,RF}(t)$, is down-converted by multiplying it with the coherent local oscillator's (LO) reference signal; with coherency meaning that it is identical in carrier frequency and phase. The real-valued bandpass signal with center frequency f_c may be written as

$$s_{R,RF}(t) = \Re\left\{s_{R,IF}(t)e^{j2\pi f_c t}\right\} = x(t)\cos(2\pi f_c t) - y(t)\sin(2\pi f_c t) \tag{2.20}$$

where $s_{R,IF}(t)$ is called complex baseband signal, and $x(t)$ and $y(t)$ are the in-phase (I) and quadrature (Q) components of $s_{R,IF}(t)$. The I and Q components contain the BPSK-modulated transmitted symbols. After the local oscillator, the down-converted (IF) signal is low-pass filtered (LPF) to eliminate all out-of-band interference.

$$s_{LPF}(t) = \text{LPF}\left\{s_{R,IF}(t)\right\} \tag{2.21}$$

The complex analog baseband signal is then transmuted into a sampled, digital complex baseband signal, $x[k]$, using a complex ADC. At this point in the receiver chain, zero-mean and complex Additive White Gaussian Noise (AWGN), $n[k]$, with variance σ_n^2 is also sampled together with the complex sampled signal $x[k]$

$$y[k] = x[k] + n[k] \tag{2.22}$$

where the noise distribution is given by $n \sim \mathcal{N}(0, \sigma_n^2)$. The variance of the AWGN noise can be retrieved from the thermal noise power, P_N, as defined in (1.6).

Then, the received samples, $y[k]$, arrive at the stage where digital signal processing (DSP) takes place. Next steps are to retrieve the range profiles and estimate the environment's velocity. Figure 2.3 provides an overview of two critical signal processing stages in PMCW radar, namely the Sliding correlator and the Doppler processor. Respectively, these are explained in Section 2.3.1 and 2.3.2. The sliding correlator is implemented using a discrete matched filter.

The Doppler processor coherently processes the consecutive correlated periods to estimate velocities of possible targets.

2.3.1 Range Correlation

In radar, range profiles are generally retrieved by applying a matched filter, where the matched filter is a conjugated time-reversed version of the transmitted signal. Figure 2.3 implies that for phase-coded radar, the matched filter is implemented in the digital domain. A matched filter for the entire measurement frame, consisting of M periods, is equal to the entire transmitted frame of M sequences (2.7), namely

$$\mathbf{h} = \mathbf{1} \otimes \mathbf{c}\,, \tag{2.23}$$

where $\mathbf{1}$ is the all-one vector sized $(1 \times M)$, and the operation $\otimes$ is referred to the Kronecker product. For large M, the matched filter implementation of the entire pulse burst waveform becomes computationally expensive. Richards states in Section 4.5.2 of [6] that rather a matched filter can be implemented using a single-pulse matched filter,

$$\mathbf{h} = \mathbf{c} \tag{2.24}$$

after which the outputs are combined. When the sampling frequency is configured to be equal to the bit rate $F_s = R_c$ Hz, the duration between two consecutive samples is equal to T_{chip}. Then, for every multiple of T_{chip} the last L_c samples of $\mathbf{y}$ are compared to the transmitted code sequence $\mathbf{c}$

$$\begin{aligned} r[k] &= \sum_{l=0}^{L_c-1} h[l]y[k-l] \\ &= \sum_{l=0}^{L_c-1} c[l]\big(x[k-l] + n[k-l]\big)\,. \end{aligned} \tag{2.25}$$

The actual implementation is therefore done using a sliding correlator that implements a correlation for all possible delays. Figure 2.4 shows the setup. It needs $(L_c - 1)$ delay elements and L_c multiplications.

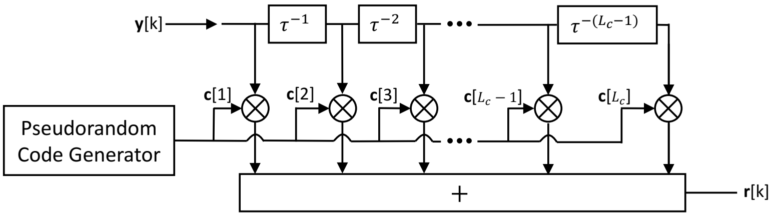

Figure 2.4: Principle of the Sliding Correlator

The output $\mathbf{y}_m$ for the m^{th} pulse results in the periodic autocorrelation function that has been described for each specific code sequence in the previous section. Recall from Section 2.2.1 that the maximum processing gain that can be achieved by correlating the received signal with a single-period reference code equals

$$G_{p,corr} = BT_r = \frac{1}{T_c} L_c T_c = L_c \tag{2.26}$$

which indeed is equal to the *time-bandwidth product*. The time-bandwidth product represents the maximum achievable gain when the reflected signals are completely on-grid in time and frequency.

Figures 2.5a and 2.5b show the output of a M-sequence with $L_c = 1023$. For the static target at $R_0 = 20\,\mathrm{m}$, the target is located in range gate 40, since $\Delta R = 0.5\,\mathrm{m}$. The recurrent pattern of the main peak reflects the periodicity in the waveform, which is located in samples: $40 + 1023 \cdot k$, where k depicts the slow-time index. This case exemplifies that it works for a single target. However, this could be extended to any arbitrary number of targets, because the processing steps are linear operations.

In case there appears to be a relative velocity among the source and the target, the pattern of Figure 2.5a is slightly adjusted. The relative speed causes the reflected waveform to exhibit an additional complex phase shift. The next subsection explains how to retrieve the relative velocity from the complex waveform. Due to the narrowband approximation, the *stop-and-hop approximation* claims that the target's relative movement is negligible over the measurement duration. Therefore, the target's distance is not smeared over multiple range gates.

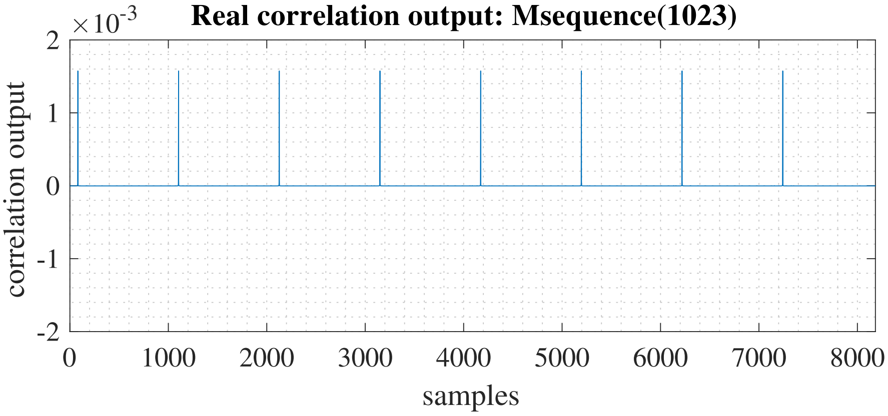

(a) Single stationary target at $R = 20\,\mathrm{m}$.

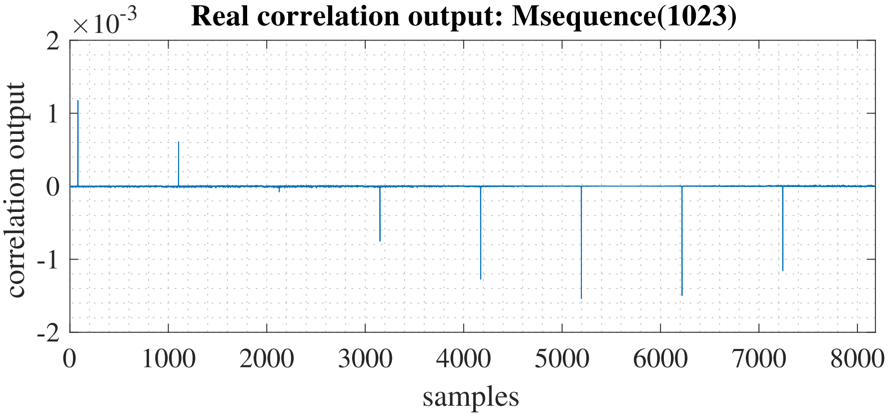

(b) Single moving target at $R = 20\,\mathrm{m}$ with $v = 40\,\mathrm{m/s}$.

Figure 2.5: Real Output of the Sliding Correlator for M-sequence (1023)

2.3.2 Doppler Processing

After correlation, the next stage in the receiver chain is coherent processing. M correlator outputs, given as $\mathbf{r}_m$ individually, of length L_c are stacked in a two-dimensional matrix $\mathbf{R}$ of size $M \times L_c$. From (2.19), we can observe that the time-dependent delay causes a frequency shift among the successive $\mathbf{y}_i$ known as the Doppler shift $f_D = \pm 2v/\lambda$. This phenomenon is represented in figure 2.5b. For longer code lengths, we observe that the correlator output becomes more corrupted as the main peak decreases in amplitude. Besides, range sidelobes start to appear for all lags, which effect is further discussed in Section 4.3.1.

The individual outputs $\mathbf{r}_m$ are similar when the targets are static (as shown in Figure 2.5a). On the other hand, if the targets are moving, the correlator outputs $\mathbf{r}_m$ will experience a phase shift caused by the velocity of the targets (see Figure 2.5b). In order to do velocity estimation, Discrete Fourier Transform is applied over N_s slow time samples

$$\mathbf{R}(m,n) = \frac{1}{N_s} \sum_{k=0}^{N_s-1} \mathbf{r}_m[k] \cdot e^{-j2\pi \frac{n}{N_s} k} \tag{2.27}$$

where N_s is the number of slow time samples and equals the FFT-length, and k describes the discrete Doppler frequency index.

In each Fourier transform the signals add up coherently, resulting in a total power gain of M^2. On the other hand, noise adds up stochastically. Hence, it experiences a power gain of M. Therefore, the gain from Doppler processing is equal to

$$G_{p,coh} = M\,. \tag{2.28}$$

The total gain that can be achieved, after correlation and coherent processing, is equal to

$$G_p = G_{p,coh} \cdot G_{p,corr} = ML_c \tag{2.29}$$

which is equal to the time-bandwidth product of the entire code.

2.4 Range and Doppler ambiguities

In general, phase-coded waveforms perform excellently when Doppler is minimal. However, in the presence of Doppler, their performance degrades dramatically due to the frequency shifts caused by Doppler effects (narrowband assumption) [25].

To investigate the Doppler effects on the matched filter's performance, a distinctive tool to use is the ambiguity function. There have been two different types of ambiguity functions specified, namely narrowband ambiguity function (AF) and wideband ambiguity function (WAF) [7]. The ambiguity function is critical for designing the radar's waveform and is useful for examining the range and Doppler resolution, side lobe behavior, range-Doppler coupling and range and Doppler ambiguities [6]. The narrowband ambiguity function is generally defined as

$$\chi(\tau, v) = \int s(t) s^*(t-\tau) e^{j2\pi v t} dt \tag{2.30}$$

where $s(t)$ is a periodic sequence containing M periods.

Our goal is to design the "ideal ambiguity function" according to the intent of the system design. The ambiguity function of the phase-coded radar has a thumbtack shape, which is commonly cited as ideal [31], [32]. Ideally, the ambiguity function can be distinguished by a single narrow peak for zero-delay ($\tau = 0$) and zero-Doppler ($v = 0$) and its remaining energy spread uniformly over the delay-Doppler plane for non-zero delays and non-zero frequency shifts. The spike shape implies high resolution in both range and velocity, while the low and uniform plateau entails a flat noise floor and no significant side lobes. This means enhanced performances in terms of minimum target masking effects, and therefore, increased detection capabilities for far-away located targets or having low radar cross sections.

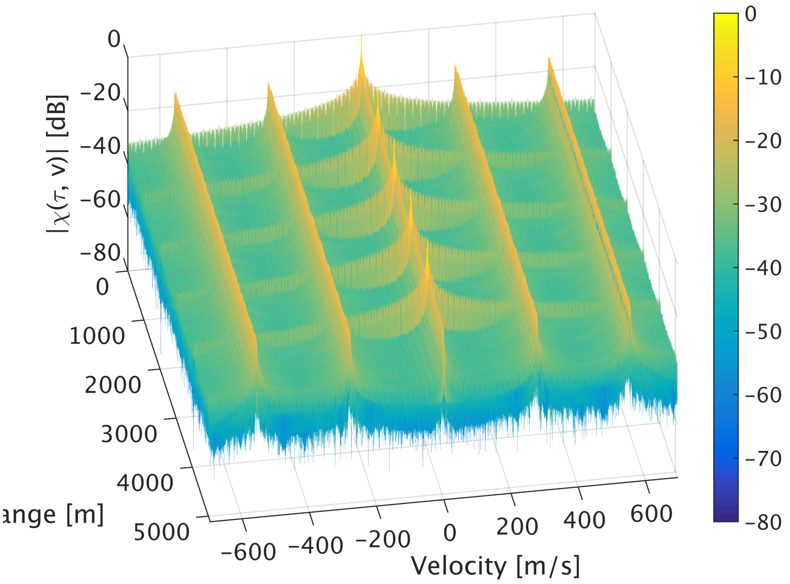

Figure 2.6: Ambiguity Function for a phase-coded waveform of a Gold(2047) sequence.

Figure 2.6 displays the ambiguous region for an MRR Gold-coded waveform, with $L_c = 2047$ and $T_{frame} = 1\,\text{ms}$ (hence $M = 146$). The illustration is limited to five-period durations in time to provide an understanding of the ambiguities that arise. For a coherent pulse train (CPT), the ambiguity function looks like a bed of nails, where the nails arise at $\tau = nT_r$ and $f_D = m/T_r$ with $n = \pm 1, \pm 2, \ldots$ and $m = \pm 1, \pm 2, \ldots$. For phase-modulated waveforms, there is one major difference, which is that for $f_D = m/T_r$, instead of nails, a ridge is found over the full range in the former Doppler bin.

Respectively, the maximum unambiguous range and velocity for this specific setup can be defined by Equations (2.14) and (2.15), which can be retrieved at multiples of

$$R_u = 1022.8\,\text{m} \qquad \text{and} \qquad v_u = 278.1\,\text{m/s} \tag{2.31}$$

As mentioned before, the code length L_c determines the lower and upper limit for respectively R_u and v_u, which implies that a trade-off is to be made in the design configurations of the desired phase-coded radar. Not to mention the constraints in code length for the code generation from certain families. The specific properties of certain code families, as well as the mentioned trade-offs and restrictions, are further addressed in Chapter 3.

Another useful property of the PAF is that it provides insight on the sidelobe levels in range and in Doppler. In range, the expected sidelobe levels are according to the PACF of the specific code, for the the case of no Doppler shift. In velocity, the sidelobe levels behave to are sinc-shaped, where the first sidelobe measures $-13.46\,\text{dB}$ with respect to the main lobe.

2.5 Channel Access

Before proceeding to the design aspects for the MIMO PMCW radar, it is necessary to articulate the radar principles to the problem of this thesis; interference in PMCW radars. This section provides an introduction to the two distinct types of interference in PMCW radar and should act as preliminary knowledge for the actual design choices being made in Chapter 4 and 5. The MIMO configuration causes the first case of channel access, as multiple waveforms are excited simultaneously. Secondly, radar-to-radar interference is another class of channel access, which is less controllable due to the lack of standardization.

2.5.1 Self-Interference

Multiple Input Multiple Output (MIMO) radar indicates a radar system consisting of multiple transmitters and receivers. Traditionally, MIMO radar is either implemented using Time-Domain Multiplexing (TDM) or Frequency Domain Multiplexing (FDM) in FMCW radar. In the last decade, FMCW radar systems also aim to have transmitters radiating simultaneously through different multiplexing techniques. Some of these techniques are frequency-division and code division [33], frequency-division using multiple TX- beamforming [34] and time-staggered chirps [35].

This thesis intents for full transmit capacity and is restricted only to MIMO configurations, for which the transmitting antennas radiate simultaneously, only. Therefore, MIMO PMCW aims for orthogonal waveforms. However, in practice, this orthogonality is not always achievable. Interference susceptibility depends heavily on these correlation properties of the codes and the impact of the correlation operation in the presence of Doppler. Section 3.1 provides an overview of the different codes and its Doppler tolerance.

The main advantage of a full channel capacity MIMO setup is that it enables to estimate on the direction of arrival (DoA). This is an impending feature for automotive radars. Other advantages of MIMO systems are increased spatial resolution, increased antenna aperture and higher sensitivity to detect slowly moving object [36]. Direction of arrival can be explained using the virtual array concept, which is described below.

Virtual Array Concept

As stated above, in order to obtain the angular position of a target, a radar system should consist of at least multiple transmitters or receivers. Then, from the additional distance covered, the angle of incidence can be found by the phase delays in reception. For narrowband signals (we concluded that we use narrowband assumption, see Section 1.2) when time delay τ_i is small compared to the inverse bandwidth of $x(t)$, we can claim that the difference among the array elements is just a phase shift [37]

$$\begin{aligned} x_{\tau_i}(t) :&= x(t-\tau_i)\, e^{-j2\pi f_c \tau_i} && (2.32)\\ &\approx x(t)\, e^{-j2\pi f_c \tau_i} && (2.33)\\ &= x(t)\, e^{j2\pi \Delta_i sin(\theta)} && (2.34) \end{aligned}$$

where $\Delta_i = d_{t,i}/\lambda$ is the inter-elements spacing in wavelength between the first antenna element of the array to the i^{th} antenna element and θ defines the target direction.

For simplicity, a uniform linear array (ULA) has been selected for both the transmitter and receiver array. The distance between the transmitting elements d_t and receiving elements d_r is equal to $\lambda/2$. The arrays consist of K_T transmitting antennas and K_R receiving antennas.

The RF waveform of the k^{th}-transmitting antenna, as in (2.9), in direction θ is given as

$$x_k(t,\theta) = s_{T,k}(t)\, e^{j2\pi \frac{d_t k \sin(\theta)}{\lambda}} \tag{2.35}$$

with $k = 0, 1, \dots, K_T - 1$. Equivalent vector model denotes the combined signal, in far field, as

$$x(t,\theta) = \mathbf{a}_T(\theta)^T \mathbf{s}_T(t) \tag{2.36}$$

where the complex exponential, denoting the phase shift among the transmitting sources, is endowed in the directional vector

$$\mathbf{a}_T(\theta) = \begin{bmatrix} 1 \\ e^{j2\pi d_T \sin(\theta)/\lambda} \\ \vdots \\ e^{j2\pi d_T (K_T-1) \sin(\theta)/\lambda} \end{bmatrix} \tag{2.37}$$

Let us assume that omnidirectional transmitters and receivers are deployed and have a uniform beam pattern for $-90^\circ \leq \theta \leq 90^\circ$. Also, the assumption is made that only line-of-sight rays are received. Therefore, defining L targets, the received signals at K_R receiving elements is given as

$$\begin{aligned} \mathbf{s}_R(t) &= \sum_{l=1}^{L} \beta_l\, \mathbf{a}_R(\theta_l)\, x(t-\tau_l, \theta_l) \\ &= \sum_{l=1}^{L} \beta_l\, \mathbf{a}_R(\theta_l)\, \mathbf{a}_T(\theta_l)^T \mathbf{s}_T(t-\tau_l) \end{aligned} \tag{2.38}$$

Here, β is the path attenuation coefficient according to the path loss model, and again

$$\mathbf{a}_R(\theta) = \begin{bmatrix} 1 \\ e^{j2\pi d_R \sin(\theta)/\lambda} \\ \vdots \\ e^{j2\pi d_R (K_R-1) \sin(\theta)/\lambda} \end{bmatrix} \tag{2.39}$$

refers to the receive directional vector. For unique parameter estimation, we need a proper selection of transmit and receive geometry (d_t and d_r). From (2.38) follows that the received signal is composed of $K_T K_R$ signals, based on different phase centers. The phase centers are present due to the differences in path lengths Δ_i in the receiving and transmitting arrays. A uniform linear virtual array is assured for $d_T = d_R K_R$, where d_R should not exceed $\lambda/2$ to avoid grating lobes on reception. Then, using Figure 2.7, a steering vector of the virtual array can be found by multiplying every element of the transmission steering vector with all the elements of the receiver steering vector and concatenate all the multiplication results to form one vector. Mathematically, the Kronecker product of $\mathbf{a}_t(\theta)$ and $\mathbf{a}_r(\theta)$ is used to generate the steering vector of the virtual array

$$\mathbf{a}_v(\theta) = \mathbf{a}_t(\theta) \otimes \mathbf{a}_r(\theta) = \begin{bmatrix} 1 \\ e^{j2\pi d_R \sin(\theta)/\lambda} \\ \vdots \\ e^{j2\pi d_T \sin(\theta)/\lambda} \\ e^{j2\pi (d_T + d_R) \sin(\theta)/\lambda} \\ \vdots \\ e^{j2\pi (d_T (K_T-1) + d_R (K_R-1)) \sin(\theta)/\lambda} \end{bmatrix} \tag{2.40}$$

The phase delays caused from each transmitting antenna to each receiving antenna can be found from the 2D-processed data, which has been explained in Section 2.3.2. This is done using a *data cube*, $z(l, m, n)$, where the l dimension is fast time; m dimension is slow time; and n dimension refers to the spatial sampling for the individual channels (See Chapter 3.1 of [9]).

Similar to the DFT taken along the slow-time samples, from (2.40) we observe an exponential dependency along the spatial samples. Different approaches on recent directional beamforming techniques can be applied [38], which are outside the scope of this thesis, but using the conventional DFT method the direction of arrival can be estimated

$$\begin{aligned} Z(l,p,n) &= \frac{1}{K_T K_R} \sum_{k=0}^{K_T K_R - 1} z_l[p,k] \cdot e^{-j2\pi \frac{n}{K_T K_R} k} \\ &= \frac{1}{K_T K_R} \sum_{k=0}^{K_T K_R - 1} z_l[p,k] \cdot e^{-j2\pi \frac{d_v sin(\theta)}{\lambda} k} \end{aligned} \tag{2.41}$$

where p denotes the velocity bin of the target. Then, the N_{FFT}-point output for velocity bin p and range gate l results in the following angular dependency θ

$$\theta = \sin^{-1}\left(\frac{n\lambda}{d_v K_T K_R}\right) \tag{2.42}$$

where n denotes the n^{th} angular FFT bin.

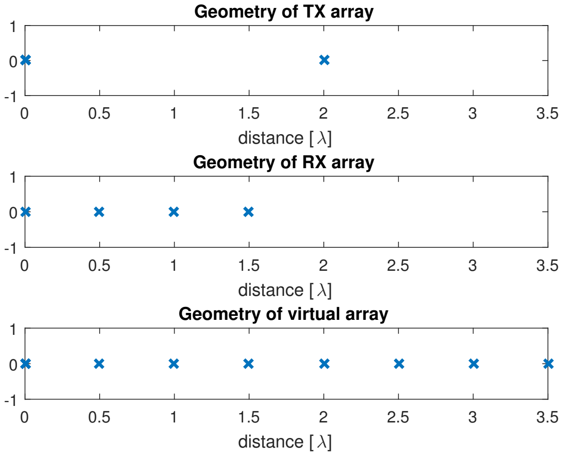

Figure 2.7: Geometry of receiver, transmitter and virtual array, with inter-element spacing: $d_t = 2\lambda$, $d_r = \lambda/2$, and $d_v = \lambda/2$.

2.5.2 Multi-user Interference

Multi-user interference is a substantial open problem, where a lot of random variables exist. Despite the lack of standardization in automotive radar, extensive analysis is required to observe the influences of other automobiles on the PMCW radar system and how to mitigate this interference. In [39], Bourdoux has given a superficial analysis based on a few computer simulations. This thesis isolates the problem by observing the two independent SISO signals having different center frequency f_c, bandwidth B, code length L_c, code family S or time-domain overlap. Therefore, this type of interference is referred to as *asynchronous interference*.

In worst case scenario, we can do a theoretical analysis using the path loss model to provide a benchmark for the numerical and practical study on asynchronous interference given in Chapter 5. In this scenario, interference overlays entirely in time and frequency with the source signal. By considering an MRR radar, with the system parameters as given in Table 2.1. This link budget analysis considers a single target and single interference, where power spectral densities, expressed in dBm/Hz, are used, meaning that the absolute power levels are normalized to the receiver bandwidth.

In this setup, the receiver bandwidth amounts for twice the bitrate, and thus equals the null-to-null bandwidth. The inferred noise figure, F_{noise}, equals 15 dB. Then, the noise power spectral density is

$$P_N = -174 + F = -174 + 15 = 159\,\mathrm{dBm/Hz}$$

Table 2.1: Link Budget Analysis

Parameter		Source	Interferer
Transmit power	P_T	10 dBm	10 dBm
Center Frequency	f_c	79 GHz	79 GHz
Transmitter Gain	G_T	12 dBi	12 dBi
Receiver Gain	G_R	12 dBi	-
Chip rate	R_c	300 MHz	-
Receive Bandwidth	B_N	600 MHz	300 MHz
Thermal Temperature	kT_{sys}	−174 dBm/Hz	-
Noise Figure	F_{Noise}	15 dB	-
Period Duration	T_r	12.89 µs	12.89 µs
Frame Duration	T_{frame}	10.9 ms	10.9 ms

Using P_T, G_T, G_R, σ, and λ from Table 2.1 the received power can be derived from (1.4). The received power from target reflections, whose distances vary from 0 m to 100 m, have been displayed in Figure 2.8. Assuming that the theoretical processing gain from (2.29) is unaffected, the red curve in the image represents the power of the processed waveform.

Unlike the two-way propagation path from the desired signal, interference power illuminates the source radar in one-way propagation as denoted in (1.5). Figure 2.8 illustrates the interference power at consistent distances of $R_{INT} = 1, 10, 40$ m. Now we can easily interpret for which target distances, the reflected signal is superior to the interference.

In theory, this analysis expects that the interference power relates to an increase in the noise floor, as the sum of powers. However, this is not so trivial. In Chapter 6, the influence of interference on the source radar will be inspected and compared to the power levels in this link budget analysis.

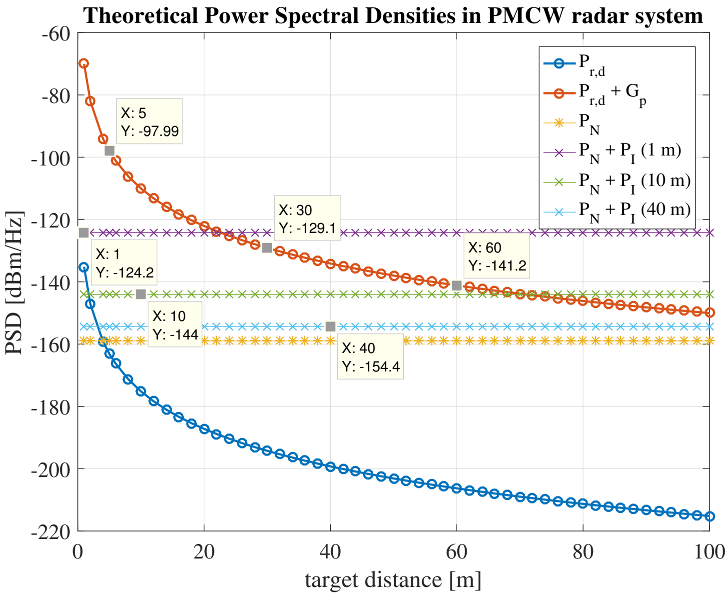

Figure 2.8: Theoretical Power Spectral Density for an MRR phase-coded radar system.

Chapter 3

Design Choices for MIMO PMCW Automotive Radar

The following part of this thesis moves on to describe in greater detail the importance of several design choices and trade-offs that are unavoidable. Section 3.1 signifies the existing code families and its properties. The autocorrelation properties of every code family are also inspected in the presence of Doppler using the periodic ambiguity function (in Section 3.2). Then, in Section 3.3 these codes are translated into distinctive choices that should lead to the design of PMCW MIMO radar systems.

3.1 Code Family Candidates

Several code families are investigated in order to exploit the most desirable properties in the system design: orthogonality, side lobe levels, sequence set size and available code lengths. The to be reviewed code families are M-sequences, Gold and Kasami sequences, Almost Perfect Autocorrelation Sequences (APAS) and the Zero-correlation Zone (ZCZ) sequences. These codes are currently the most popular codes for automotive radar.

3.1.1 M-sequence

Maximal length shift register sequences, or so-called M-sequences, constitute one of the most important classes of pseudo random sequences [27]. M-sequences are generated by a linear feedback shift register (LFSR) containing n shift registers. The feedback loops are usually described by a generator polynomial, e.g.

$$g(x) = a_{n-1}z^{n-1} + \ldots + a_1 z + a_0 \tag{3.1}$$

Here, the coefficient a^k represents a connection from the k^{th} register to the adder. Figure 3.1 illustrates the connections between the registers and the adders. The binary M-sequence is constructed from the output of register R_n for every cycle. The initial state of the shift registers can take up any binary realization, except the all-zero state. Therefore, $2^n - 1$ possible initial shift register states result in $\mathcal{S}_M = 2^n - 1$ different code sequences.

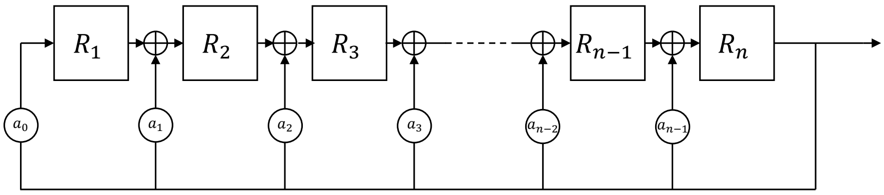

Figure 3.1: Representation of a Galois Linear Feedback Shift Register (LFSR)

The periodic autocorrelation function of m-sequences is 2-valued; that is the in-phase value and out-of-phase values. Its in-phase value measures $2^n - 1$, while its out-of-phase values are equal to -1 [23]. The autocorrelation function sidelobe levels perform below the famous Welch Bound and the theoretically defined maximum ACF/CCF sidelobe levels, as visualized in Figure 3.2a. These exceptional autocorrelation properties of the M-sequence come in pair with dramatic cross-correlation characteristics. For only a few sequences in the established sequence set, which is generated using the same generator polynomial with different initial register states, the preferred cross-correlation function is found (see Figure 3.2b), which are:

$$R_{x,y}(k) \in \left\{ -1 \ , \ -1 - 2^{(n+l)/2} \ , \ -1 + 2^{(n+l)/2} \right\} \tag{3.2}$$

where $l = 1$ for odd n and $l = 2$ for even n. This subset of m-sequences is known as *preferred m-sequences*. There are only few *preferred* m-sequences; just 6 for the 127-bit m-sequence, which are not sufficient for multiple access applications [40]. Non-*preferred m-sequences* have poor cross-correlation behavior: either increased cross-correlation values (compared to the values from Figure 3.2b), or a cross-correlation pattern similar to the autocorrelation function, only having two peaks of $2^n - 1$ amplitude.

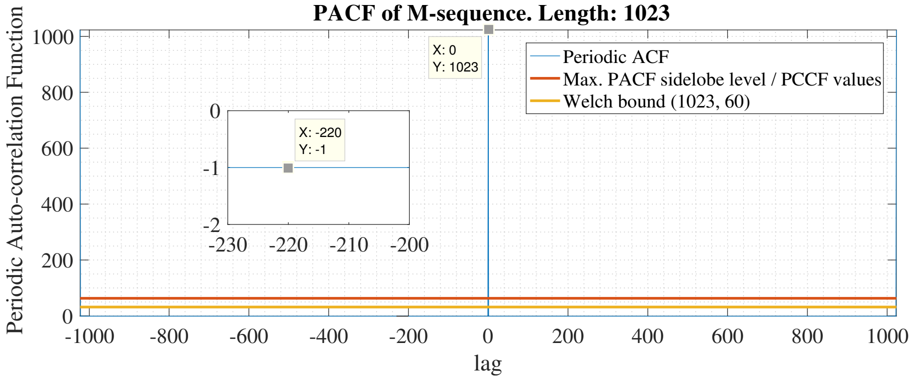

(a) Periodic Autocorrelation Function

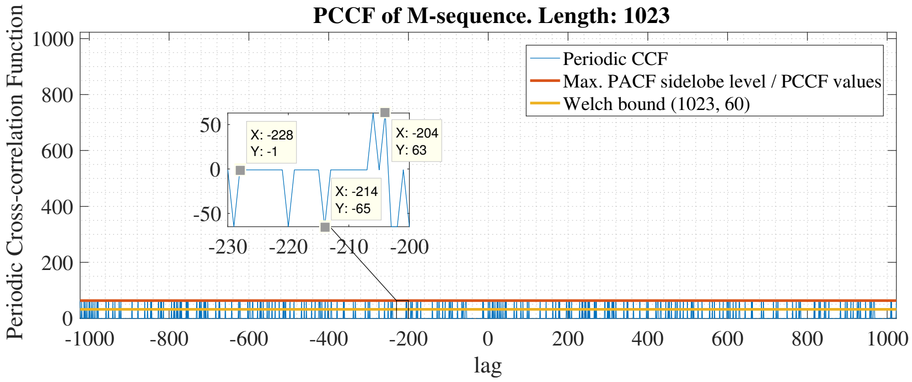

(b) Periodic Cross-correlation Function

Figure 3.2: PACF and PCCF: preferred M-sequences (1023)

3.1.2 Gold and Kasami Sequences

Two other binary spreading code classes are Gold and Kasami codes and are generated using *preferred* m-sequences. Both classes of sequences have controlled correlation properties [40].

Gold Gold codes are nowadays implemented in telecommunications (CDMA) and satellite communications (GPS). This type of application takes advantage of the fact that large sets of sequences can be generated with relatively good cross-correlation properties [27]. Also, the sets can be easily constructed using only two *preffered* m-sequence.

The Gold sequence is of length $L_c = 2^n - 1$ and is generated from two *preferred m-sequences* that are circularly shifted and modulo-2 added. However, the number of shift registers n must satisfy mod(n,2)=1 or mod(n,4)=2 [27], Chapter 4.4.2. The resulting Gold code set $S_G(\mathbf{a}, \mathbf{b})$ of period L_c, of a selected *preferred m-sequences* pair **a** and **b**, can mathematically be represented as $\mathbf{a} \otimes D^l \mathbf{b}$ with $l = 0, 1, \ldots, L_c - 1$. The operator D represents a shift to the periodic sequence by l positions to the right. Then, the set size contains **a**, **b** and $(2^n - 2)$ shifted versions of **b**, therefore, resulting in a sequence set size is equal of $\mathcal{S}_G = 2^n + 1$.

Kasami Kasami sequences can be subdivided into Kasami sequence with small sets and large sets. Small sets of Kasami sequences are generated using two m-sequences and are again of length $L_c = 2^n - 1$. The construction of the sequences c_i is based on decimating one m-sequence $\mathbf{a}_{ir}$ and a non-decimated m-sequence $\mathbf{b}_i$. Similar to the construction of Gold sequences, $\mathbf{a}_{ir}$ and $\mathbf{b}_i$ will be circularly shifted and modulo-2 added. The decimation factor r is

$$r = 2^{n/2} + 1 \tag{3.3}$$

The sequence set size of Kasami (small set) sequences is determined as $\mathcal{S}_{Ks} = 2^{n/2}$, which shows that $\mathcal{S}_{Ks} < \mathcal{S}_G$.
As the name initiates, large sets of Kasami sequences contain a larger number of sequences in the set compared to small sets of Kasami sequences. Large sets of Kasami sequences are not constructed using two preferred m-sequences; instead, three preferred m-sequences are used. The large set contains the small set, as well as a set of Gold sequences, and an additional set generated by shifting a third preferred m-sequence with the set of Gold sequences [27]. However, the construction of Kasami (large sets) exists only for lengths of $L_c = 2^n - 1$ with $\bmod\ (n, 4) = 2$.

The cross-correlation and the autocorrelation side lobe values of the Gold sequences and Kasami (small set) are both 3-valued. The large set of Kasami sequences has autocorrelation side lobe levels equal to those of the small set. However, the cross-correlation values are 5-values. Therefore, we can the define the cross-correlation values of the three different subfamilies as [27] [40],

$$R_{x,y_G}(k) \in \left\{ -1,\ -1 - 2^{(n+l)/2},\ -1 + 2^{(n+l)/2} \right\} \tag{3.4}$$

$$R_{x,y_{K_s}}(k) \in \left\{ -1,\ -1 - 2^{n/2},\ -1 + 2^{n/2} \right\} \tag{3.5}$$

$$R_{x,y_{K_L}}(k) \in \left\{ -1,\ -1 - 2^{(n+2)/2},\ -1 + 2^{(n+2)/2},\ -1 + 2^{n/2},\ -1 + 2^{n/2} \right\} \tag{3.6}$$

where $l = 1$ when the number of shift register is odd and $l = 2$ when the number of shift registers is even.

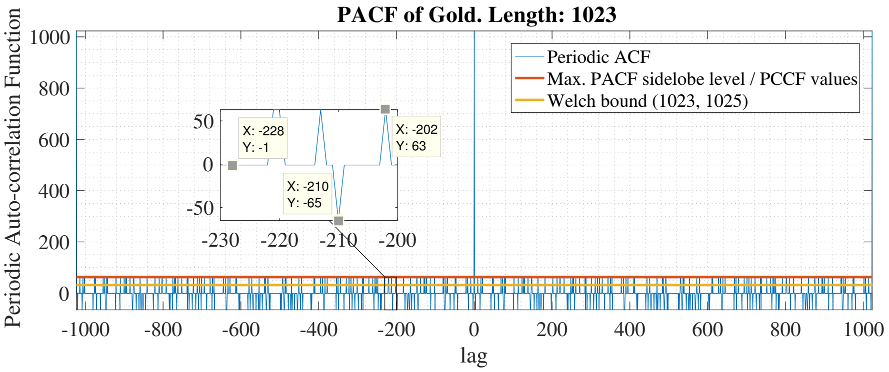

(a) Periodic Autocorrelation Function

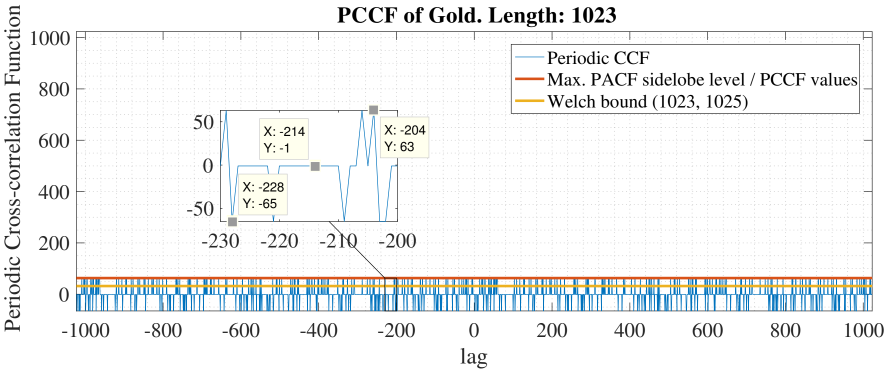

(b) Periodic Cross-correlation Function

Figure 3.3: PACF and PCCF: Gold (1023)

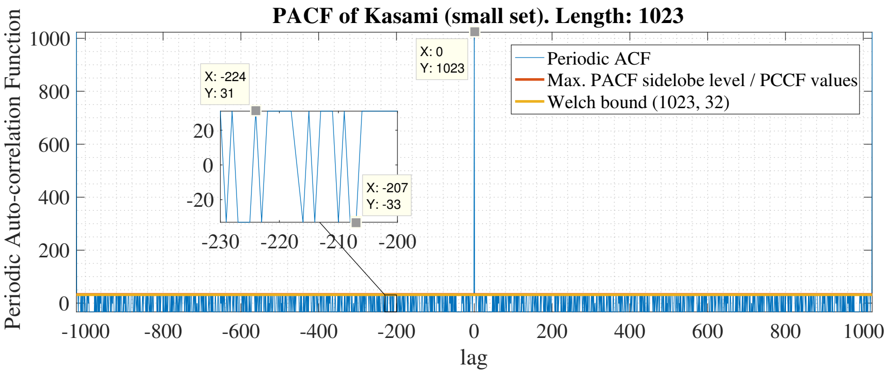

(a) Periodic Autocorrelation Function

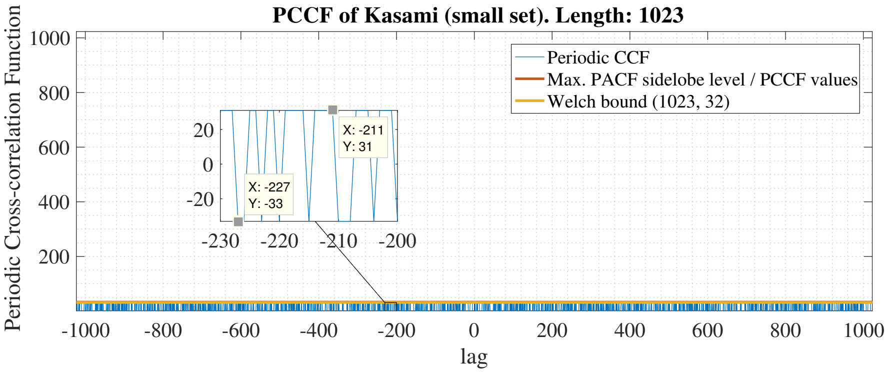

(b) Periodic Cross-correlation Function

Figure 3.4: PACF and PCCF: Kasami small set (1023)

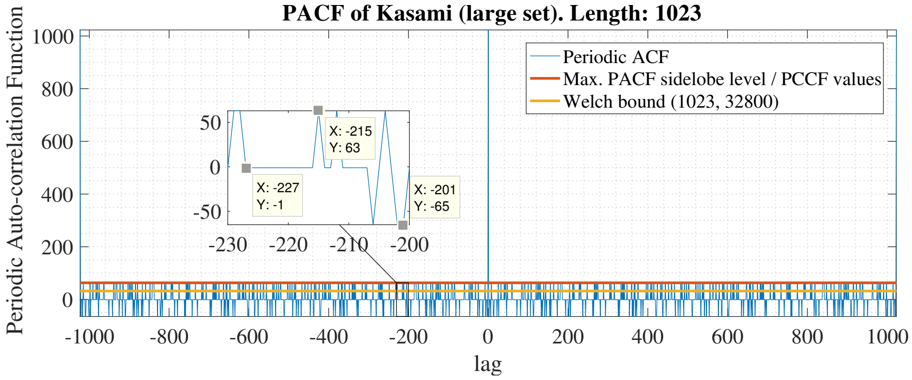

(a) Periodic Autocorrelation Function

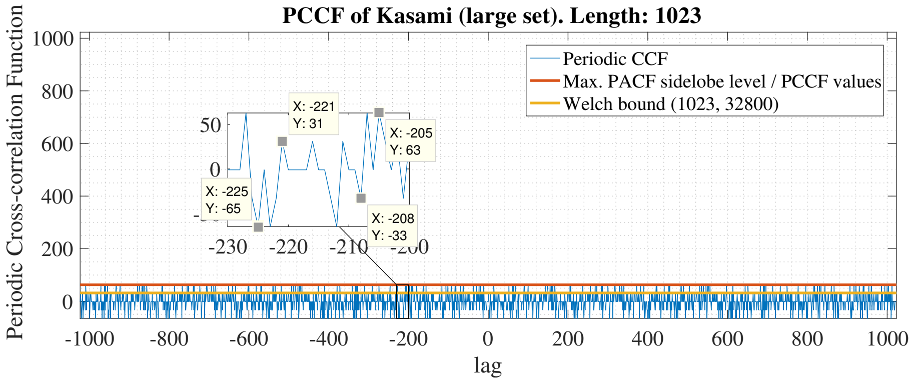

(b) Periodic Cross-correlation Function

Figure 3.5: PACF and PCCF: Kasami large set (1023)

3.1.3 Almost Perfect Autocorrelation Sequences

In 1992, Wolfmann was first to generate a binary sequence whose autocorrelation properties were perfect autocorrelation function except for one lag [41]. He created the sequences up to the size of 100 based on an exhaustive search, which can be found in the appendix of his paper. In [42], Pot and Bradley demonstrate an algorithm that can generate APAS sequences of longer lengths, which is based on p-ary m-sequences. The sequence of interest was deeply analyzed by Van Thillo *et al* in [43], whereas the following properties have been concluded of the L_c-sized APAS sequences:

1. Periodic autocorrelation function has an L_c-amplitude peak for the in-phase value. The out-of-phase values are zero for all non-zero shifts are zero, except for two lags, at $\pm L_c/2$, where two negative peaks are found.

2. The zero-autocorrelation zone is therefore $L_c/2 - 1$.

3. The amplitude of the negative peaks is measured to be $-L_c + 4$.

4. The sequence length must be a multiple of 4. Also, L_c/2-1 must be a prime power e.g. of the form L_c/2-1 = p^r with p prime and r a positive integer.

5. The sequence set size is given by $\mathcal{S}_A = \begin{cases} \frac{\phi(N/4)}{2r}, & \text{if } \bmod\,(N/2-1,\,4)=1 \\ \frac{\phi(N/4)}{r}, & \text{if } \bmod\,(N/2-1,\,4)=3 \end{cases}$, where $\phi(n)$ refers to Euler's totient function [44].

The property of interest of the APAS sequence is that the autocorrelation values are shaped in such a way that the Welch Bound is bypassed for all lags smaller than $L_c/2$. However, the cross-correlation values are large compared to the Welch Bound, for all sequences in the code set $\mathcal{S}_A$. The sequences are therefore not orthogonal to eachother.

The algorithm that was used for the generation of APAS sequences is found in Appendix A.1.

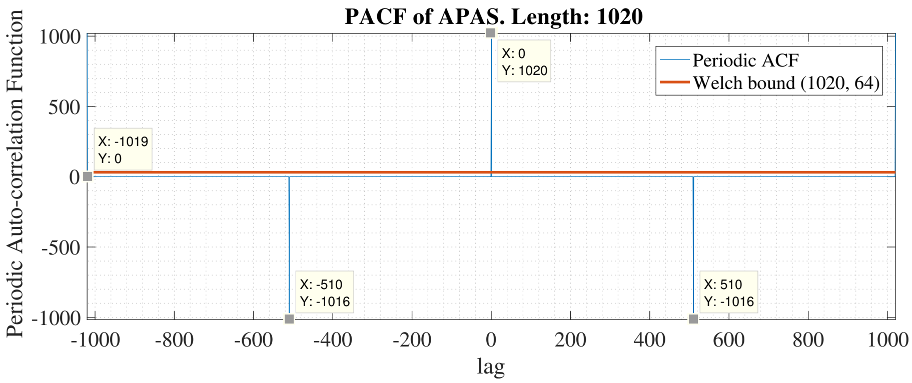

(a) Periodic Autocorrelation Function

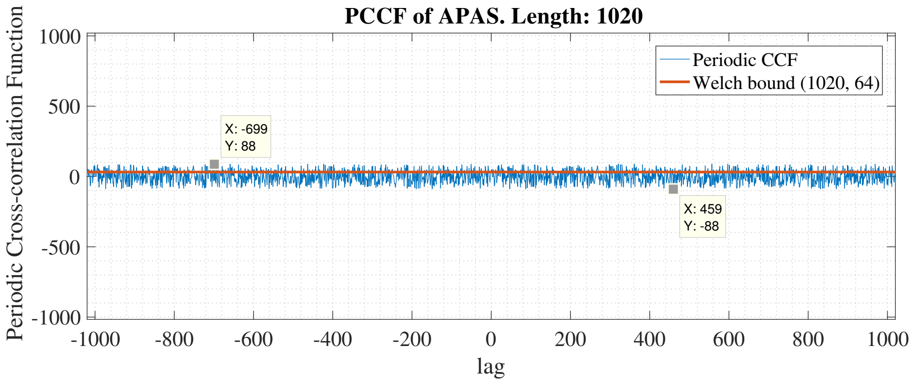

(b) Periodic Cross-correlation Function

Figure 3.6: PACF and PCCF: APAS (1020)

3.1.4 Zero-Correlation Zone Sequences

Zero Correlation Zone (ZCZ) sequences are binary sequences with special correlation properties. For both the PACF and PCCF, the ZCZ sequences are designed such that the PACF/PCCF have zero correlation values in a specified zone (Z_{CZ}). Generally, a ZCZ sequence is defined using a triplet notation (L_c, $\mathcal{S}_Z$, Z_{CZ}), where L_c refers to the code length, $\mathcal{S}_Z$ notes the sequence set size, and Z_{CZ} defined the width of the zero-correlation zone

$$\begin{gathered} Z_{CZ} = \max\{Z : R_{x,y}[k] = 0, \text{ where} \\ (|k| \leq Z \text{ and } x \neq y) \text{ or } (0 < |k| \geq Z \text{ and } x = y))\} \end{gathered} \tag{3.7}$$

The last decades several algorithms have been developed for construction of *optimal* ZCZ sequence set. The random variables in these algorithms are again L_c, $\mathcal{S}_Z$ and Z_{CZ}. Binary ZCZ sequences have been proven by Tang-Fan [30] to be upper bounded by,

$$\mathcal{S}_Z(Z_{CZ} + 1) \leq L_c \tag{3.8}$$

where equality implies optimality. Table 3.1 lists three different algorithms from [36], [45], [46] having a different triplet, which have been implemented. For details on the algorithms, the reader is referred to Appendix A.2.

Table 3.1: Characteristics of three algorithms for generating ZCZ sequences

Algorithm	Triplet $(L_c, \mathcal{S}_Z, Z_{CZ})$	Example	Remarks
[45]	$(2^{2n}L_0, 2^{n+1}, 2^n+1)$	$L_0 = 2, n = 5$; (2048, 64, 33)	-
[36]	$(2^{2n+1}, 2^{n+1}, 2^{n-1}L_0+1)$	$L_0 = 2, n = 5$; (4096, 64, 33)	-
[46]	$(2^{p+2} \cdot n, 2n, 2^p)$	$p = 7, n = p$; (4096,16,128)	Set size and Z_{CZ} can be arbitrary chosen for integers of n and p

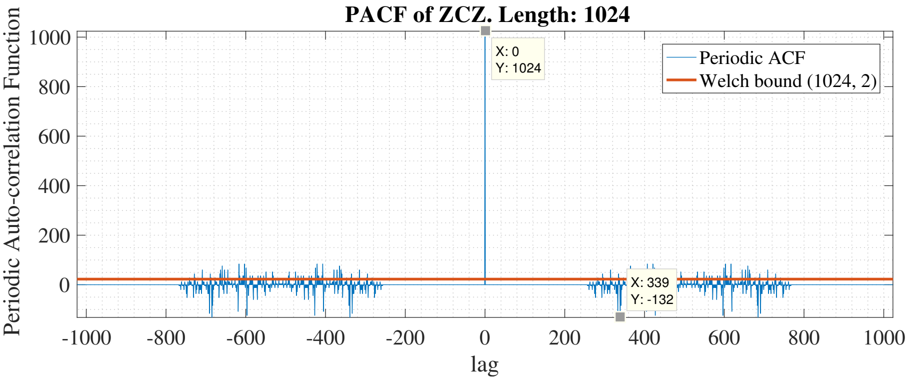

(a) Periodic Autocorrelation Function

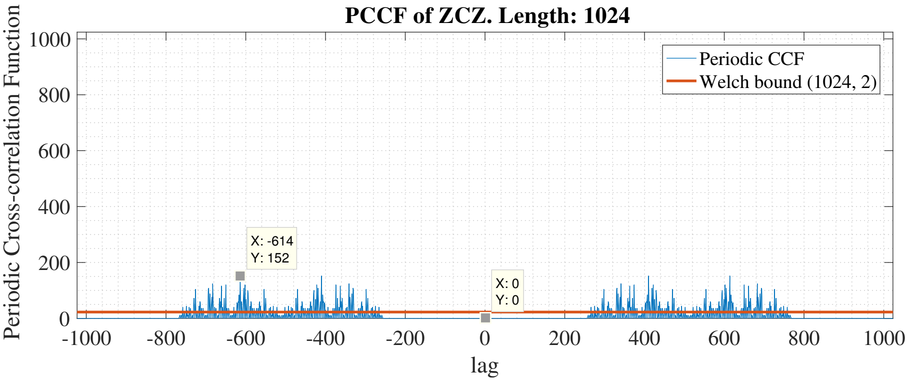

(b) Periodic Cross-correlation Function

Figure 3.7: PACF and PCCF: ZCZ (1024, 2, 256) of [46]

Similar to APAS sequences, the ZCZ sequences also bypass the theoretical limitations defined by the Welch Bound. Only for a specific width, Z_{CZ}, the PACF and the PCCF are inferior to the Welch Bound. This makes these sequences highly attractive to design a radar systems within this predefined zone width.

3.1.5 Summary

The previous section explained the properties and generation of the most likely and available binary codes for automotive radar, of which an overview of its characteristics is given in Table 3.2.

M-sequences have excellent autocorrelation properties whereas its cross-correlation values are relatively large. Only the *preferred m-sequence* have improved cross-correlation values, whose order of magnitude and structure is comparable to those of Gold and Kasami sequences. Preferred m-sequences pairs can be found; however, it is difficult to find a set of *preferred m-sequences* that are preferred pairs to all sequences within the set [47].

Gold sequences, Small set of Kasami sequences and Large set of Kasami sequences are all created using preferred m-sequences and possess similar auto- and cross-correlation properties. The main limitation of the Kasami sequences is the lesser number of code lengths for which they can be generated.

Two code families that possess impressive correlation properties are APAS and ZCZ sequences. Its excellent autocorrelation properties can identify APAS. On the other hand, its cross-correlation properties of the code are poor. However, Bourdoux *et all.* in [3] have provided multiple methods to achieve transmission orthogonality still.

ZCZ sequences are possible codes to provide both perfect auto- and cross-correlation properties within a predetermined zone. The algorithm for the ZCZ of [46] is preferred over the other algorithms stated in Table 3.1. This algorithm provides more flexibility in the sequence set design regarding of code length, set size and zero-correlation zone.

Table 3.2: Properties of different code families and their maximum autocorrelation sidelobe level and/or cross-correlation values, ϕ_m [3], [27], [47], [48]

Code family	**Code length** L_c	**Maximum correlation value** $\lvert\phi_m\rvert$		**Set size** $\mathcal{S}$	
Preferred m-sequence	2^n-1	$1+2^{(n+1)/2}$ $1+2^{(n+2)/2}$	for odd n for even n	Size of connected set of preferred pairs is unknown	
Gold	2^n-1	$1+2^{(n+1)/2}$ $1+2^{(n+2)/2}$	for odd n for mod(n,4)=2	2^n+1	
Kasami (small set)	2^n-1	$1+2^{n/2}$	for even n	$2^{n/2}$	
Kasami (large set)	2^n-1	$1+2^{n/2+1}$	for even n	$2^{3n/2}$ $2^{3n/2}+2^{n/2}$	for mod(n,4)=0 for mod(n,4)=2
APAS	See prop. 4. in APAS	$\phi_a=0$ $\phi_c=$ unknown	for $\lvert k\rvert \leq L_c/2-1$	See prop. 5. in APAS	
ZCZ	Depends on algorithm	0	for $\lvert k\rvert \leq Z_{CZ}$	Depends on algorithm	

The remainder of this thesis explores three different code families: Gold, APAS, and ZCZ sequences. The next section explains the trade-offs in the design of an MRR phase-coded radar for these specific code families.

3.2 Periodic Ambiguity Function

In radar, sacrifices need to be made in terms of maximum detectable range and maximum detectable Doppler as the ambiguities are unavoidable. These aspects have been denoted in Section 3.2, as well as visualized in Figure 2.6.

The focus of this section is to investigate the influence of Doppler on the prior code families within the unambiguous region. This unambiguous region has been retrieved from Figure 2.6 and Equations (2.14) and (2.15). Note that for comparing purposes the arbitrary code lengths are selected to be as close as possible. The total duration of a single frame is equal for all computations in this section, and measures $T_{frame} = 5\,\text{ms}$.

For all Figures 3.8a to 3.8f, there is an apparent peak when the waveform of consideration is non-delayed and non-Doppler shifted, denoted as $|\chi(0,0)|$. This is often referred to as the thumbtack. As expected, the zero-Doppler cut of the PAF, $|\chi(\tau,0)|$, behaves exactly similar to the code's periodic autocorrelation function.

The zero-delay cut, $|\chi(0,f_D)|$, is for all figures precisely the same. The cut shows a sinc-shaped behavior, which is induced by the rectangular structure of the sub-pulses. The first side lobe is found at $-13.46\,\text{dB}$ with respect to the main lobe. Remarkably, for certain delays, the visible range sidelobes also degrade in a sinc-pattern for Doppler shifts.

However, an essential remark that must be taken into the design stage, is the fact that the matched filter output responds fully accords to its theoretical autocorrelation function. There are no surprising peaks or side lobes for specific pairs of delay and Doppler.

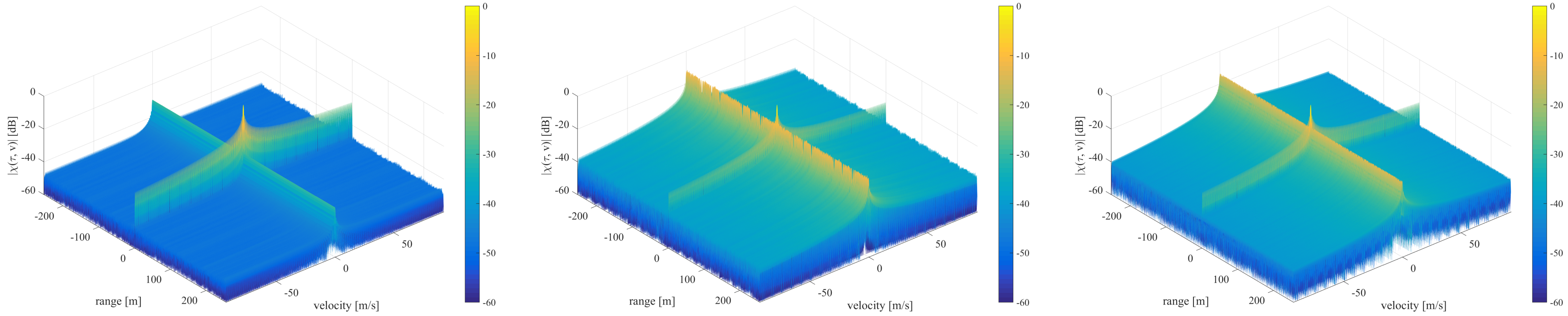

(a) M-sequence(1023): $M = 1466$.

(b) Gold(1023): $M = 1466$.

(c) Kasami small set(1023): $M = 1466$.

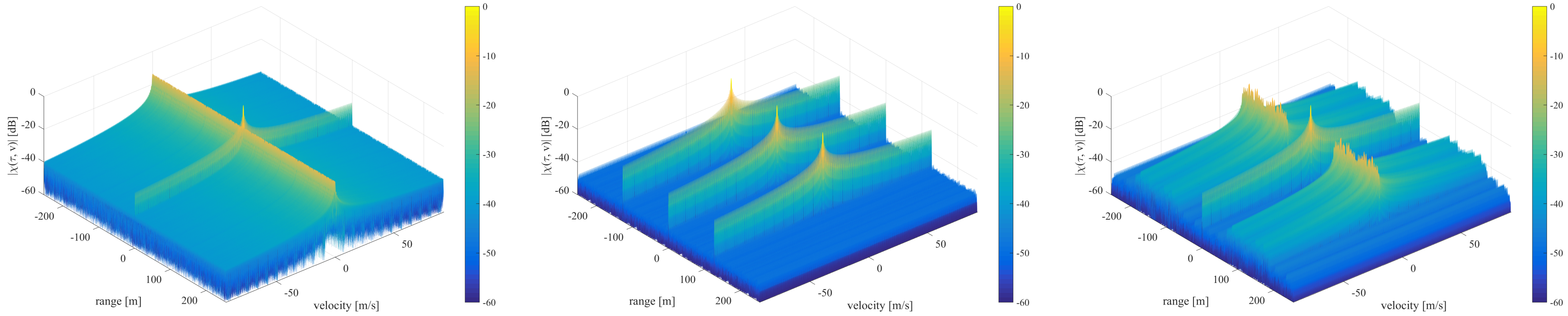

(d) Kasami large set(1023): $M = 1466$.

(e) APAS(1020): $M = 1470$.

(f) ZCZ(1024): $M = 1464$.

Figure 3.8: Periodic Ambiguity Function

3.3 MIMO System Design

Phase-coded radar might provide the solution to take full advantage of the capacity of the transmit array containing K_T transmitters. However, this requires at least K_T waveforms that are orthogonal by coding. If K_T orthogonal codes are available, the K_T transmit antennas can transmit concurrently, as each antenna transmits its own unique coded waveform. Therefore, the number of transmitters should always be smaller or equal to the set size of the code family being utilized: $K_T < \mathcal{S}$. On the other hand, non-orthogonal codes act as interferers, for which sidelobe levels behave according to its cross-correlation properties.

Concerning MIMO system design, radar engineers always question themselves how to transmit the waveforms concurrently and exploit the desired correlation properties of a distinct waveform. Like already mentioned before, this thesis focusses on full-transmit capacity. For this thesis, two transmission methods are selected and explained in the subsection below. Subsequently, design for each code family is explicitly given.

3.3.1 Transmission Schemes

Code Division Multiplexing

The first transmission scheme, a trivial solution for PMCW waveforms, is code division multiplexing (CDM). In this configuration, all transmitters start radiating simultaneously, where every antenna transmits its own unique coded waveform as illustrated in Figure 3.10. This transmission scheme will be used for the Gold sequence and the ZCZ sequence.

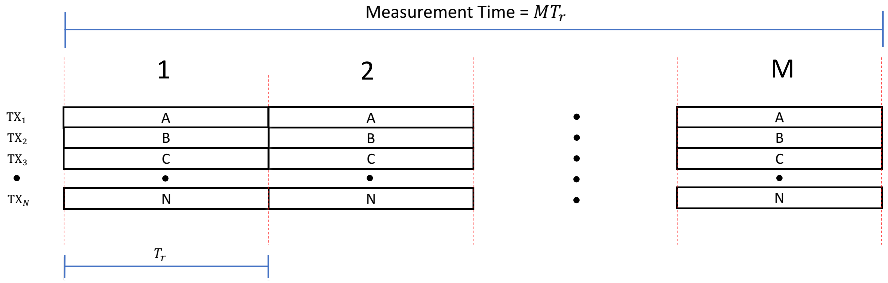

Figure 3.9: Time Division Multiplexing (TDM)

Time Division Multiplexing

Another technique being discussed is a transmission scheme proposed by Bourdoux [3] where an APAS sequence is time-staggered for K_T transmitters, called Time Division Multiplexing (TDM). This technique benefits from the perfect autocorrelation properties as only one unique APAS sequence is transmitted by all transmit antennas. Each antenna in the array starts transmitting at a different time instant, resulting in the time-staggered profile illustrated in Figure 3.9.

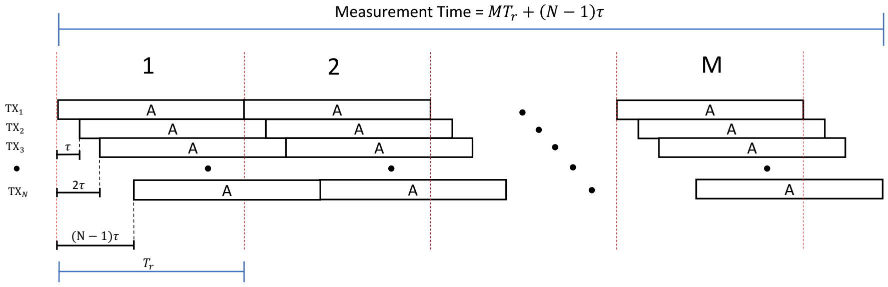

Figure 3.10: Code Division Multiplexing (CDM)

3.3.2 System Parameterization

NXP Semiconductors set the following requirements for the design of an MRR MIMO PMCW radar:

1. The radar must be equipped with 16 transmitting antennas;
2. The radar must at least satisfy the range/velocity resolution and maximum ambiguous range/velocity as defined in Table 1.1.
3. The maximum number of FFT outputs is limited to 2048.

Table 3.3 lists the final design parameters for the Gold, ZCZ and APAS sequence, which will be substantiated below.

Gold Sequence

The MIMO radar employed with the Gold sequence uses the CDM transmission scheme. The autocorrelation side lobes and cross-correlation values are equally significant, meaning that none of the two can be emphasized in a particular transmission scheme.
For the implementation of the Gold sequence in the MIMO radar, we start off by selecting an appropriate code length L_c that concurrently satisfies the maximum ambiguous range of (2.14) and maximum ambiguous velocity of (2.15). From (2.16), we have seen that this resulted in a lower and upper bound for L_c

$$151 < L_{c,siso} < 4744\,.$$

Generating sequence sets for certain code families could bring along several implications. For the Gold sequence, this implication is the code length, which depends on the code length for which preferred m-sequence can be generated. The number of registers, n, in the LFSR can not be mod(n,4)=0. Therefore, lengths $L_c = 255$ and 4096 are excluded, which leaves over lengths $L_c = 511, 1023$ and 2047 in the range of (2.16).

Regarding velocity estimation, the code lengths mentioned above also suffice the maximum ambiguous velocity. To limit the number of slow-time periods, the most prodigious length of the three code lengths is chosen, which is $L_{c,mimo-G} = 2047$. For $T_c = 3.33\,\text{ns}$, this means that the duration of a single slow-time period lasts for 6.68 µs. The maximum velocity for the Gold sequence measures

$$v_{max} = \pm \frac{\lambda}{4\,L_{c,mimo-G}\,T_c} = 139.04\,\text{m/s}\,. \tag{3.9}$$

Then, to achieve a velocity resolution of $\Delta v_r = 0.2\,\text{m/s}$, hence $T_{frame} \approx 10\,\text{m/s}$, the number of slow-time repetitions is equal 1465. Therefore, the number of FFT points could be set to the next power of 2, which is $N_{FFT} = 2048$.

The sequence set size $\mathcal{S}_G$ does not bring any implications for assigning each transmit antenna an unique code, since $\mathcal{S}_G = 2048$.

ZCZ Sequence

As mentioned before, the ZCZ sequence possesses beneficial properties for the design of the MIMO radar. Like the Gold sequences, its transmit mode is CDM, where it is designed such that the zero-correlation zones are larger than the maximum required distance.

In [46] and Table 3.1, it is stated that the width of the zone for zero-correlation is confined to a power of 2. Therefore, for the zone Z_{CZ} to be larger than 151 range gates of (2.16), it is required to have $Z_{CZ} = 2^p = 256$, and thus $p = 8$. The number of transmitters is fixed to $K_T = 2n = 16$, hence $n = 8$. This finalizes the triplet

$$(L_{c,mimo-Z}, \mathcal{S}_Z, Z_{CZ}) = (2^{p+2}n, 2n, 2^p) = (8196, 16, 256)\,,$$

hence $L_{c,mimo-Z} = 8196$. However, such a large code length limits the maximum detectable velocity to $v_{max} = 34.74\,\text{m/s}$, which is insufficient for the application.

Unfortunately, this setup requires us to scale down on either K_T or Z_{CZ}. For this design, we have chosen to keep the number of transmitters intact and reduce the zero-correlation zone to 128, which leads to the final triplet (4096, 16, 128). The maximum detectable velocity is enhanced by a factor 2, compared to the former case, and measures:

$$v_u = \frac{\lambda}{4\, L_{c,mimo-Z}\, T_c} = 69.49\,\text{m/s}\,. \tag{3.10}$$

The consequence of limiting the width of the correlation zone implies degradation of performance of the radar. However, the severeness of performance deterioration depends on the reflectivity of a target and the location of a target. Since for an MRR radar with $\Delta R = 0.5\,\text{m}$ the zero-correlation zone is equivalent to $Z_{CZ} = 64\,\text{m}$, targets close ($R < 11\,\text{m}$) to the radar and farther away ($R > 64\,\text{m}$) can have a direct impact on the correlation within the range of interest.

A first situation is sketched using a truck having a significant RCS and is closely positioned to the radar, as depicted in Figure 3.11a. In this case, it means that after $R = 68\,\text{m}$, for which the autocorrelation artifacts as well as the cross-correlation artifacts are summed to form side lobes.

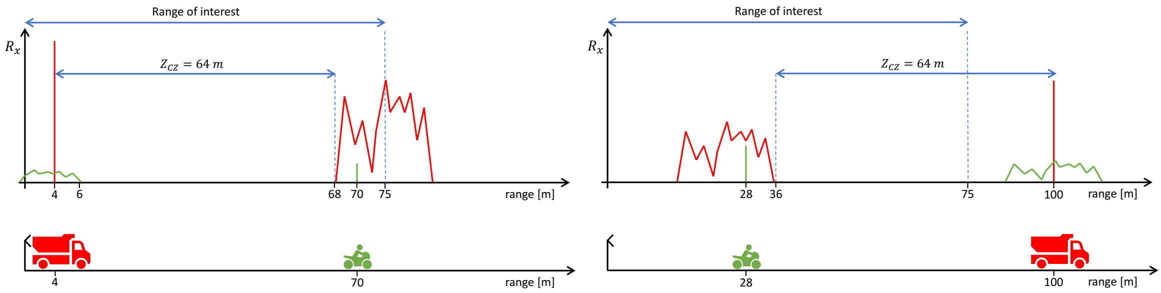

(a) Strong interferer within range of interest **(b)** Strong interferer outside range of interest

Figure 3.11: Insufficient width of the correlation zone in ZCZ sequences

A similar situation could occur, where the target is outside the range of interest, but still causes problems within the range of interest. This is exemplified in Figure 3.11b. Nonetheless, note that these reflections are usually largely suppressed due to path attenuation.

APAS Sequence

This MIMO design for APAS sequences exploits the almost perfect autocorrelation properties, and obscures its poor cross-correlation properties. Namely, by time staggering a single sequence as was explained above, which is known as TDM transmission scheme, as explained above.

Once again, the secondary peak of the autocorrelation function of the APAS addresses the maximum distance. APAS sequences can be generated for numerous of lengths, which makes the design process flexible. If $K_T = 16$ is selected, the minimum code length in order to satisfy the unambiguous range

$$L_{c,min_{mimo}} = 16 \cdot 2 \cdot L_{c,min_{siso}} = 4832 \tag{3.11}$$

where the factor 2 places the ambiguous secondary peak twice as far. This code length already exceeds the upper limit defined by (2.16), which means that both R_u and v_{max} cannot be satisfied.

Unlike the MIMO design of the Gold and ZCZ sequences, the nearest code length to 4832 could lead to ambiguous objects among the transmitters. For example, this would mean that the range corresponding to round trip delay, τ_{rt}, is approximately 75 m. In this design the delay, τ_a, among the transmit elements is slightly increased, such that the range corresponding measures 85 m. Therefore, by increasing the code length a guard time band is implemented to ensure unambiguity for 10 m additional meters. Thus, the closest code length for the APAS sequence is $L_{c,mimo-A} = 5160$, and hence the delay across the consecutive antenna elements is equivalent to

$$\tau = \frac{L_{c,mimo-A}\, T_c}{2K_T} \tag{3.12}$$

The code length results in a maximum detectable velocity equal to

$$v_u = \frac{\lambda}{4\, L_{c,mimo-A}\, T_c} = 55.16\ m/s \tag{3.13}$$

To understand the principles of reception of the time-staggered APAS-coded waveforms, a simplified example is given for $K_T = 4$ and $L_c = 1296$. In Figure 3.12, the return signal gives rise to a time staggered correlator's output having a period of $L_c/(2K_T)$ lags. In this example, a stationary target is located at $R = 20$ m, or in range gate 40. The first antenna starts transmitting at lag = 0; the second antenna starts at the first red line lag = 161; the third one at lag = 322; and so forth. The last $L_c/2$ correlation lags of the output of the correlator (after the rightmost red line) represent the secondary peaks of respectively TX(1) to TX(4). These outputs are left out from further processing.

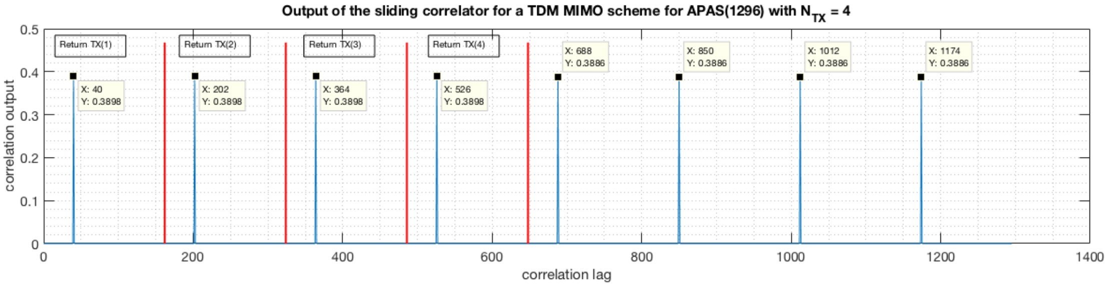

Figure 3.12: Time Division Multiplexing (TDM) for APAS(1296) with $K_T = 4$.

Table 3.3: MRR MIMO System Parameters

Parameter	Symbol	Values					
		Gold		**ZCZ**		**APAS**	
Number of Transmitters	K_{T}	16		16		16	
Number of Receivers	K_{R}	1		1		1	
Code length	L_c	2047		4096		5184	
Chip duration	T_{c}	0.33	ns	0.33	ns	0.33	ns
Duration of period	T_{r}	6.82	µs	13.65	µs	17.28	µs
Number of periods	M	1465		732		578	
Number of FFT points in Doppler processing	N_{FFT}	2048		1024		1024	
Total duration of a singlr transmit frame	T_{frame}	9.996	ms	9.99	ms	10.00	ms
Range resolution	ΔR	0.5	m	0.5	m	0.5	m
Maximum distance	R_u	1022.8	m	2046.6	m	81.0	m
Maximum zero-correlation distance	R_{cz}	-		64	m	81.0	m
Velocity resolution	Δv	0.19	m/s	0.19	m/s	0.19	m/s
Maximum velocity	v_u	139.0	m/s	69.49	m/s	55.15	m/s

3.4 Conclusion

This chapter examined the possible binary code families applicable in automotive radar in terms of autocorrelation and cross-correlation properties and sequence set sizes.

The autocorrelation properties returned in the thumbtack-shaped ambiguity function, with Doppler sidelobes according to a sinc-pattern.

This chapter concluded with a specific MIMO design for the Gold, ZCZ and APAS sequences. Table 3.3 presents the important parameters for the design of the three former code families. The design of the codes has been plagued by trade-offs that had to be taken in terms of maximum detectable range, maximum detectable velocity, sequence set size, zero-correlation zone widths. Therefpre, it has been shown that the designs cannot be optimized, and the system design needs to give in in at least one property:

1. For the Gold sequence, radar performance is reduced in terms of autocorrelation sidelobes and cross-correlation values.

2. Zero-correlation sequences have zero correlation values; however, they can not be realized for all range gates if a large number of channel accesses is required (16TX). By alleviating the restriction on the number of transmit antennas, and taking, e.g., $K_T = 8$ would highly increase the performance of the ZCZ-coded waveform.

3. The APAS sequences must be designed such that the maximum detectable velocity is inferior to the requirements. Also, ambiguous targets could arise more easily than for the former two designs.

Chapter 4

Synchronous Interference

In the chapter that follows, it will be investigated how the three preferred code families, namely Gold, APAS, and ZCZ sequences, perform concerning synchronous interference. Synchronous interference is inevitable for MISO or MIMO configurations. Section 4.1 briefly introduces the phenomena and denotes the main definitions required to inspect synchronous interference. Next, Section 4.2 and 4.3 explain implications caused in MIMO system designs by, e.g. low pass filter, significant TX-to-RX spillover, reflections from moving targets. Finally, a comparison is given on the computational requirements of the three distinct MIMO system designs.

4.1 Definitions

This chapter focusses only on MISO configurations to entirely investigate the effect of multiple (semi-orthogonal) coded waveforms returning simultaneously at a single receive antenna. Synchronous interference connotes as unwanted electromagnetic radiation occurring in Code Division Multiplexing. The mutually interfering signals are referred to as synchronous, meaning that the signals fully overlap in time and possess similar center frequency f_c, bandwidth (and hence chip width), code family and code length.

Mutually interfering signals can have several effects on the performance of the radar. To get a better understanding of how certain aspects influence interference levels, we are defining three important metrics. First of all, *noise floor* is defined as the average noise power in the Range-Doppler plot

$$N_F = \frac{1}{R_G - N_T} \sum_{i}^{R_G} \mathbf{y}_i \mathbf{y}_i^H, \quad \text{where } i \neq T_j \text{ and } j = 1, 2, ..., N_T \tag{4.1}$$

where R_G is the total number of range gates of the RD-map, $\mathbf{y}_i$ refers to the i-th range gate in the Range-Doppler Map, N_T is the number of targets located within the RD-map, and T_j is the specific range gate in which target j is located. Thus, all Doppler bins within a target's range bin are excluded from the calculation of the noise floor. This method only works in the deterministic case, e.g., when the target's range bin is known beforehand.

Another definition that generally goes in hand with the noise floor is receiver sensitivity. Receiver sensitivity determines the ability of the radar to pick up weak signals. In general, loss in receiver sensitivity is then referred to the increase in noise floor with respect to the theoretical noise floor. If there is a loss in receiver sensitivity, due to imperfections in auto- and cross-correlation, or interference, targets will become more challenging to detect.

Then we will define the Peak-to-Sidelobe Ratio (PSR) as the ratio of the main lobe power level to the second largest power level within a particular range/Doppler gate.

4.2 Autocorrelation Performance

The performance of phase-coded radar is heavily depending on the autocorrelation properties of the code being implemented. In practice, some undesirable effects may arise due to intrinsic or extrinsic realities.

4.2.1 Impact of Low Pass Filter

Besides suppressing the sidelobes in the frequency spectrum, the low pass filtering in the digital domain establishes the additional functionality of suppressing out-of-band interference. Removing frequency components by filtering also brings some side effects on the autocorrelation performance of the phase-coded waveforms. Figures 4.1a and 4.1c show multiple spectra with distinct cut-off frequencies, f_{cut}, when applying a Brickwall filter and 4th order Chebyshev low-pass filter in the receiver chain.

Brickwall filter, also known as Sinc filter, completely suppresses the sidelobes of its frequency spectra. The filter's impulse response in time is equivalent to the sinc function, while it is a rectangular function in the frequency domain. Figures 4.1a-4.1d consider the following cut-off frequencies: $f_{cut} = \pi/4\,R_c$, R_c, $2R_c$ and ∞. The cut-off frequency $f_{cut} = \pi/4\,R_c$ was selected, since Guermandi *et al.* state in [49] that the SNR is maximized for this proposed cut-off frequency. The other cut-off frequencies are equal to, or multiples of, the first null in the frequency spectra.

As previously defined in Section 2.2, the RF receiver bandwidth of $B_N = 2R_c$ seems to satisfy the correlation properties well enough.

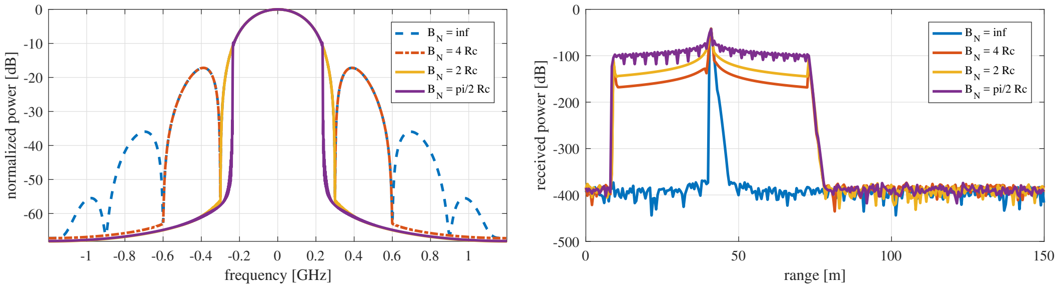

(a) Power Spectra using Brickwall LPF

(b) Autocorrelation using Brickwall LPF

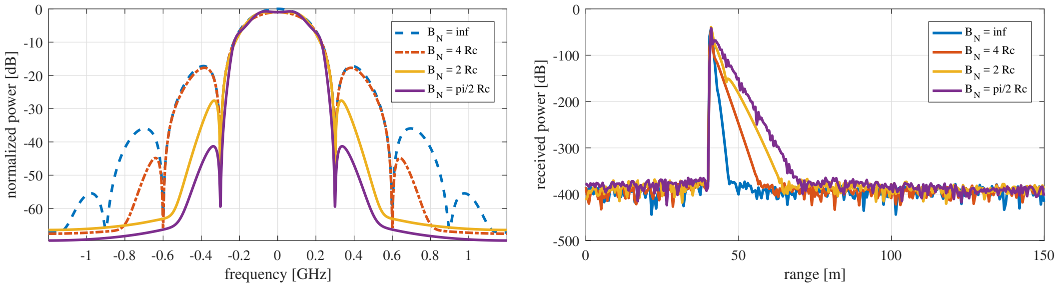

(c) Power Spectra using 4th-order Chebyshev LPF

(d) Aurocorrelation using 4th-order Chebyshev LPF

Figure 4.1: Low-pass filter effects

Actually, the more high-frequency components are lost, the higher the sidelobes in range due to imperfect autocorrelation process, as depicted in 4.1b. As we have seen in the theoretical study, the sidelobes for the APAS and ZCZ sequences are supposed to be zero, and minus infinity in dB scale. In the noiseless case, the sidelobes are found at approximately -400 dBm for a return signal that does not undergo low-pass filtering. These values of the pretended "noise floor" are approach the limit of the double floating point precision, and is, therefore, a constraint of the simulation environment MATLAB.

Theoretically, the side lobe levels are found at minus infinity due to the zero-correlation values, but MATLAB limits the values to the double-precision floating point precision.

For the brickwall filter, a symmetrical pattern in sidelobe levels of significant magnitudes is found for approximately 30 adjacent range gates (see Figure 4.1b).

The 4^{th}-order Chebyshev low pass filter better preserves the perfect autocorrelation properties, as the width of the peak slightly increases for increasing RF receiver bandwidth. The higher-order frequency components signify the smoothness of the received and filtered, and its close relation to the correlation properties.

4.2.2 Spill-over effect

Car integration and assembly of the radar-on-chip is another critical aspect. First of all, it is aims to protect the radar from dust and dirt. However, the radome should be carefully designed to avoid system degradation due to transmission losses, reflections, and edge effects. The radars are usually mounted behind the front and rear bumpers, which can also vary in thickness and shape. Bloecher *et al.* performed a series of experiments to show the electromagnetic effects of bulk material and painting, manufacturing tolerances, various paintings and coverage of water, snow, ice, dust, salt, etc. [50]. They experimented with a bumper with a substrate thickness $d = 3.44\,\text{mm}$ and found a maximum reflection coefficient of $-20\,\text{dB}$, which we will from now on as an assumption for simulating the spill-over effect. Here, we assume that the radome is dry, as a water-covered dielectric radome can heavily increase the reflection coefficient. For a study on the influences of rainwater, the interested reader is referred to the work of N. Chen *et al.* in [51].

In the following example a single target with $\sigma = 10\,\text{dBm}^2$ is located at 20 m. Then, as every transmitting antenna radiates with $P_T = 10\,\text{dBm}$, with $G_T = 10\,\text{dB}$ and $\Gamma = -20\,\text{dB}$, the received signal power from the spill-over effect is $P_{Spill} = 0\,\text{dBm}$. Then, for a processing gain $G_p = 64.77\,\text{dB}$, the correlated output power from the strong reflections can have undesirable effects on the Range-Doppler plots for codes that have non-zero autocorrelation sidelobe levels.

Gold Sequence Gold sequences are characterized by its non-zero auto/cross-correlation sidelobe levels, that for $L_c = 2047$ has a theoretical peak-to-sidelobe in the target's range cut. For $N_T = 16$ transmitter antennas, the autocorrelation values are added to the non-zero cross-correlation values which are accumulated for (N_T - 1) channel accesses and could be denoted as

$$\mathbf{y}_1 = \sum_{k=1}^{N_T} \mathbf{r}_{1k}\,. \tag{4.2}$$

where $\mathbf{r}_{11}$ refers to autocorrelation, and $\mathbf{r}_{1k}$ for $k \neq 1$ refers to the cross-correlation.

The range-Doppler map that includes the effects of the high spill-over reflections is visualized in Figure 4.2a. The peak power in the range profiles in the target's range gate measures 36.48 dBm. The target at $R = 20\,\text{m}$ is covered under these extremely large received powers. By comparing this Figure to the ambiguity function of Figure 3.8b, we observe that the sinc-shaped sidelobes in Doppler caused by the significant ridge are suppressed by applying a Dolph-Chebyshev window over the slow-time samples before taking the Doppler FFT. The window ensures that moving targets with velocities $|v| > 0.2\,\text{m/s}$ do not fall below the main lobe and sidelobes of the high spill-over power. However, still, we observe an artificial increase in noise floor that is caused by the sidelobe levels of the Dolph-Chebyshev window.

$$S_L = N_F - P_N = -50.76\,\text{dBm} - (-76.76\,\text{dBm}) = 26.00\,\text{dB} \tag{4.3}$$

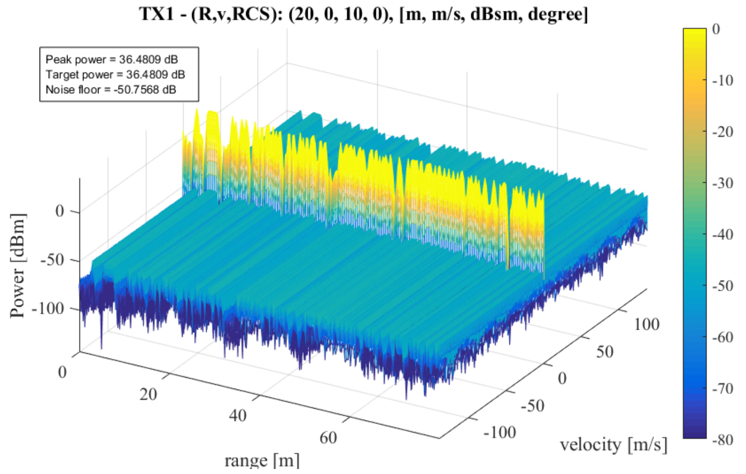

(a) Range-Doppler plot

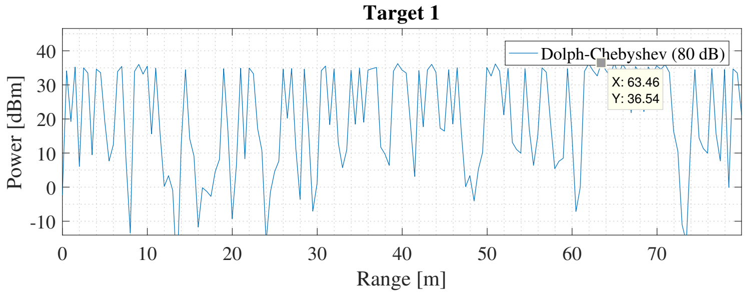

(b) Range cut at Target Velocity and Azimuth

Figure 4.2: Spill-over effect: Gold (2047)

APAS and ZCZ Sequence In contrast to the Gold sequence, the APAS and ZCZ sequences are known for they perfect correlation values within the specified ranges as defined in Section 3.3.2. As expected, the spill-over effect does not lead to extreme performance degradation. Only for $R < 2.5\,\text{m}$, the spill-over reflections cause a huge peak in the first range bin and some spectral leakage in the four adjacent range bins. Also, the Dolph-Chebyshev window fixes the Doppler sidelobe levels at $-80\,\text{dB}$ with respect to the peak power of the spill-over reflection. Since the PACF sidelobe levels and the PCCF values fall below the average noise floor in the presence of Additive White Gaussian Noise. Respectively, Figures 4.3a and 4.4a illustrate the Range-Doppler plots of APAS and ZCZ sequence and show the static target is well defined at $R = 20\,\text{m}$ with processed power levels of 28.68 dBm and 28.66 dBm.

Additionally, it has been addressed that the zero-correlation zone is limited to 64 m (see Table 3.3). Thus, the spill-over effects create large artifacts for $R > 64\,\text{m}$ within the zero Doppler bin. This shows once again that the zero-correlation zone cannot be realized for 16 unique sequences for 16TX MIMO.

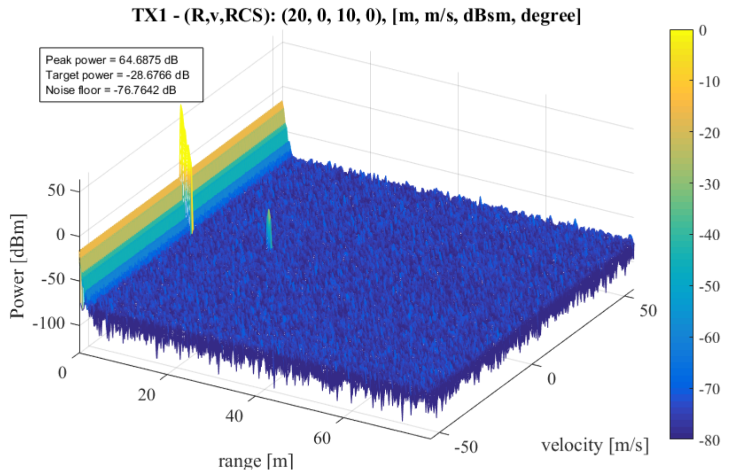

(a) Range-Doppler plot

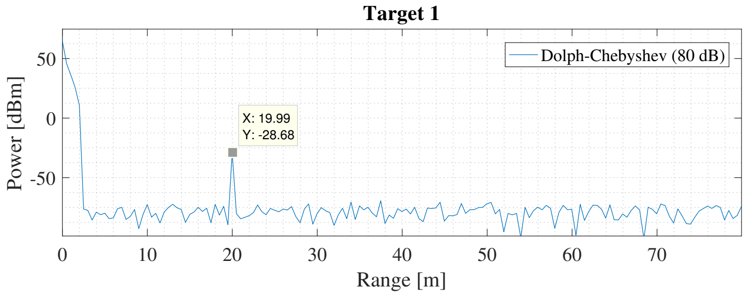

(b) Range cut at Target Velocity and Azimuth

Figure 4.3: Spill-over effect: APAS (5184)

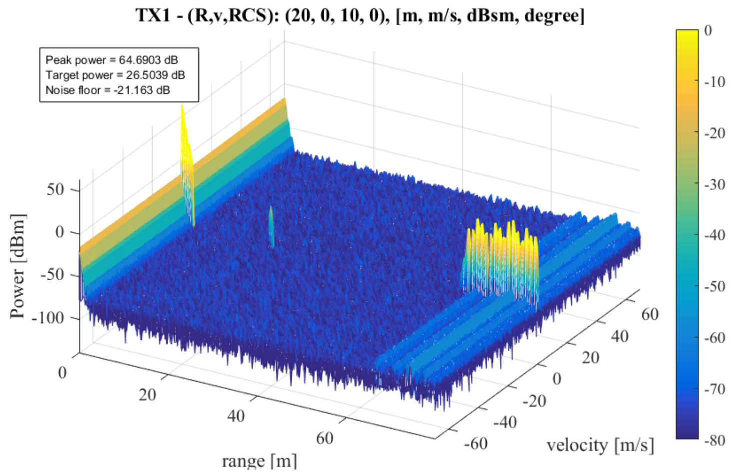

(a) Range-Doppler plot

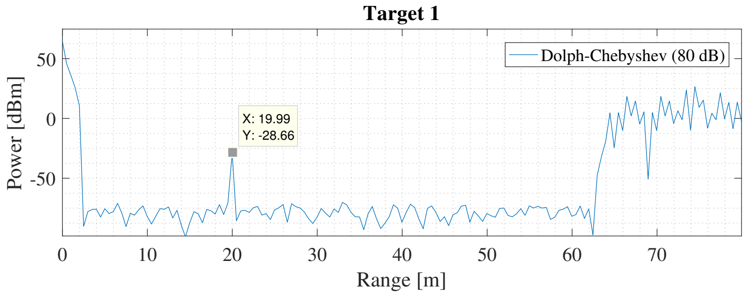

(b) Range cut at Target Velocity and Azimuth

Figure 4.4: Spill-over effect: ZCZ (4096)

4.3 Orthogonality

Besides degradation of the autocorrelation characteristics of the code caused by the low pass filter, orthogonality can also become problematic, e.g., when reflections from moving targets arrive at the radar.

4.3.1 Doppler Tolerance

Doppler tolerance of phase-coded waveforms has always been a point of discussion. This section reviews whether these statements should be taken into notice for the predefined systems. The impact of Doppler shifts is observed in the radar's performance in the range-Doppler map and range-angular map.

Velocity Spectrum

In the range-Doppler map, we ran Monte-Carlo simulations of 100 repetitions for the proposed designs of the three code families for 16TX channels that solely consists of a single target. By varying this target's velocity from $0\,\mathrm{m/s}$ to $80\,\mathrm{m/s}$, we could observe the performance of the distinct code families that are influenced by the presence of Doppler shifts. Figures 4.6 to 4.7 show the Range-Doppler maps for target velocity of $v = 0\,\mathrm{m/s}$ and $v = 40\,\mathrm{m/s}$ for respectively Gold, APAS and ZCZ sequences. For $v = 40\,\mathrm{m/s}$, there start to appear high range sidelobes in the target's range cut.

In Figure 4.5a the target's peak power is plotted against target velocity. This figure illustrates the phenomenon that a Doppler shift causes the peak power to degrade due to non-idealities in autocorrelation. This effect is augmented as the length of the sequence increments. Therefore, the APAS sequence of length $L_c = 5184$ is roughly $10\,\mathrm{dB}$ less prominent than in the case of a stationary target reflection.

Contrarily, the peak-to-sidelobe ratio in a target range cut does not depend on the code length (see Figure 4.5b). The APAS sequence exhibits the best performance of the three code families regarding PSR, which means that for this specific code family the ratio of the peak amplitude to the highest Doppler-induces sidelobe is larger.

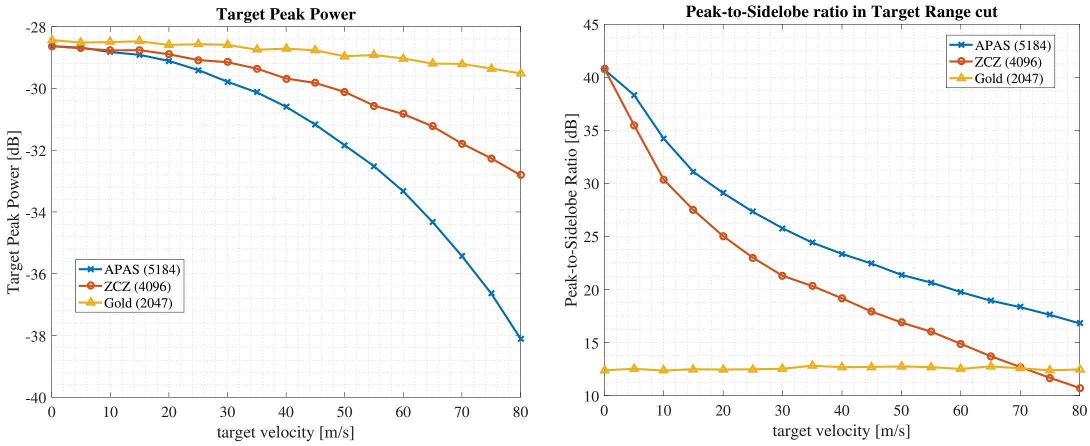

(a) Target Peak Power

(b) Peak-to-Sidelobe ratio

Figure 4.5: Doppler Tolerance in Range-Doppler Map

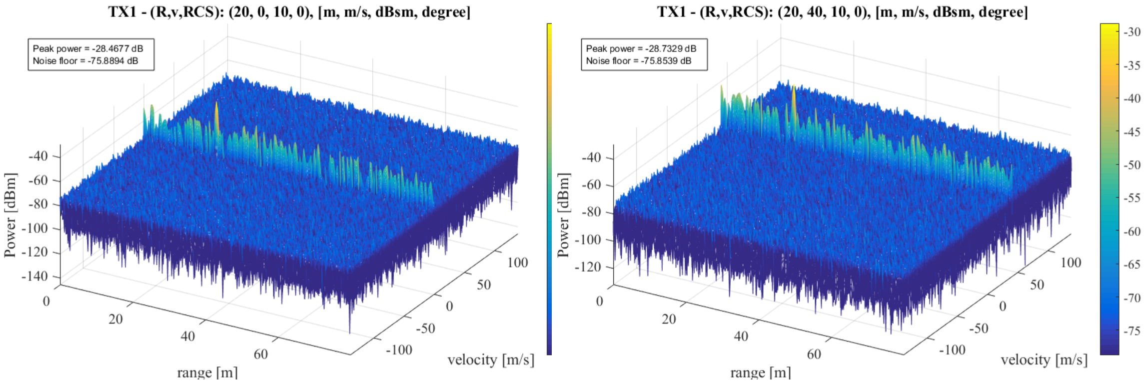

(a) $v = 0\,\mathrm{m/s}$ **(b)** $v = 40\,\mathrm{m/s}$

Figure 4.6: Range-Doppler Map: Gold (2047).

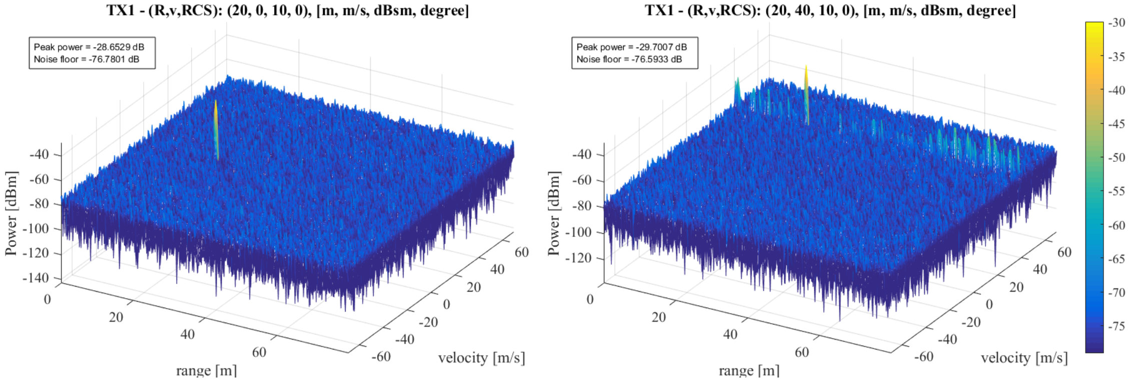

(a) $v = 0\,\mathrm{m/s}$ **(b)** $v = 40\,\mathrm{m/s}$

Figure 4.7: Range-Doppler Map: ZCZ (4096).

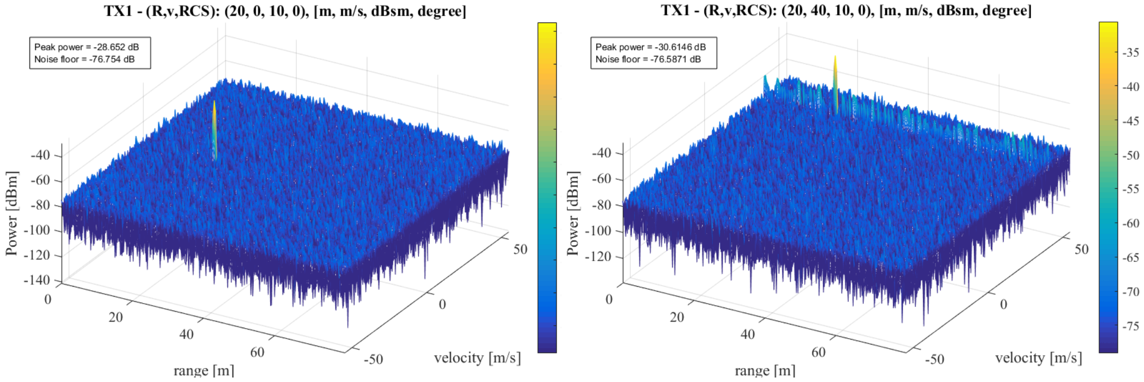

(a) $v = 0\,\mathrm{m/s}$ **(b)** $v = 40\,\mathrm{m/s}$

Figure 4.8: Range-Doppler Map: APAS (5184).

Angular Spectrum

The importance of robust angle estimation is highly needed to bring maturity to automotive radar. Although more robust algorithms exist, this thesis uses an FFT over the spatial samples to estimate the angle of arrival (read Section 2.5.1). This section entails the consequences of Doppler on this angle estimation method. Like the previous section, range-angular maps have been illustrated in Figures 4.11 to 4.12 for respectively the Gold, APAS and ZCZ sequence for $v = 0\,\mathrm{m/s}$ and $v = 40\,\mathrm{m/s}$.

In the Range-Angular map, the peak-to-sidelobe ratio in range for the target's angle degrades more rapidly than the peak-to-sidelobe ratio in the Range-Doppler map.

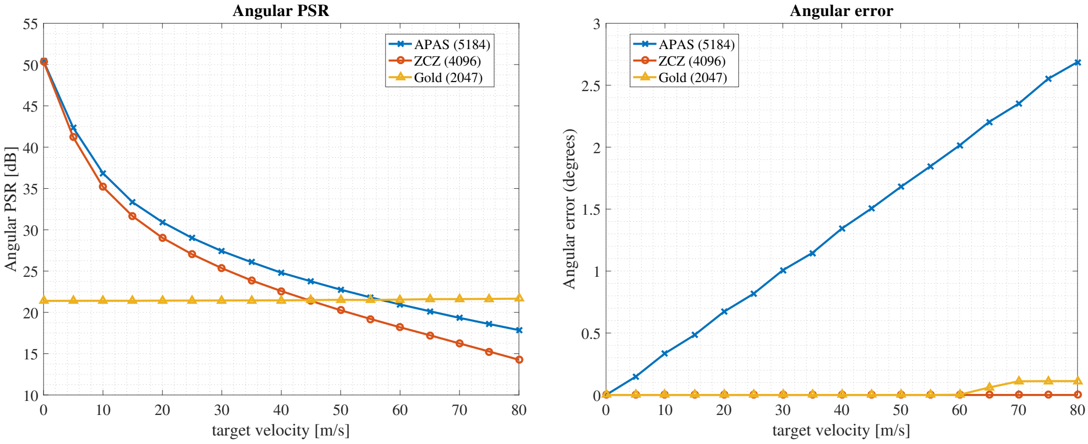

(a) Peak-to-Sidelobe ratio **(b)** Estimated error in DoA

Figure 4.9: Doppler Tolerance in Range-Angular Map

Similar to its performance in the Range-Doppler map, the Gold code of length $L_c = 2047$ is somewhat Doppler resistant. As the code's high natural sidelobe characteristics remain similar for target velocities up to $v = 80\,\mathrm{m/s}$, its performance in angle estimation is constant. However, as Figure 4.11 shows a very noisy-like angular spectrum.

APAS and ZCZ sequences can accurately reconstruct a stationary target's angular position. Artifacts start to show up as reflections from a non-stationary target are received. The peaks are visible, but phase distortion caused by Doppler shifts results in inaccuracy in auxiliary ranges and angles. For the ZCZ sequence, Figure 4.12b depicts especially distortions in ranges farther than the target at $R = 20\,\mathrm{m}$. Also, the artifacts are only found for angles at which the main lobe or sidelobes of the target are located, where the uneven sidelobes have fewer distortions compared to the even sidelobes.

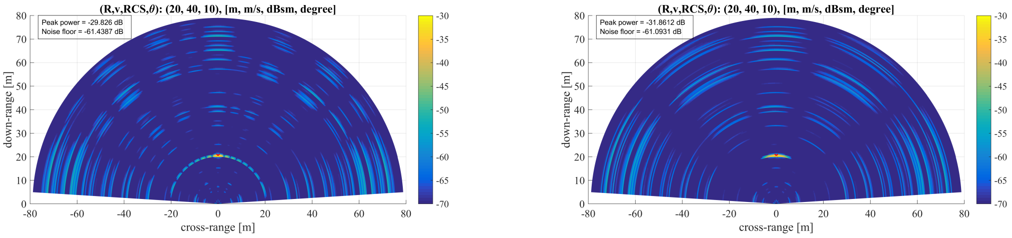

(a) No Angular Window **(b)** With Angular Window (Dolph-Chebyshev)

Figure 4.10: Range-Angular Map: ZCZ (4096)

For the APAS sequence, the artifacts are directed only in the beam that corresponds to the width of the main lobe. In this case, the energy of the artifact is higher compared to the case for the ZCZ sequence and is also present before the target's location. Besides, in contrast to the Gold and ZCZ sequences that are transmitted concurrently using CDM, the APAS sequence incorrectly estimates the target's angular position in the presence of Doppler. The error is linearly dependent on the target's velocity, as illustrated in Figure 4.9b. This phenomenon is because a nonconcurrent transmission scheme is applied, which does not take account for the position changes during the sequential TX activations for moving targets. The received signal at antenna 1 is a summed version of time-staggered transmitted waveforms

$$s_{rx,1}(t) = \sum_{n=1}^{N_T} s(t - \tau_{A,n} - t_{d,n})\, e^{j2\pi(n-1)d_t \sin(\theta)/\lambda}\, e^{j2\pi f_c t_{d,n}} \tag{4.4}$$

with n denoting the n^{th} of the transmit array, $\tau_{A,n}$ the time-staggered induced delay and $t_{d,n}$ the round-trip delay. For moving targets, unfortunately $t_{d,n}$ changes over time as targets are non-stationary. To solve this issue displacement compensation for moving targets can be implemented, but that is notes as out of the scope of this thesis. The interested reader is referred to [52] for which a design is proposed that compensates for motion in TDMA FMCW MIMO radar systems.

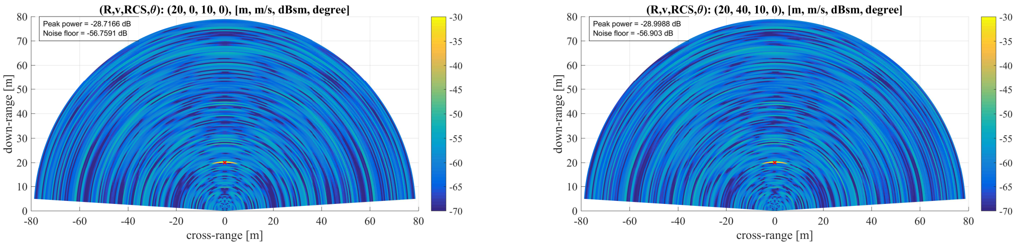

(a) $v = 0\,\mathrm{m/s}$ **(b)** $v = 40\,\mathrm{m/s}$

Figure 4.11: Range-Angular Map: Gold (2047).

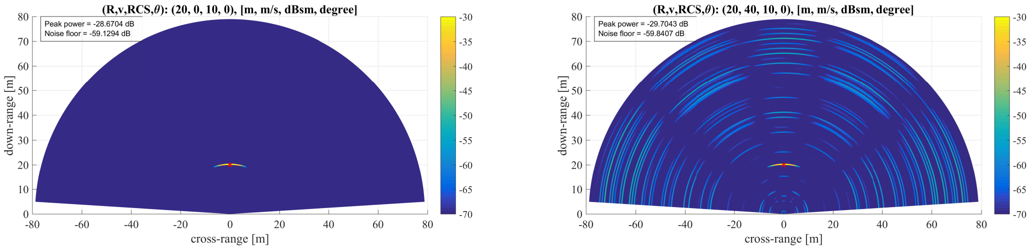

(a) $v = 0\,\mathrm{m/s}$ **(b)** $v = 40\,\mathrm{m/s}$

Figure 4.12: Range-Angular Map: ZCZ (4096).

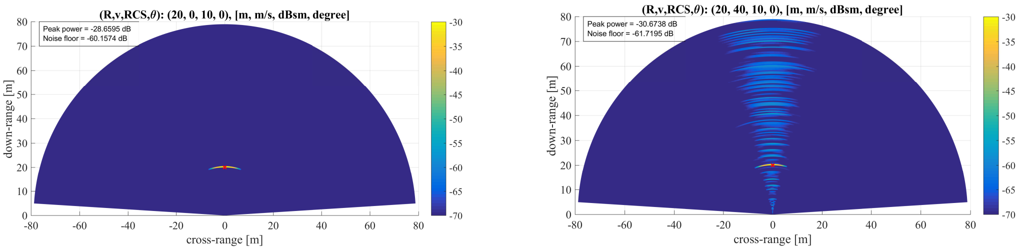

(a) $v = 0\,\mathrm{m/s}$ **(b)** $v = 40\,\mathrm{m/s}$

Figure 4.13: Range-Angular Map: APAS (5184).

4.4 Computational Complexity

Automotive radar requires high real-time update speed, since it is a real-time application. Thus, the computational complexity is another important metric. In this investigation, we can assume that the differences in correlation duration for each of the three distinct designs are negligible. However, there is a remarkable design aspect that makes the design configured with the APAS sequences (TDM) favorable in the number of correlation operations, and thus computation power, when compared to the design of the Gold and ZCZ sequence (CDM).

For realizing a virtual array of length $K_T \cdot K_R$ for the design implemented with APAS sequence, K_R correlation processes are required, since the same sequence is transmitted for all channel accesses.

For the Gold and ZCZ sequences, the realization of a virtual array of length $K_T \cdot K_R$ requires $K_T \cdot K_R$ correlation processes. Hence, all receivers need to correlate with all individual transmitted waveforms.

4.5 Conclusion

In this chapter we have examined the performance of MIMO PMCW radars systems; its autocorrelation properties, orthogonality (under the influence of Doppler), and computational complexity for each of the proposed designs of the previous chapter. The autocorrelation properties were closely inspected as the effects of the low pass filter for various cut-off frequencies were applied. It was observed that the high-frequency components play an important role and have an impact on the width of the autocorrelation peak, and thus range resolution. In this thesis, a cut-off frequency of $f_{cut} = R_c$ Hz us used, which suffices the requirements in terms of range resolution.

Afterwards, the influence of Doppler shifted versions of the transmitted waveforms have been examined, which pointed to specific imperfections for all the proposed designs. The Gold sequence showed that its naturally high range sidelobes are negligibly effected by Doppler shifts. Independent of the Doppler shift, the Range-Angular map is noisy and does not render the target's position. Radar systems configured with APAS and ZCZ sequences are affected to a greater extent by Doppler-shifted reflections, in both the Range-Doppler Map and Range-Angular Map. The range sidelobes, that are formed within the entire target's range cut, cause the Range-Angular map to reduce in performance as well. Additional to this impact, TDM Transmission results in inaccuracy in the FFT-estimated angular position of the target.

Finally, it was shown that the APAS sequence design is preferred over the Gold and ZCZ sequence design concerning the computational complexity.

Chapter 5

Asynchronous Interference

In the previous chapter, interference caused by non-orthogonality among the concurrently transmitted waveforms in the MIMO configuration has been observed. The following part of this thesis describes the effects of asynchronous interference on phase-coded radar systems. Radar-to-radar interference is considered as asynchronous, since no time-management and the lack of standardization in automotive radar implies that differences in frequency usage, bit rate, and code properties will exist. Both PMCW and FMCW waveforms will be considered as interference sources under different operative conditions. The approach of this chapter is to take generalized interference situations, instead of simulating real-world "road scenarios".

5.1 Definitions

Frequency overlap

The importance of the carrier frequency has not been addressed yet, as it leads to the advantage of multiplexing waveforms that are excited at different carrier frequencies. Assuming that, regardless of the type of waveform, two waveforms coexist (source and interferer), within the same time span but having different carrier frequencies $f_{c,S}$ and $f_{c,I}$, respectively. Then, if the carrier frequencies are well-spaced compared to the signal's bandwidth, the source signal can be separated from the interference by applying a low-pass filter that suppresses the out-of-band interference power (see Section 5.2.1). So apart from the signal division by coding, interference can be avoided by selecting a source signal, whose frequency components are not in a similar frequency spectrum as the interfering signal. However, interferce is unavoidable if the frequency spectra of the two separate waveforms overlap, the bandwidth of that specific overlap can be determined by

$$B_{OL} = \frac{B_S + B_I}{2} + |f_{c,I} - f_{c,S}| \tag{5.1}$$

where in case of BPSK-modulated waveforms B_S and B_I refer to the receiver null-to-null bandwidth, while $f_{c,S}$ and $f_{c,I}$ represent the source and interferer carrier frequency respectively.

Time overlap

Apart from the overlap in frequency components, the occurrence of the interference can be randomly distributed in time. Assuming that the interference starts illuminating the source at time $T_{I,start}$ and ends at time $T_{I,end}$, with the starting and ending time being completely random variables. Therefore, the interference period can span any period of time in the measurement time, T_{frame}, of the source. The receiver signal constitutes of reflected source signal $s_{tx,S}(t)$

and a single interference signal $s_{tx,I}(t)$

$$s_{rx}(t) = \begin{cases} s_{rx,S}(t) & \text{if } 0 \geq t > T_{I,start} \text{ and } T_{I,end} \geq t > T_{frame} \\ s_{rx,S}(t) + s_{rx,I}(t) & \text{if } T_{I,start} \geq t > T_{I,end} \end{cases} \tag{5.2}$$

where the total interference duration is denoted as $T_I = T_{I,end} - T_{I,start}$.

Accordingly, the overlap in time and frequency of the source and interferer is described in percentages, with respect to the frame time of the source T_{frame} and receiver bandwidth B_N, respectively:

$$\gamma_T = \frac{T_I}{T_{frame}} \tag{5.3}$$

$$\gamma_B = \frac{B_{OL}}{B_N} \tag{5.4}$$

Figure 5.1 represents the spectra of two waveforms that do not fully overlap in frequency, but only for 50% with respect to their main lobes.

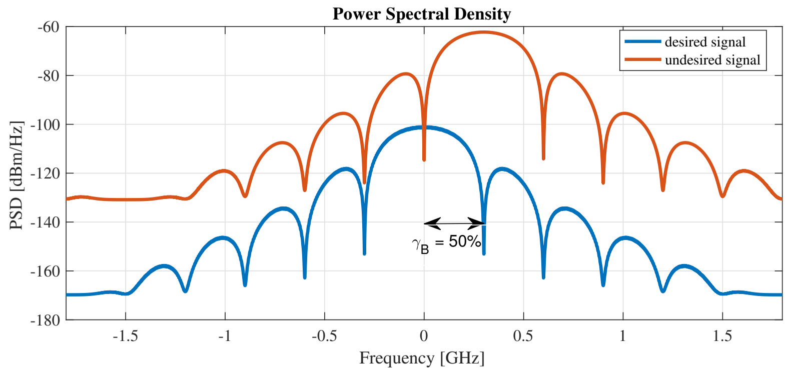

Figure 5.1: Frequency spectra overlap ($\gamma_B = 50\%$) of desired and undesired PMCW waveforms

Three-Dimensional Interference Space

The number of interference scenarios is infinte, so in order to closely observe the effects of radar-to-radar interference, scenarios are generalized using three variables: interference distance R_{INT}, time overlap γ_T and frequency overlap γ_B. Then for each combination in the three-dimensional interference space, Monte Carlo simulations are performed to gain a structured view on what will happen in that specific interference situation.

$$\begin{aligned} R_{INT} &\in [1,\ 5,\ 10,\ 20,\ 40,\ 80,\ 160] && \text{[in meters]} \\ \gamma_T &\in [1,\ 2.5,\ 5,\ 6.25,\ 12.5,\ 25,\ 37.5,\ 56.25,\ 70] && \text{[in percentage]} \\ \gamma_B &\in [5,\ 12.5,\ 17.5,\ 35,\ 60,\ 80,\ 100] && \text{[in percentage]} \end{aligned}$$

The results on the Monte Carlo simulations for each situation can be found in Appendices C, D and E. On the other hand, all results presented in this chapter are simulated for $R_{INT} = 1\,\text{m}$, $\gamma_T = 100\,\%$, and $\gamma_B = 100\,\%$.

Sensitivity Loss

For all possible combinations in the provided 3D cube, the effects will be observed. It is expected that the impact of high energy interferers (closeby, with long time duration and full bandwidth overlap) on the source radar is severe and can lead to a severe sensitivity loss. Loss in receiver sensitivity means that the maximum distance at which a target can be well-detected decreases. In radar, targets are generally detected by the Constant False Alarm Rate (CFAR) algorithm, which provides logic for determining the noise floor adaptively and detecting the targets by applying a threshold to this adaptively estimated noise floor. The threshold is usually set according to a predefined minimum SINR, which has been defined by the end user. For this thesis, a minimum SINR of 10 dB is used.

Assuming a single target of $\sigma = 0$ dBsm and single interferer, the noise power spectral density, the sensitivity loss and the minimum SINR have lead to the link budget analysis illustrated in Figure 5.2. This figure provides the maximum distances at which targets can be detected due to the loss in receiver sensitivity as given in Table 5.1. The colors in Table 5.1 match the colors of the simulation results shown in Appendix C, D and E. Here, the maximum distance R_{max} matches the range that corresponds to the maximum sensitivity loss of the indicated range of sensitivity.

Table 5.1: Reduced maximum distance in case of receiver sensitivity loss

Sensitivity Loss [dB]	Noise Floor [dBm/Hz]	R_{max} [m]
0 - 10	-159 to -149	53.0
10 - 20	-149 to -139	29.8
20 - 30	-139 to -129	16.8
> 30	> -129	9.4

In practice, the maximum distance R_{max}, as defined in Table 5.1, expresses essential information about the safety of the car. In case of a loss in receiver sensitivity of $S_L = 20$ dB, the maximum distance, for which a target with $\sigma \leq 0$ dBsm, can be observed is $R_{max} = 29.8$ m. Any target with an equivalent reflectivity that is beyond this distance will be covered under the noise floor. Therefore, the speed of the vehicle needs to be adjusted such that the car is able to brake within the time it travels the maximum distance R_{max}. In practice, a loss in receiver sensitivity requires the car to move slower.

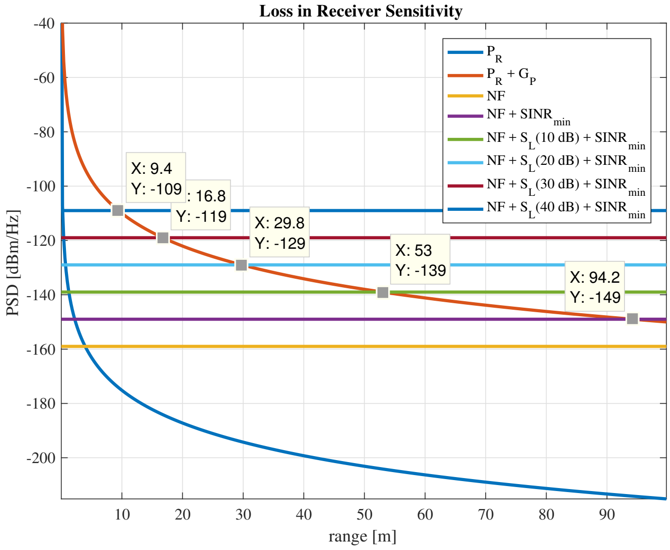

Figure 5.2: Reduced maximum distance in case of receiver sensitivity loss. The legend of this Figure denotes the following parameters: P_R as the received power, G_p as the processing gain, NF as the thermal noise power, S_L as receiver sensitivity loss, and $SINR_{min}$ as the minimum SINR required to detect a target.

5.2 Suppression Techniques in System Design

Two signal processing stages help to suppress the severeness of the interference.

5.2.1 Low-pass Filtering

Having inspected how the performance of autocorrelation function can be influenced by changing the cut-off frequency of the low pass filter in Section 4.2.1, this section addresses the advantages that the low pass filter provides in terms of out-of-band interference rejection. Figure 5.3 shows the magnitude response in frequency domain of a 2nd-order Chebyshev filter, which indicates the attenuation in power for the out-of-band frequencies. Now, assuming the case where the received signal has been down-converted to baseband, an interference waveform can have spectral components from, e.g., 500-800 MHz, then its magnitude is suppressed according to the magnitudes of this curve, which indicates a suppression of -35 to -92 dB.

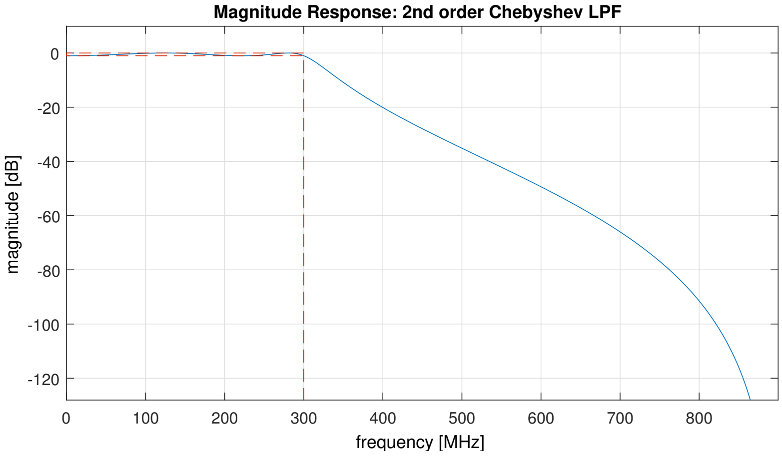

Figure 5.3: Low pass filter magnitude response

From this figure, the carrier frequency offset can be found for which out-of-band interference can be assumed to be negligible for a 2$^{\text{nd}}$-order Chebyshev LPF. In case an interferer is located at $R_{INT} = 1$ m with a null-to-null bandwidth from 400 MHz-1 GHz , then all frequency components are suppressed by at least 20 dB. This means that receiver sensitivity increases by at least 20 dB, and from Figure 5.2 the maximu distance is improved from 9.4 m to 29.8 m.

5.2.2 Doppler FFT Windowing

The Doppler FFT window is a method used to suppress velocity sidelobes in the Range-Doppler map [53]. The proposed radar design contains a Dolph-Chebyshev window with $\alpha = 4$, which suppresses all sidelobes with 80 dB compared to the main peak.

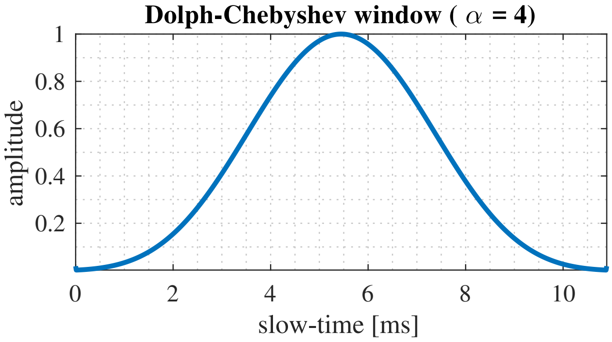

Figure 5.4: Dolph-Chebyshev window

The windows induces a loss in signal-to-noise ratio that equals [53]

$$\mathrm{SNR}_L = \frac{1}{N}\frac{|\sum_{n=0}^{N-1} w[n]|^2}{\sum_{n=0}^{N-1} |w[n]|^2} \tag{5.5}$$

The time duration and time instance of interference occurrence heavily determines the impact that the interference has on the source radar. Figure 5.4 shows the Chebyshev window, which is a discrete window whose length is equal to the number of FFT points, N_{FFT}. In the Doppler processing stage, for all individual fast-time samples, the slow-time samples are multiplied by the windowing function before the FFT is taken. Therefore, this declares that interference is attenuated more at the beginning or end of a measurement frame. Figure 5.5 illustrates this effect. Each figure represents an interference occurrence of 2 ms, but with the start moment of $T_{I,start}$ = 0, 2.5 and 5 ms shown in Figures 5.5a, 5.5b and 5.5c respectively. Therefore, the corresponding noise floors also measure −152.39 dBm/Hz, −134.02 dBm/Hz, and −130.38 dBm/Hz.

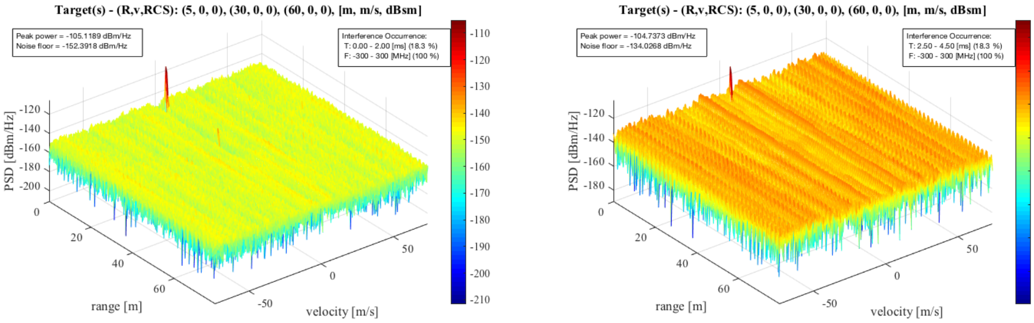

(a) $T_{I,start} = 0\,\mathrm{ms}$ **(b)** $T_{I,start} = 2.5\,\mathrm{ms}$

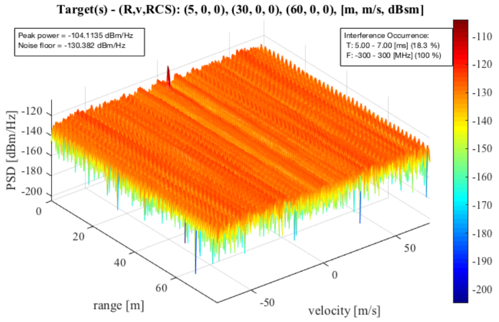

(c) $T_{I,start} = 5\,\mathrm{ms}$

Figure 5.5: Different time occurrences of the exact same (uncorrelated) interference signal ($\gamma_T = 18.3\%$, $\gamma_B = 100\%$)

5.3 FMCW-to-FMCW Interference

As previously stated, the FMCW-to-FMCW interference has become a more familiar issue in the last couple of years. Due to its predominance in the automotive market, many researchers and industrial companies investigate the effects of FMCW-to-FMCW interference. NXP Semiconductors deeply analyzed the problems that might occur. For this thesis, several results of internal work were provided by NXP Semiconductors for comparison purposes. These results can be found in Appendix C, but are confidential and will be left out of the public version of this document.

5.4 PMCW-to-PMCW Interference

As stated before, PMCW-to-PMCW interference has only been inspected using simulation models. These studies did not completely show the interference effects in PMCW radar systems. In this thesis, the internal results on FMCW-to-FMCW interference from NXP Semiconductors are used as a benchmark for comparison it to the effects in PMCW-to-PMCW Interference. The parameters of the source and interer in PMCW-to-PMCW interference simulations match to the parameters in the prior-mentioned simulations from NXP Semiconductors. Apart from equalizing the transmit power levels, antenna gains and target characteristic, the time-bandwidth product is matched as well, which is equal to

$$G_p = 65.15\,\text{dB} \tag{5.6}$$

This chapter only presents results for which full time and bandwidth overlap is assumed. Furthermore, SISO radar systems are considered to isolate the issue completely.

The simulation results for partially overlaps in time and frequency, can be found in Appendix D and E. To generalize the interference effects, in all simulations, the interference starts to illuminate the source at 3 ms. Through this way, the influence of the specific time of occurrence (as explained in Section 5.2.2) is removed, which has been decided for comparison purposes. Appendices D and E present interference illustrations for different time and frequency overlap combinations of $\gamma_T = 5\%\,,\ 25\%\,,\ 70\%$ and $\gamma_B = 17.5\%\,,\ 80\%\,,\ 100\%$.

5.4.1 Correlated Interference: Identical Sequence

First, we discuss the correlated case of interference, which is probably the most intuitive type of PMWC interference. Especially, if the undesired waveform is emitted at the same center frequency, it is expected that the identical sequence forms a non-existing target, which in the jargon of radar engineers is called a ghost target. The range to the ghost target can actually be anywhere and depends on the lag of the bit of the interference code that starts illuminating the source at time $T_{i,start}$. Mathematically, this phenomenon can be denoted by a circular shift by a certain number of lags of the interer's code, where e.g., a shift with k lags refers to a range according to this delay. Figure 5.6 illustrates a ghost target at $R_I = 56\,\text{m}$, having sidelobes in velocity at levels $-80\,\text{dBm}$ less with respect to the main ghost's target position, according to the Dolph-Chebyshev window.

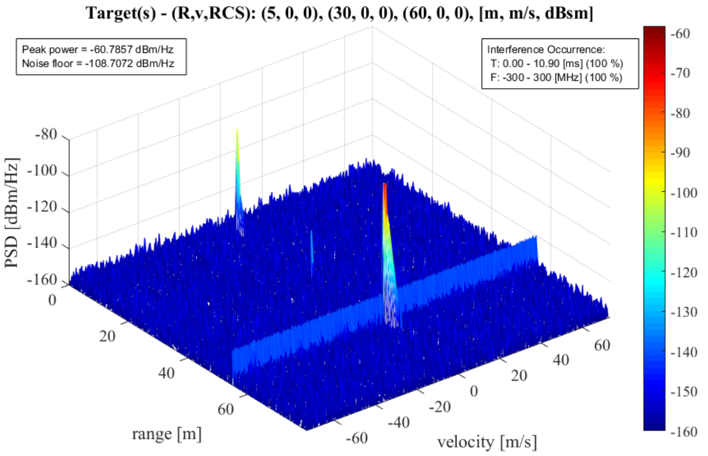

Figure 5.6: PMCW-to-PMCW (In-Band) Interference: Identical Sequence

For the MIMO system designs of Chapter 3, the design choices are made such, in order to retrieve (sub)optimal correlation characteristics, sequences are longer than required for the range of interest. Therefore, in these cases (except for the APAS MIMO design), the ghost targets can be imitated at outside the range of interest ($R > 80\,\text{m}$).

Figures D.2a-D.2f present the interference effects in case the identical sequence is received, but now distorted by a carrier offset (read: a large Doppler shift). In Chapter 4, the effects from Doppler shifts have been observed, which now return, but in an extreme case. As peak power is highly reduced and the sidelobes large increased by the Doppler distortions, the interfererce signal results in a ridge. Again, the estimated velocity reflects to the Doppler shift caused by the carrier frequency offset.

5.4.2 Uncorrelated Interference: Different Configurations

In Section 2.5.2, Figure 2.8 gives estimates on the noise, target, and interference powers using a link budget analysis for full time and bandwidth overlap. By including the processing gain, the three target powers at respectively $R_T = 5$m, 30m, and 60m, are equal to

$$
\begin{aligned}
P_{R,d}(R_{T1} = 5\,\text{m}) + G_p &= -97.99\,\text{dBm/Hz}\,, && (5.7)\\
P_{R,d}(R_{T2} = 30\,\text{m}) + G_p &= -129.1\,\text{dBm/Hz}\,, && (5.8)\\
P_{R,d}(R_{T3} = 60\,\text{m}) + G_p &= -141.2\,\text{dBm/Hz} && (5.9)\\
& && (5.10)
\end{aligned}
$$

and the noise-plus-interference power for an interferer at $R_I = 1m$ is

$$P_N + P_{R,u}(R_{INT} = 1\,\text{m}) = -124.2\,\text{dBm/Hz}\,. \tag{5.11}$$

This section compares these theoretically-obtained power levels with the numerically-obtained power levels. The types of uncorrelated interference that can appear, are listed below.

Different Code Family

Let us consider interference of a different code family and code length, respectively APAS (3868) and ZCZ(4096) sequences are used. The parameters used are listed in Table D.4. The considered source and interference waveforms are of unequal duration, which creates randomness in the range and velocity estimation processes.

For range correlation, the source signal is unaffected and is delayed according to its round-trip delay. This repetitive pattern is found in the slow-time samples. Thus, the phase relation over the slow-time samples remains the same, indicating that the FFT operation can estimate the frequency offset due to Doppler.

The interference waveform differs from the source in period duration. Therefore, the cross-correlation of the two waveforms changes over the slow-time periods. For this reason, the slow-time outputs of the sliding correlator are not coherently added, which does not lead to any significant peaks. Besides, the inconsistency in code length also destroys the phase relation in time. This withholds the radar from observing peaks in Doppler induced by the interference.

Figure 5.7 presents the Range-Doppler output for this type of interference in the worst case scenario. The image shows a structural pattern in range for which the energy is spread out over the complete Range-Doppler map. The annotation box in 5.7 shows that the measured noise floor is equal to $-123.42\,\mathrm{dBm/Hz}$, and approaches the theoretical noise-plus-interference power of (5.5).

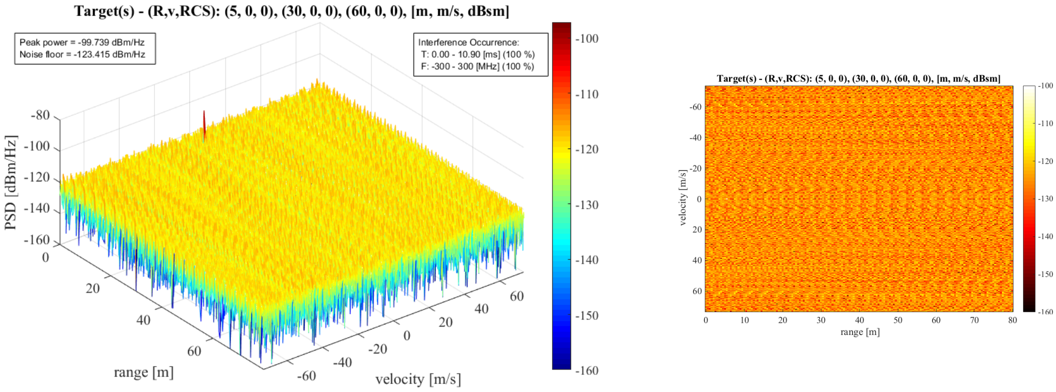

Figure 5.7: PMCW-to-PMCW (In-Band) Interference: Different Code Family

Different Code Length

The previous situation already demonstrated two waveforms from different code families with a different period duration. Now, this section discusses the effects for two waveforms of the same code family but non-equal code lengths, namely APAS(3868) and APAS(3864). Again a similar phenomenon happens; however, the energy is spread over the Range-Doppler map in a slightly different manner. Figure 5.8 depicts that the patterns are structured more along the range gates.

An exceptional situation occurs, when the code length is of the interferer is of multiple length of the source code. We discuss the case for ZCZ sequences, of length 4096 (source) and 2048 (interferer). These lengths indicate that in every slow-time period of the source fit precisely two periods of the interferer. This means that the phase relation over the slow-time samples remains constant, and the interference energy is concentrated in a single ridge in the zero-Doppler cut (see Figure 5.9). In case of an interferer having a different carrier frequency (See Figures D.4a to D.4f), the ridge is shifted to a velocity according to the offset in carrier frequency. In fact, it acts like a Doppler shift from a moving target. As the offset in carrier frequency exceeds the frequency, for which the maximum velocity of the design has been specified, the ridges aliases to the negative frequencies. This phenomenon of spectrum folding withholds the system from estimating the corresponding frequency offset, because of ambiguity.

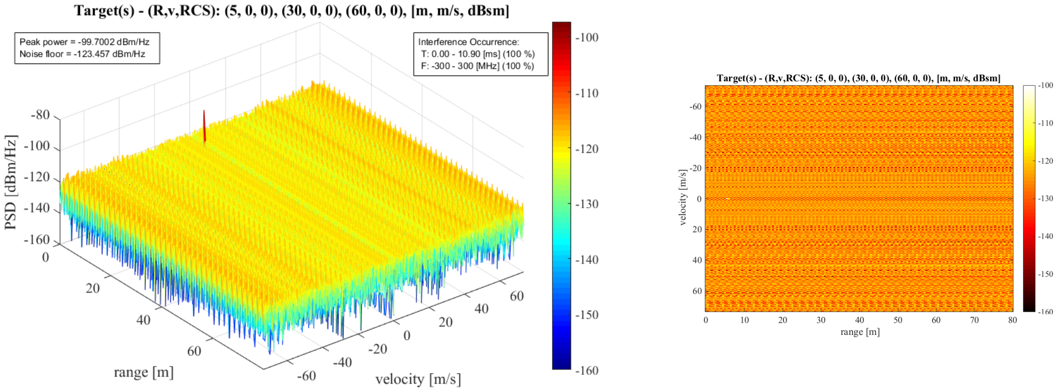

Figure 5.8: PMCW-to-PMCW (In-Band) Interference: Different (Random) Code Length.

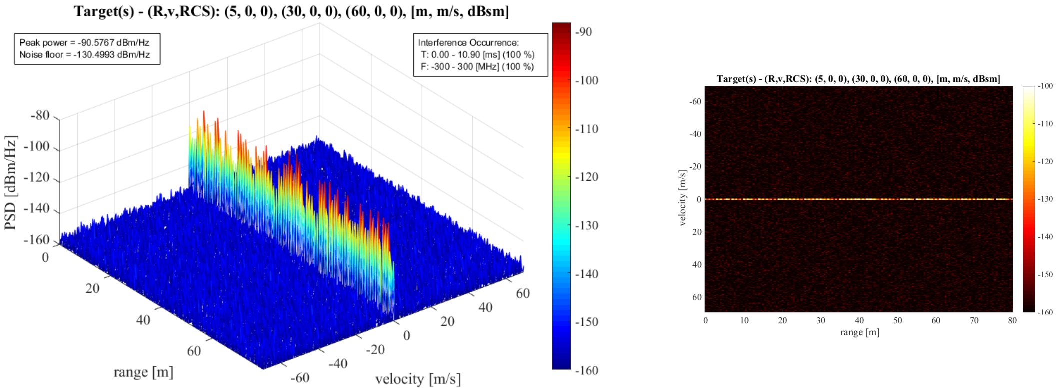

Figure 5.9: PMCW-to-PMCW (In-Band) Interference: Different (Multiple) Code Length.

Different Bandwidth

The lack in standardization in automotive radar implies that every manufacturer can configure its radar to comply with its demands. In PMCW, the bit rate and bandwidth go hand in hand. At first, we have analyzed the case where an LRR configured with the APAS(1308) sequence interferes with an MRR APAS(3868) radar. By our definitions, the LRR range is configured to have a bit rate that is twice as small (150MHz) compared to the MRR radar, which implies that the chip duration is twice as long. Then, similar as in the previous two uncorrelated situations, the noise-plus-interference power behaves in a uniform and randomized manner, due to the difference in code length (see Figure 5.10), where the noise floor measures $-124.30\,\mathrm{dBm/Hz}$.

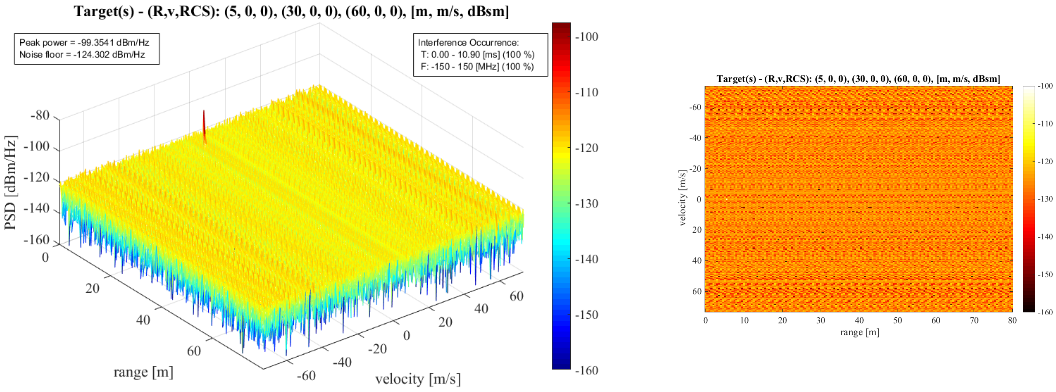

Figure 5.10: PMCW-to-PMCW (In-Band) Interference: Different Bandwidth and Code Length

Analogous to the specific code length case where the interference waveform spanned half of the waveform duration of the source, a similar situation can happen when codes are transmitted at multiple bit rates (assuming similar code lengths for the source and interferer). Similar code length implies that the duration of the waveform period reduces the maximum velocity. Although this might be unpractical, e.g. as LRR radar is required to measure large relative velocities on the highway, we are still investigating its interference effects.

Figure 5.11 presents the effects for different bit rates of the interferer's coded waveform. The simulations setups are configured such that the source's bit rate $R_{c,SRC}$ is a multiplicative factor larger than the interferer's bit rate $R_{c,INT}$. The problem can be generalized by $R_{c,SRC} = R_{c,INT}/K$, where K can be any integer larger than zero. Then, in Figure 5.11a the effect is shown for $K = 2$; Figure 5.11b illustrates the effect for $K = 3$, etc.

Observing Figure 5.11 has lead to locate the ridges at the following velocities

$$v_{ridge,k} = \pm k\frac{2v_u}{K} \qquad \text{for } k = 0, 1, 2, \ldots, K-2 \tag{5.12}$$

For the simulations of Figure 5.11, the maximum detectable velocity equals

$$v_u = \pm 73.58\,\mathrm{m/s} \tag{5.13}$$

what lead to the ridges at the following velocities

$$K := 2 \quad \Rightarrow \quad v_{ridge} = \{0,\ \pm 73.58\} \tag{5.14}$$

$$K := 3 \quad \Rightarrow \quad v_{ridge} = \{0,\ \pm 49.05\} \tag{5.15}$$

$$K := 4 \quad \Rightarrow \quad v_{ridge} = \{0,\ \pm 36.79,\ \pm 73.58\} \tag{5.16}$$

$$K := 5 \quad \Rightarrow \quad v_{ridge} = \{0,\ \pm 29.43,\ \pm 58.87\} \tag{5.17}$$

Note that, for K is uneven, the ridges found from (5.12) for even k are less significant compared to the ridges found for uneven k.

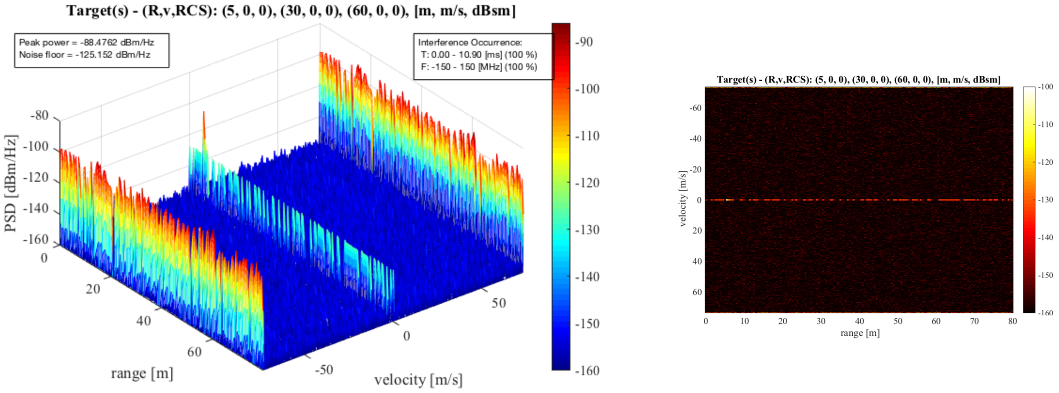

(a) $B_{INT} = \frac{1}{2} B_{SRC}$

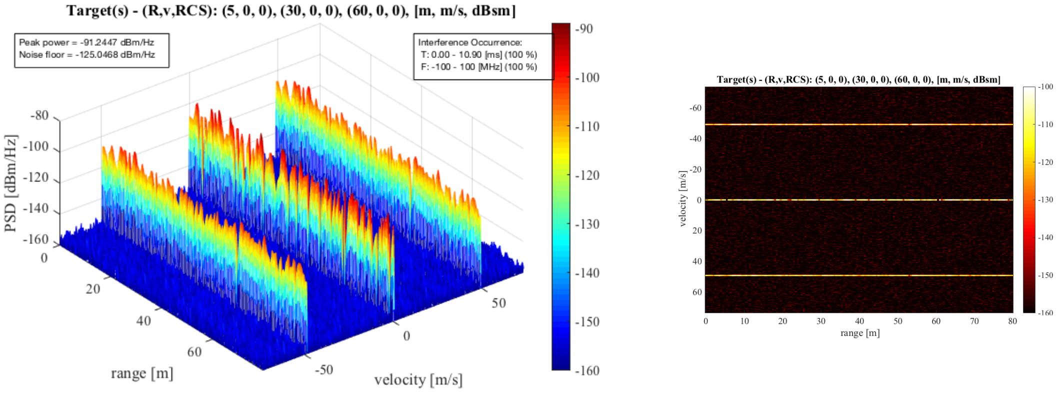

(b) $B_{INT} = \frac{1}{3} B_{SRC}$

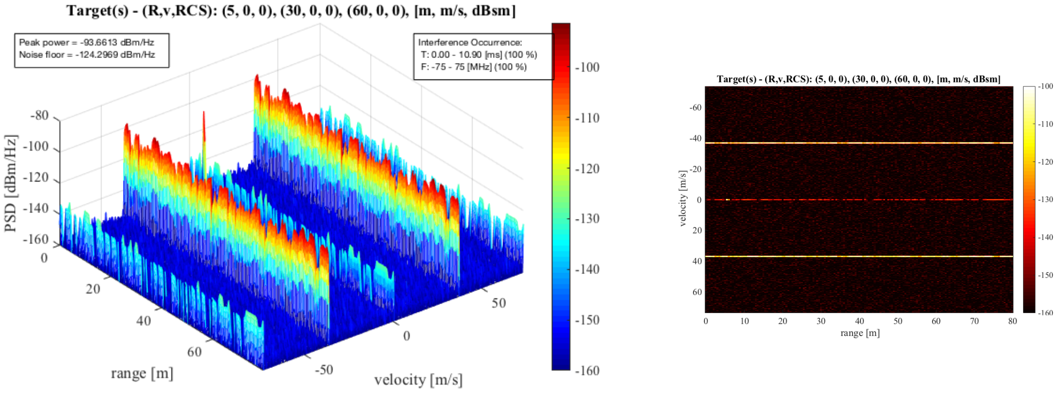

(c) $B_{INT} = \frac{1}{4} B_{SRC}$

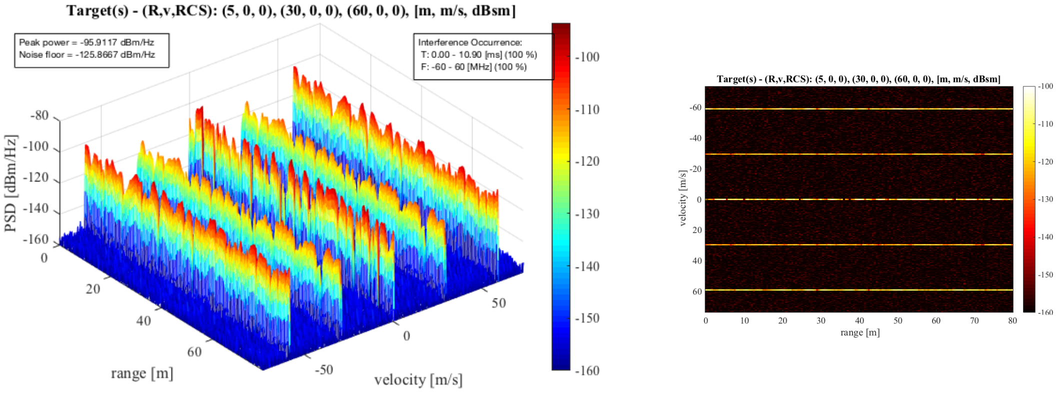

(d) $B_{INT} = \frac{1}{5} B_{SRC}$

Figure 5.11: PMCW-to-PMCW (In-Band) Interference: Different (multiple) Bandwidth

5.5 FMCW-to-PMCW Interference

According to the parameters of Table E.1 the influences of FMCW waveforms have been investigated on PMCW radar systems. This single situation does not give a complete overview on the interference issue, but at least for this specific case of the bandwidth and waveform duration (thus, the slope of FM ramp). Again, for the above-explained case, the influences on the PMCW radar systems can be designated as uncorrelated and random. In contrast to the previous cases, where a structural pattern could be observed in some sense, the behavior of frequency-modulated waveforms is mainly random over range and velocity (See Figure 5.12).

Also, the interference-plus-noise power increases according to the link budget analysis, where theoretically $-124.2\,\mathrm{dBm/Hz}$ from is compared with the numerically $-124\ 56\mathrm{dBm/Hz}$ in the worst case scenario

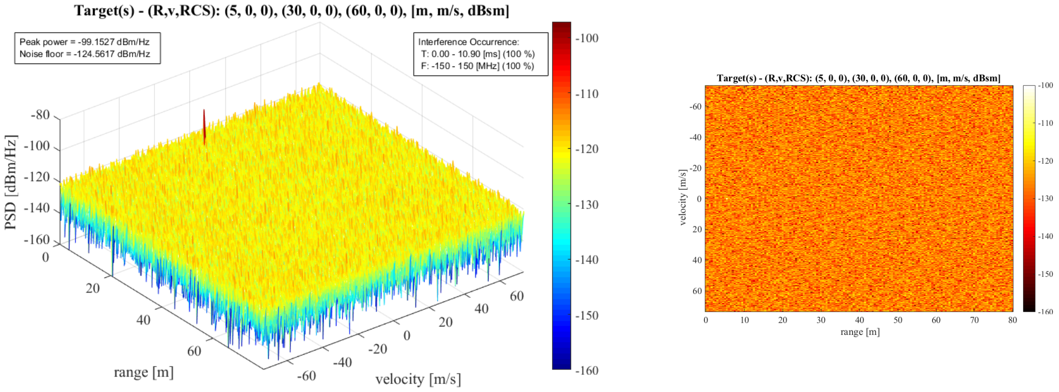

Figure 5.12: FMCW-to-PMCW (In-Band) Interference

5.6 Comparing FMCW and PMCW: Radar-to-Radar Interference

The previous studies in this thesis on radar interference showed that different radar setups with different waveform durations lead to uncorrelated signals. In this case, the energy of these uncorrelated waveforms spreads out over the complete Range-Doppler map. The uncorrelated interference can be compared for full time and bandwidth overlap. Simulations have been executed for different interference ranges R_{INT} and different time occurrences γ_T. For FMCW-to-FMCW radar, these simulation results have been tabulated in Table C.1.

For PMCW-to-PMCW radar, the additional degree of freedom by using codes increases the likelihood of uncorrelated signals. In the previous sections these impacts were investigated and classified in Tables D.5, D.8, D.11 and D.14, which can be concluded by the remark that, if the waveform period duration for the source and interferer are unequal, the uncorrelated effects similar to FMCW radar are shown. Note that this also holds for dissimilar PRI of FMCW waveforms.

Interestingly, it can be concluded that in the presence of radar-to-radar interference and in the case of asynchronous radar systems (without time management), PMCW waveforms do not provide benefits, compared to FMCW waveforms. After digital processing, still similar energy levels hold, which leads to the conclusion that codes do not remove the interference energy, but spreads out over the Range-Doppler map. Therefore, both radar systems have to account for similar losses in receiver sensitivity assuming an equal amount of interference energy that comes in, regardless of the type of waveform.

5.7 Conclusion

For PMCW-to-PMCW interference, the following conclusions can be drawn:

1. The low pass filter and the FFT window can alleviate the impact of the interference.
2. Ghost targets can be created when (nearly) identical configurations are being used.
3. In case the configurations of the source and interferer mismatch, then Tables D.5, D.8, D.11, D.14 show that the uncorrelated interference causes a loss in receiver sensitivity by an increase in noise floor. This increase, in the worst case, matches the interference-plus-noise power as analytically calculated from the link budget analysis.
4. There are situations where uncorrelated interference does not lead to a consistent increase in the noise floor, but to one or multiple ridges along range in the Range-Doppler map. This happens when the slow-time period duration of the source and interferer is a multiple of the other, or vice versa. The two cases for which this occurs are:
   (a) $R_{c,SRC} = R_{c,INT}$ and $L_{c,SRC} = nL_{c,INT}$
   (b) $R_{c,SRC} = nR_{c,INT}$ and $L_{c,SRC} = L_{c,INT}$

   where n is an integer or its reciprocal, unequal to zero. Then, if there is also a mismatch in carrier frequency, the ridge shifts to the velocity as a Doppler shift. For large carrier offsets, aliasing in Doppler keeps the ridge within the Range-Doppler map.

FMCW-to-PMCW interference has been shortly addressed; for non-equal waveform period duration. Again, the interference power is spread out uniformly in the Range-Doppler map, according to the interference-plus-noise power calculated by a link budget analysis.

The simulations have provided insights on the interference effects in a PMCW receiver. By comparing FMCW-to-FMCW interference to PMCW-to-PMCW interference (Table C.1 with Tables D.5, D.8, D.11, D.14), for uncorrelated waveforms specifically, we can conclude that PMCW radar systems do not provide advantages regarding the receiver sensitivity loss in asynchronous cases. Although if in future, some form of time management and certainty on the transmitted codes exist, it can definitely benefit from the additional degree of freedom and achieve the low correlation values as found in Chapter 4.

Chapter 6

Experimental Validation

To validate the radar-to-radar interference results obtained from the simulation model of Chapter 5, experiments are done in baseband. Due to unavailability of radar embodiments appropriate for 79 GHz PMCW radar, the experiments are performed using an Arbitrary Waveform Generator (AWG), RF cables, a coaxial waveform combiner, and an oscilloscope, which are provided by Delft University of Technology.

6.1 Measurement Setup

To imitate a radar scenario on 79 GHz, this experimental setup consists of an AWG, combiner and ADC. The setup is shown in Figure 6.1. Table 6.1 shows the apparatus that were used in the experiments.

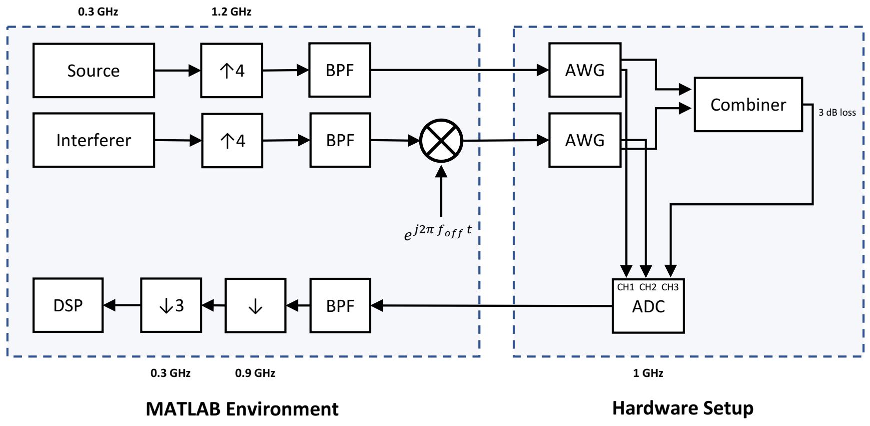

Figure 6.1: Measurement Setup

Table 6.1: Measurement apparatus

AWG	Tektronix AWG5014B	[54]
Combiner	Mini-Circuits Power Splitter/Combiner ZX-10-2-12-S+	[55]
Sampling oscilloscope	Agilent DSO-X-91604A	[56]

Signal generation for the coded waveforms of the source and interferer are done in the digital domain using MATLAB environment. Initially, the bitrate of the source and interfererce signal is equal to 300 MHz, similar to bitrate used in the simulations of Chapter 5. The sub-pulses are oversampled by a factor four, such that the sampling frequency of the discretized coded waveform is equal to the maximum sampling rate of the AWG, which equals 1.2 GSa/s. In the digital domain, the interference signal could be initialized by a frequency offset for observing the effects of partial bandwidth overlap of the two waveforms. Note that both signals must only contain real values.

The real-valued txt-files are read in the Tektronix AWG5014B AWG, which outputs two analog waveforms. Both outputs are connected to the Mini-Circuits Power Combiner using RF cables. Furthermore, the created analog waveforms are also directly attached to the Analog-to-Digital Converter (ADC), by using two separate RF cables, indicated by *CH1* and *CH2* respectively. A third channel, *CH3*, inputs the combined version of the source and interference waveforms.

To imitate a target, the round-trip delay is already fixed in MATLAB using zero-padding. Assuming a single static target at R = 5 m results in a delay $\tau = 33.36\,\text{ns}$. Accordingly, the amplitude of the source waveform is equal to 0.0113 mV based on the two-way round trip attenuation losses. The amplitude of the interference signal is used as reference, with a magnitude of 1 mV, which starts interfering the source at $T_{I,start} = 3\,\text{ms}$. Figures 6.2a and 6.2b depict the real-time analog waveforms presented on the oscilloscope. The first figure shows a PMCW interfered waveform for an 70% occurrence in time, while the second figure represents an FMCW radar interfering for a period of 25% of the source's signal duration.

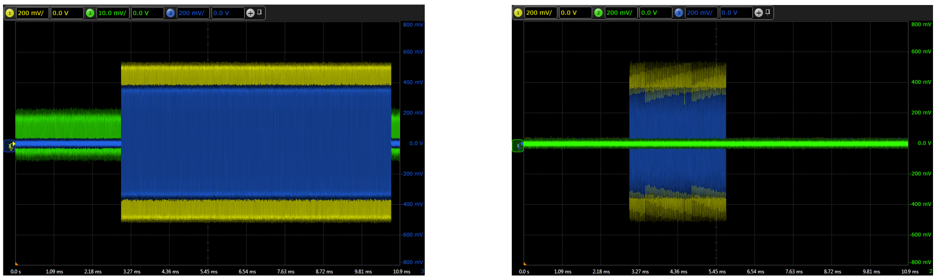

(a) 70% Interference occurrence of PMCW waveform

(b) 25% Interference occurrence of FMCW waveform

Figure 6.2: Output of the oscilloscope

The sampling rate of the ADC could be arbitrarily chosen from $F_{s,adc} = 0.1, 0.2, 0.5, 0.5, 1, 2, 4, 10$ up to 40 GSa/s. This indicates a problem, since these values are non-multiple rates of R_c. Therefore, the sampling frequency of the ADC $F_{s,adc} = 1\,\text{GSa/s}$ was selected. It means that interpolation of the digitized waveform in MATLAB is required, which leads to the interpolated sampling rate of $F_s = 0.9\,\text{GSa/s}$. Accordingly, the signal is downsampled to R_c. The impact of interpolation of the receive signal has been shortly investigated. The effects on reception were negligible, as can be observed in Figure 6.3. Note that the the received signal is attenuated by approximately a factor of two, when compared to the transmitted waveforms. The input of the combiner (not shown) is even more attenuated because of the Power combiner itself.

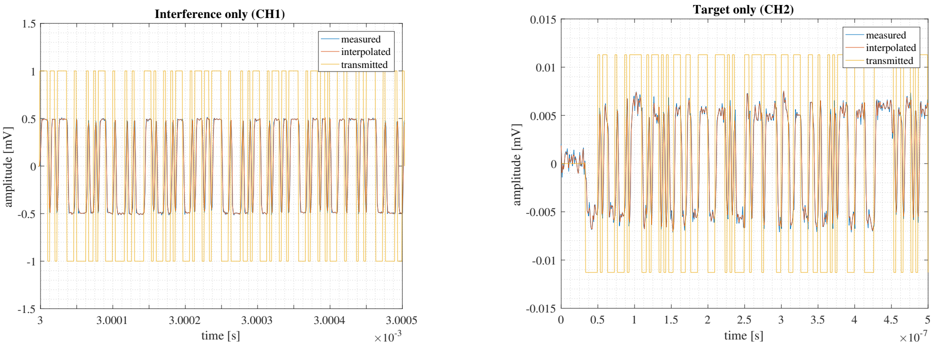

(a) Interference

(b) Target's reflection

Figure 6.3: Signal separation by using three input channels of the oscilloscope.

6.2 Results

In this section, we discuss three distinct situations: two PMCW-to-PMCW interference situations (non-multiple and multiple slow-time period duration, respectively) and FMCW-to-PMCW interference. For the PMCW-to-PMCW situation, where the slow-time period of the source and interferer are non-multiples, the situation of two codes from the same code familiy but different code length was selected. The other uncorrelated situations are left out, as they show similar behavior.

Despite the fact that the amplitudes of the baseband waveforms have been selected according to the pathloss model, its magnitudes are incomparable to the realistically received magnitudes. The input voltages in the AWG cannot be realized as the original simulated magnitudes. Therefore, we expect the received power level to deviate from the simulation model. Also, the noise power might deviate from the simulated case, since the Analog-to-Digital converter has a different noise figure. For this reason, we firstly retrieved a reference situation, where only the source signal exists (CH1). The obtained noise floor from the simulation environment and from the measurements are respectively: $-157.41\,\text{dBm/Hz}$ and $-133.83\,\text{dBm/Hz}$ (see Figure 6.4). Now, in Sections 6.2.1 to 6.2.3, it is observed is the similar effects show up as the ones found in Chapter 5. The metric of interest is the sensitivity loss, and whether the rise in noise floor matches the rise in noise floor obtained from the simulations.

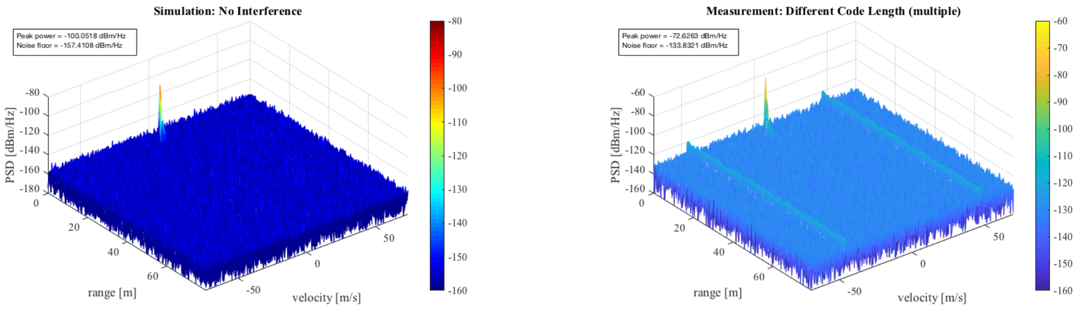

(a) Simulation **(b)** Measurement (CH1)

Figure 6.4: Range-Doppler maps: Interference-free

6.2.1 PMCW-to-PMCW: Uncorrelated – Non-multiple slow-time period

In Section 5.4.2 it was observed that for PMCW-to-PMCW interference, a uniform increase in the noise floor arises when the interference periodic signal is not equal to a multiple of slow-time period of the source.

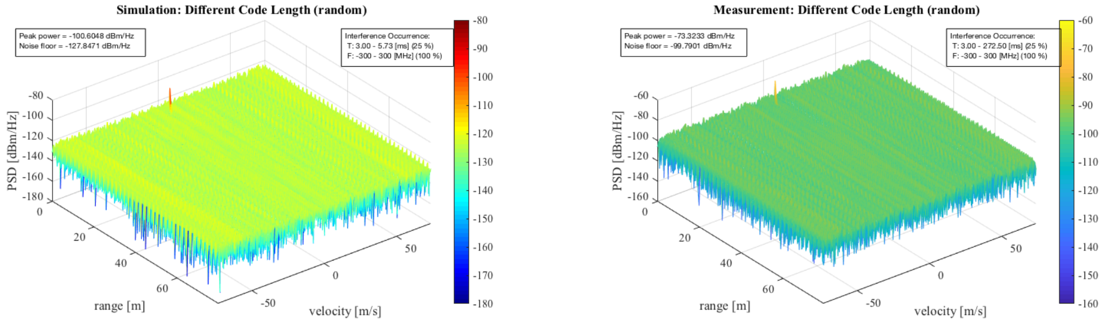

(a) Sensitivity Loss: $S_L = 29.56\,\text{dB}$ **(b)** Sensitivity Loss: $S_L = 34.04\,\text{dB}$

Figure 6.5: In-Band Interference: Different Code Length (non-multiple)

The loss in receiver sensitivity is presented in Figures 6.5a and 6.5b, and shows that for the simulation and measurement the loss in receiver sensitivity is equal to

$$S_{L,sim} = 29.56\,\text{dB} \tag{6.1}$$

$$S_{L,meas} = 34.04\,\text{dB} \tag{6.2}$$

The difference of 4.48 dB between the simulation model and the measurements is larger than expected. However, these results originate from two independent snapshots, for a more notable conclusion on this difference more than one measurement needs to be taken. Figures 6.5a and 6.5b show that the interference pattern is similar for both the simulation and measurement.

6.2.2 PMCW-to-PMCW: Uncorrelated – Multiple slow-time period

In the exceptional case that the PRI of the interference is a multiple of the PRI of the source, a single ridge is formed. According to the carrier frequency offset, the ridge is found at a specific velocity. In baseband processing that is relevant to this section, the carrier frequency offset is zero, meaning the ridge is found at zero Doppler. The formed ridge causes the sensitivity in the receiver to be larger for the experiment setup compared to the simulation model:

$$S_{L,sim} = 24.00\,\text{dB} \tag{6.3}$$

$$S_{L,meas} = 26.43\,\text{dB} \tag{6.4}$$

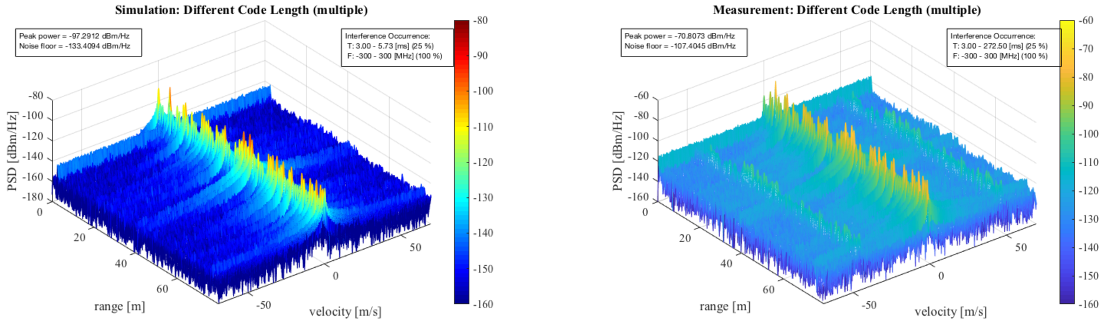

(a) Sensitivity Loss: $S_L = 24.00\,\text{dB}$

(b) Sensitivity Loss: $S_L = 26.43\,\text{dB}$

Figure 6.6: In-Band Interference: Different Code Length (multiple)

6.2.3 FMCW-to-PMCW Interference

As seen before, an FMCW waveforms of a different waveform duration than the source resulted in an equivalent effect as for uncorrelated PMCW waveforms. The receiver sensitivity loss is retrieved from Figures 6.7a and 6.7b and is quantified as

$$S_{L,sim} = 29.37\,\text{dB} \tag{6.5}$$

$$S_{L,meas} = 29.41\,\text{dB} \tag{6.6}$$

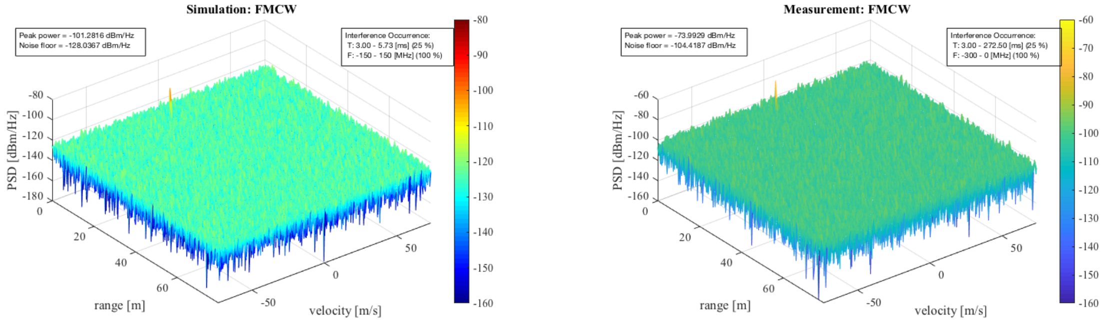

(a) Sensitivity Loss: $S_L = 29.37\,\text{dB}$

(b) Sensitivity Loss: $S_L = 29.41\,\text{dB}$

Figure 6.7: In-Band Interference: FMCW

6.3 Conclusion

The measurements results, as presented in this chapter, have proven that the simulation environment of Chapter 5 delivers the correct output in terms of interference power levels and patterns. The measurements do not contain any unexpected processing outputs. The loss in receiver sensitivity is consistent for the simulations and measurements, and is of similar order of magnitude. The receiver sensitivity from the simulation may slightly differ from those of the measurements, but the general effects match. The only unexpected finding can be observed in Figures 6.4b and 6.6b. Two narrow and inconsiderable ridges are found at $\pm 46.34\,\text{m/s}$. These ridges are not caused by the interference, since these artifacts also show up in the interference-free channels. This implies that the ridges are formed by non-idealities of the measurement setup, but the exact reasoning for these artifacts is not investigated.

Chapter 7

Conclusion

In the final chapter, we summarize the work of this thesis, draw conclusions and suggest directions for the further research.

7.1 Conclusions

This project was undertaken to design and simulate a MIMO PMCW radar system. After the literature review; the Gold, ZCZ and APAS sequences were selected as the three most promising code families in Chapter 3. For the synchronous case, in particular MIMO PMCW radar, a comprehensive overview was given in Chapter 4 of the predefined MIMO system designs. It showed the strengths and shortcomings of the three distinct designs and gave preference to the APAS and ZCZ code family.

The primary aim of this research was to examine the performance of a PMCW radar in the presence of interference and whether it would provide benefits in comparison to FMCW radar. The following conclusions for asynchronous radar-to-radar interference, which have been realized by the simulations and measurements of Chapters 5 and 6, can be taken:

- Correlated interference in PMCW radar systems creates a ghost target, only if the carrier frequency of the source and interference are approximately equal. Otherwise, for significant carrier frequency offsets, the interference causes a ridge that is folded to the velocity corresponding to the frequency (Doppler) shift.

- Uncorrelated interference in PMCW radar systems can be subdivided into two subcategories: non-multiple and multiple slow-time duration of the source and interference waveforms.
  In the case the source slow-time duration is not a multiple of the interferer slow-time duration, the interference energy is spread out evenly over the full Range-Doppler map. This rise in noise floor matches to the interference-plus-noise power calculated from the link budget analysis.
  In the case the source slow-time duration is a multiple of the interferer slow-time duration, the interference energy is concentrated as a ridge in one or multiple Doppler bins of the Range-Doppler map. The number of ridges depends on the difference factor in slow-time duration. Carrier frequency offsets cause the ridge(s) to fold in the velocity spectrum.

- The interference effects often exhibit uncorrelated noise behavior, as no clear and evident patterns are found, making it harder to detect and mitigate PMCW-to-PMCW interference.

- The three points mentioned above conclude that the interference levels are not naturally removed or suppressed in the coding domain, and are hard to mitigate due to their noise-like behavior. In the general situations that have been discussed the interference levels in PMCW-to-PMCW interference approach the levels found in FMCW-to-FMCW interference. However, as the probability of interference occurrence is not equal in both systems, no conclusive answer can be assigned to the research question if PMCW systems can better reject interference in comparison to FMCW systems.

7.2 Future Work

The following recommendations are provided to further enhance the knowledge on interference in MIMO PMCW radars:

- Due to limited time, only one specific situation of FMCW-to-PMCW interference was investigated. However, the number of interfering FMCW waveforms can be extended, to observe if characterizing patterns can be found, by simulation more FMCW waveforms with differences in transmit bandwidth, frequency ramp, waveform duration, etc.
- Detection techniques for PMCW interference remain to be unsolved. Other than detection by setting a threshold to measure the noise floor, are there any techniques that recognize specific patterns in the Range-Doppler map.
- After having designed practical detection techniques, the interference needs to be mitigated by using analog or digital signal processing techniques.
- Finally, and most importantly, to complete the picture of the comparison between interference in FMCW and PMCW radar systems, a more practical related interference study needs to be done. In this study, the probability of interference occurrence needs to be coupled to the severeness of interference, which is needed to give preference to either FMCW or PMCW radar systems and their interference rejection capabilities.

Appendix A

Algorithms for Generating Different Code Families

A.1 APAS sequences

As explained in Section 3.1.3, in 1995, the constraints for generating APAS sequence has been published [42]. This section provides a more extensive and computation-oriented approach than for generating APAS sequences:

1. Find an arbitrary p, which will be equivalent to the width of the zero autocorrelation zone ($L_c/2 - 1$). The constraint here is that L_c must be a multiple of 4.
2. Use the C program from [57] to generate the primitive polynomial that corresponds to p. Several primitive polynomial have been listed in Table A.1.
3. Rewrite the primitive polynomial to the form of a feedback polynomial. Again, feedback polynomials are provided in Table A.1.
4. Generate a *p-ary* M-sequence using a $p - ary$ Galois Linear Feedback Shift Register (GLFSR).
5. Then, the APAS sequence a of length is retrieved by initializing all $2(p-1)$ bits with -1, after which every bit j of the *p-ary* m-sequence output is compared to '1', if true then the j^{th} bit of a is set to '1'.

Table A.1 has listed the primitive polynomials and feedback polynomials for several (read: not all) prime numbers p and the generated APAS code lengths L_c.

Table A.1: Primitive polynomials and feedback polynomials for different APAS code lengths

p	L_c	**primitive polynomial**	**feedback polynomial**
29	60	x^2 + x + 3	19 x^2 + 19x -1
53	108	x^2 + x + 5	21 x^2 + 21x -1
101	204	x^2 + x + 3	67 x^2 + 67x -1
229	460	x^2 + x + 6	38 x^2 + 38x -1
257	516	x^2 + x + 5	154 x^2 + 154x -1
353	708	x^2 + x + 13	190 x^2 + 190x -1
461	924	x^2 + x + 2	230 x^2 + 230x -1
509	1020	x^2 + x + 2	254 x^2 + 254x -1
541	1084	x^2 + x + 10	54 x^2 + 54x -1
557	1116	x^2 + x + 8	348 x^2 + 348 x -1
569	1140	x^2 + x + 3	379 x^2 + 379 x -1
577	1156	x^2 + x + 10	173 x^2 + 173 x -1
641	1284	x^2 + x + 6	534 x^2 + 534 x -1
653	1308	x^2 + x + 14	513 x^2 + 513 x -1
1279	2560	x^2 + x + 6	213 x^2 + 213 x -1
1291	2584	x^2 + x + 2	645 x^2 + 645 x -1
1301	2604	x^2 + x + 10	130 x^2 + 130 x -1
1931	3864	x^2 + x + 14	1793 x^2 + 1793 x -1
1933	3868	x^2 + x + 5	773 x^2 + 733 x -1
2579	5160	x^2 + x + 18	1576 x^2 + 1576 x -1
2591	5184	x^2 + x + 21	987 x^2 + 987 x -1
2593	5188	x^2 + x + 10	1815 x^2 + 1815 x -1
2999	6000	x^2 + x + 19	947 x^2 + 947 x -1
3011	6024	x^2 + x + 6	2509 x^2 + 2509 x -1

A.2 ZCZ sequences

The construction of ZCZ sequences of triplet $(2^{p+2}n,\ 2n,\ 2^{p})$, as proposed in [46], can be accomplished in three steps:

1. Create an Hadamard matrix H of order n, denoted as $h_j = [h_{j,0}], h_{j,1}, \ldots, h_{j,n-1}$. Then, for $0 \leq j < n$, a set of $2n$ sequences d_j, each of length $2n$, is constructed by

$$d_{j+0} = [-h_j, h_j] \tag{A.1}$$

$$d_{j+1} = [h_j, h_j] \tag{A.2}$$

2. Secondly, a sequence set $\{B_j\}_{j=0}^{2n-1}$ is constructed from the sequence set $\{d_j\}_{j=0}^{2n-1}$ as follows

$$B_{j+0} = \left[d_{j+0,0},\quad d_{j+1,0},\ d_{j+0,1},\ \ d_{j+1,1}, \ldots,\ d_{j+0,2n-1},\ \ d_{j+1,2n-1}\right] \tag{A.3}$$

$$B_{j+1} = \left[d_{j+0,0},\ -d_{j+1,0},\ d_{j+0,1},\ -d_{j+1,1}, \ldots,\ d_{j+0,2n-1},\ -d_{j+1,2n-1}\right] \tag{A.4}$$

   Now, the sequence set size $\{B_j\}$ equals $2n$.

3. Finally, for $p > 0$ and $0 \leq j < n$, a new series can be constructed by interleaving $\{B_j\}_{j=0}^{2n-1}$ recursively,

$$B_{j+0} = \left[B_{j+0,0},\quad B_{j+1,0},\ B_{j+0,1},\ B_{j+1,1}, \ldots,\ B_{j+0,2n-1},\ B_{j+1,2n-1}\right] \tag{A.5}$$

$$B_{j+1} = \left[B_{j+0,0},\ -B_{j+1,0},\ B_{j+0,1},\ -B_{j+1,1}, \ldots,\ B_{j+0,2n-1},\ -B_{j+1,2n-1}\right] \tag{A.6}$$

Appendix B

Simulation Results: Synchronous Interference

B.1 Doppler Tolerance in Range-Doppler and Range-Angular Maps

Figure B.1 presents the range profiles for a single target's velocity and angular bin, where the moving object has been simulated for 0, 40, and 80 m/s. In these simulations Additive White Gaussian Noise is included.

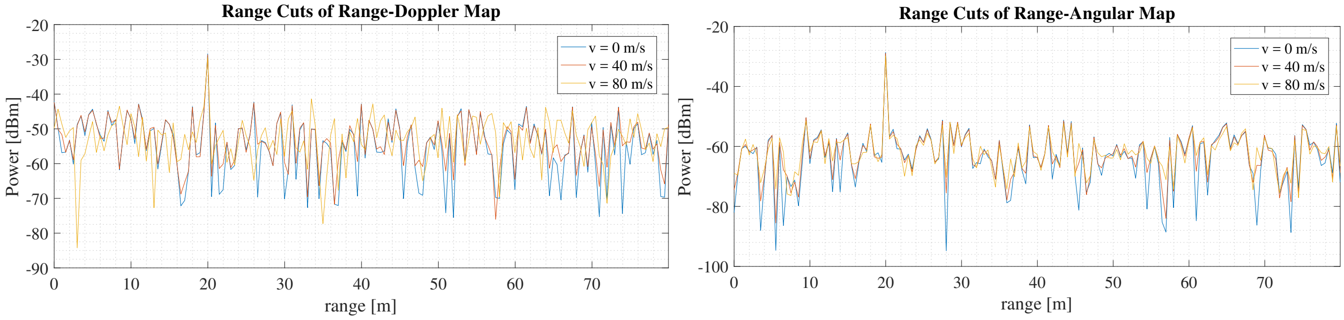

(a) Gold sequence with $L_c = 2047$

(d) Gold sequence with $L_c = 2047$

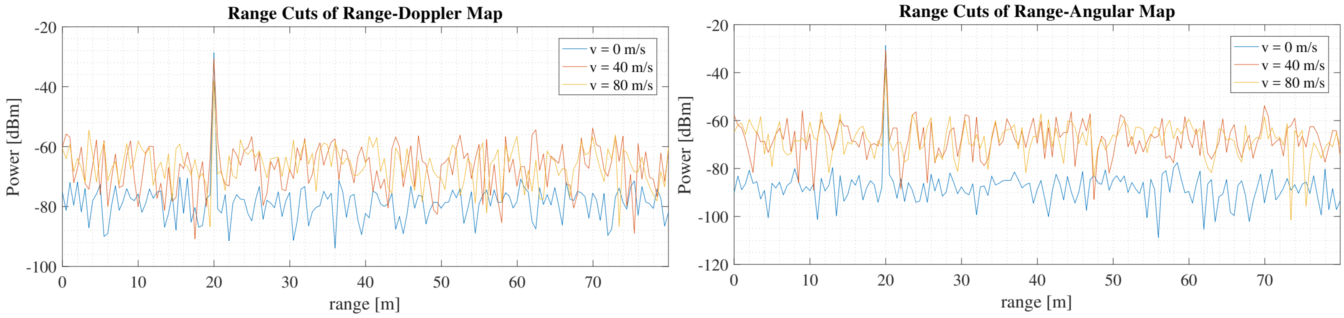

(b) APAS sequence with $L_c = 5184$

(e) APAS sequence with $L_c = 5184$

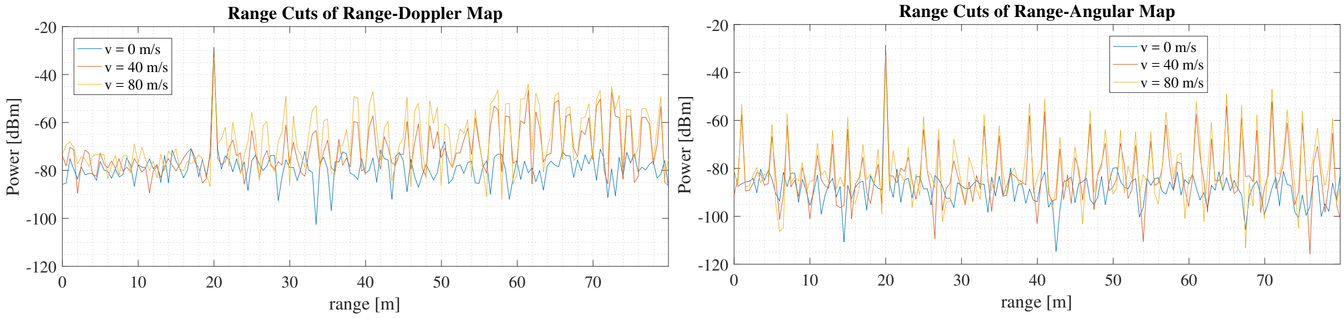

(c) ZCZ sequence with $L_c = 4096$

(f) ZCZ sequence with $L_c = 4096$

Figure B.1: Target Range cuts of (a-c) Range-Doppler Map and (d-f) Range-Angular Map

Bibliography

[1] H. H. Meinel, "Evolving automotive radar - From the very beginnings into the future," *8th European Conference on Antennas and Propagation, EuCAP 2014*, no. EuCAP, pp. 3107–3114, 2014.

[2] J. Hasch, E. Topak, R. Schnabel, T. Zwick, R. Weigel, and C. Waldschmidt, "Millimeter-wave technology for automotive radar sensors in the 77 GHz frequency band," *IEEE Transactions on Microwave Theory and Techniques*, vol. 60, no. 3 PART 2, pp. 845–860, 2012.

[3] A. Bourdoux, U. Ahmad, D. Guermandi, S. Brebels, A. Dewilde, and W. Van Thillo, "PMCW waveform and MIMO technique for a 79 GHz CMOS automotive radar," *2016 IEEE Radar Conference. RadarConf 2016*, pp. 1–5, 2016.

[4] NXP Semiconductors, "TEF810X Fully-Integrated 77 GHz Radar Transceiver." [Online]. Available: https://www.nxp.com/products/rf/radar-transceivers/tef810x-fully-integrated-77-ghz-radar-transceiver:TEF810X

[5] S. Patole, M. Torlak, D. Wang, and M. Ali, "Automotive Radars: A review of signal processing techniques," *IEEE Signal Processing Magazine*, no. March, pp. 22–35, 2017.

[6] M. A. Richard, *Fundamentals of Radar Signal Processing*. McGraw-Hill Professional Engineering, 2014.

[7] Z.-b. Lin, "Wideband ambiguity function of broadband signals," *The Journal of the Acoustical Society of America*, vol. 83, no. 6, p. 2108, 1988.

[8] L. G. Weiss, "Wavelets and Wideband Correlation Processing," *IEEE Signal Processing Magazine*, 1994.

[9] M. A. Richards, J. A. Scheer, and W. A. Holm, *Principles of Modern Radar: Basic Principles*, 1st ed. SciTech Publishing, 2015, vol. 1.

[10] W. Van Thillo, V. Giannini, D. Guermandi, S. Brebels, and A. Bourdoux, "Impact of ADC clipping and quantization on phase-modulated 79 GHz CMOS radar," *European Microwave Week 2014: "Connecting the Future", EuMW 2014 - Conference Proceedings; EuRAD 2014: 11th European Radar Conference*, no. 1, pp. 285–288, 2014.

[11] M. Goppelt, H. L. Blöcher, and W. Menzel, "Automotive radar-investigation of mutual interference mechanisms," *Advances in Radio Science*, vol. 8, pp. 55–60, 2010.

[12] M. Goppelt, H.-L. Blocher, and W. Menzel, "Analytical investigation of mutual interference between automotive FMCW radar sensors," *2011 German Microwave Conference*, no. March, pp. 1–4, 2011.

[13] G. M. Brooker, "Mutual interference of millimeter-wave radar systems," *IEEE Transactions on Electromagnetic Compatibility*, vol. 49, no. 1, pp. 170–181, 2007.

[14] S. Sanka, "RADAR to RADAR Interference for 77GHz Automotive RADARs," Master's thesis, Delft University of Technology, 2017.

[15] G. Lajiness, "Interference rejection method for an automotive radar cw/icc system," 06 1999.

[16] M. Rameez, M. Dahl, and M. I. Pettersson, "Adaptive Digital Beamforming for Interference Suppression in Automotive FMCW Radars," pp. 252–256, 2018.

[17] J. Bechter, K. Eid, F. Roos, and C. Waldschmidt, "Digital beamforming to mitigate automotive radar interference," *2016 IEEE MTT-S International Conference on Microwaves for Intelligent Mobility, ICMIM 2016*, pp. 2–5, 2016.

[18] H. Chahrour, S. Rajan, R. Dansereau, A. M. Radar, and S. Model, "Hybrid Beamforming for Interference Mitigation in MIMO Radar," pp. 1005–1009, 2018.

[19] J. Bechter, F. Roos, M. Rahman, and C. Waldschmidt, "Automotive Radar Interference Mitigation Using a Sparse Sampling Approach," *Proceedings of the 14th European Radar (EuRAD-2017) Conference*, pp. 90–93, 2017.

[20] F. Uysal and S. Sanka, "Mitigation of automotive radar interference," in *2018 IEEE Radar Conference (RadarConf18)*, April 2018, pp. 0405–0410.

[21] H.-P. Beise, T. Stifter, and S. A. Iee, "Virtual Interference Study for FMCW and PMCW Radar," pp. 351–354, 2018.

[22] A. Bourdoux, K. Parashar, and M. Bauduin, "Phenomenology of mutual interference of FMCW and PMCW automotive radars," *2017 IEEE Radar Conference, RadarConf 2017*, no. Mi, pp. 1709–1714, 2017.

[23] M. I. Skolnik, *Radar Handbook*, 3rd ed. McGraw-Hill Professional Engineering, 2008.

[24] N. Levanon and E. Mozeson, "Phase-coded pulse," in *Radar Signals.* John Wiley & Sons, Inc, 2004, pp. 100–167.

[25] M. Jankiraman, *Design of Multi-Frequency CW Radars*, 1st ed. SciTech Publishing, 2007.

[26] FCC, "FCC FACT SHEET Radar Services in the 76-81 GHz Band, url = https://docs.fcc.gov/public/attachments/DOC-348982A1.pdf."

[27] H.-J. Zepernick and A. Finger, *Pseudo Random Signal Processing: Theory and Application.* John Wiley & Sons Ltd, 2005.

[28] D. Peng and P. Fan, "Generalised Sarwate bounds on periodic autocorrelations and cross-correlations of binary sequences," *Electronics Letters*, vol. 38, no. 24, pp. 1521–1523, 2002.

[29] L. R. Welch, "Lower Bounds on the Maximum Cross Correlation of Signals," *IEEE Transactions on Information Theory*, vol. 20, no. 3, pp. 397–399, 1974.

[30] X. Tang, P. Fan, and S. Matsufuji, "Lower Bounds on Correlation of Spreading Sequence Set with Low or Zero Correlation Zone," *Electronics Letters*, vol. 36, no. 6, pp. 551–552, 1967.

[31] L. O'carroll, D. Davies, C. Smyth, J. Dripps, and P. Grant, "A study of auto-and cross-ambiguity surface performance for discretely coded waveforms," *IEE Proceedings F Radar and Signal Processing*, vol. 137, no. 5, p. 362, 1990.

[32] N. Levanon, "CW Alternatives to the Coherent Pulse Train - Signals and Processors," *IEEE TRANSACTIONS ON AEROSPACE AND ELECTRONIC SYSTEMS*, vol. 29, no. 1, 1993.

[33] J. J. De Wit, W. L. Van Rossum, and A. J. De Jong, "Orthogonal waveforms for FMCW MIMO radar," *IEEE National Radar Conference - Proceedings*, pp. 686–691, 2011.

[34] C. Pfeffer, R. Feger, C. Wagner, and A. Stelzer, "FMCW MIMO Radar System for Frequency-Division Multiple TX-Beamforming," *IEEE Transactions on Microwave Theory and Techniques*, vol. 61, no. 12, pp. 4262–4274, dec 2013.

[35] T. Fickenscher, a. Gupta, J. Hinz, M. Holters, and U. Zolzer, "MIMO surface wave radar using time staggered FMCW chirp signals," *2011 8th European Radar Conference*, vol. 1, no. October, pp. 69–72, 2011.

[36] H. Haderer, R. Feger, C. Pfeffer, and A. Stelzer, “Millimeter-Wave Phase-Coded CW MIMO Radar Using Zero- and Low-Correlation-Zone Sequence Sets,” *IEEE Transactions on Microwave Theory and Techniques*, vol. 64, no. 12, pp. 4312–4323, 2016.

[37] A. van der Veen and G. Leus, *Signal processing for communications*, 2005, vol. 6.

[38] Krim H and M. Viberg, “Two Decades of Array Signal Processin Research,” *IEEE Signal Processing Magazine*, vol. 13, no. 4, Jul 1996, pp. 67–94, 1996.

[39] A. Bourdoux, “Mutual Interference Analysis of PMCW and FMCW radars,” in *European Microwave Week*, Nuremberg, Germany, 2017, pp. 1–26.

[40] A. M. D. Turkmani and U. S. Goni, “Performance Evaluation of Maximal-length , Gold and Kasami Codes as Spreading Sequences in CDMA Systems,” pp. 970–974.

[41] J. Wolfmann, “Almost Perfect Autocorrelation Sequences,” *IEEE Transactions on Information Theory*, vol. 38, no. 4, pp. 1412–1418, 1992.

[42] A. Pott and S. P. Bradley, “Existence and Nonexistence of Almost-Perfect Autocorrelation Sequences,” *IEEE Transactions on Information Theory*, vol. 41, no. I, pp. 301–304, 1995.

[43] W. Van Thillo, P. Gioffr, V. Giannini, D. Guermandi, S. Brebels, and A. Bourdoux, “Almost perfect autocorrelation sequences for binary phase-modulated continuous wave radar,” pp. 1803–1806, 2013.

[44] E. W. Weisstein, “"Totient Function".” [Online]. Available: http://mathworld.wolfram.com/TotientFunction.html

[45] P. Fan, N. Suehire, N. Kuroyanagi, and X. Deng, “Class of Binary Sequences with Zero Correlation Zone,” *Electronics Letters*, vol. 25, no. 10, pp. 777–779, 1999.

[46] B. Fassi, “A New Class of Binary Zero Correlation Zone Sequence Sets,” *IOSR Journal of Electronics and Communication Engineering (IOSR-JECE)*, vol. 5, no. 3, pp. 15–19, 2013.

[47] A. Manikas, “Principles of Spread Spectrum Systems,” pp. 1–46, 2011.

[48] C. Carlet and A. Pott, *Sequences and Their Applications - SETA 2010*, 2010.

[49] D. Guermandi, Q. Shi, A. Dewilde, V. Derudder, U. Ahmad, A. Spagnolo, I. Ocket, A. Bourdoux, P. Wambacq, J. Craninckx, and W. Van Thillo, “A 79 GHz 2 x 2 MIMO PMCW Radar SoC in 28 nm CMOS,” *IEEE Journal of Solid-State Circuits*, pp. 1–14, 2017.

[50] H.-L. Bloecher, A. Sailer, G. Rollmann, and J. Dickmann, “79 GHz UWB automotive short range radar – Spectrum allocation and technology trends,” *Advances in Radio Science*, vol. 7, no. December 2009, pp. 61–65, 2009.

[51] N. Chen, R. Gourova, O. A. Krasnov, and A. Yarovoy, “The influence of the water-covered dielectric radome on 77GHz automotive radar signals,” *European Microwave Week 2017: "A Prime Year for a Prime Event", EuMW 2017 - Conference Proceedings; 14th European Microwave Conference, EURAD 2017*, vol. 2018-Janua, pp. 139–142, 2018.

[52] C. M. Schmid, R. Feger, C. Pfeffer, and A. Stelzer, “Motion compensation and efficient array design for TDMA FMCW MIMO radar systems,” *Proceedings of 6th European Conference on Antennas and Propagation, EuCAP 2012*, pp. 1746–1750, 2012.

[53] F. J. Harris and Others, “On the use of windows for harmonic analysis with the discrete Fourier transform,” pp. 51–83, 1978.

[54] Tektronix, “Technical Reference: AWG5000 Series. Arbitrary Waveform Generators - Specifications and Performance Verification, url=https://www.tek.com/awg5002-manual/awg5000-series-technical-reference.”

[55] Mini-Circuits, “Data sheet: Power Splitter / Combiner.”

[56] Keysight, “Agilent Infiniium 90000 X-Series Oscilloscopes Data Sheet.”

[57] S. E. O’Connor, “A Program for Computing Primitive Polynomials,” accessed 2017-12-12. [Online]. Available: http://www.seanerikoconnor.freeservers.com/Mathematics/AbstractAlgebra/PrimitivePolynomials/userManual.html